



<https://theses.gla.ac.uk/>

Theses Digitisation:

<https://www.gla.ac.uk/myglasgow/research/enlighten/theses/digitisation/>

This is a digitised version of the original print thesis.

Copyright and moral rights for this work are retained by the author

A copy can be downloaded for personal non-commercial research or study, without prior permission or charge

This work cannot be reproduced or quoted extensively from without first obtaining permission in writing from the author

The content must not be changed in any way or sold commercially in any format or medium without the formal permission of the author

When referring to this work, full bibliographic details including the author, title, awarding institution and date of the thesis must be given

Enlighten: Theses

<https://theses.gla.ac.uk/>  
[research-enlighten@glasgow.ac.uk](mailto:research-enlighten@glasgow.ac.uk)

THE NUCLEAR PHOTOEFFECT IN LIGHT NUCLEI

AT MEDIUM TO HIGH PHOTON ENERGIES

DAVID J.S. FINDLAY

Submitted to the University of Glasgow (October 1975)

as a thesis for the degree of Doctor of Philosophy

ProQuest Number: 10800643

All rights reserved

INFORMATION TO ALL USERS

The quality of this reproduction is dependent upon the quality of the copy submitted.

In the unlikely event that the author did not send a complete manuscript and there are missing pages, these will be noted. Also, if material had to be removed, a note will indicate the deletion.



ProQuest 10800643

Published by ProQuest LLC (2018). Copyright of the Dissertation is held by the Author.

All rights reserved.

This work is protected against unauthorized copying under Title 17, United States Code  
Microform Edition © ProQuest LLC.

ProQuest LLC.  
789 East Eisenhower Parkway  
P.O. Box 1346  
Ann Arbor, MI 48106 – 1346

Thesis  
4293  
Copy 1



## PREFACE

The experiments described in this thesis were carried out at the University of Glasgow in collaboration with Drs. R. O. Owens, J. L. Matthews and S. H. Gardiner, and these experiments, together with the analysis, took place between October 1972 and April 1975.

The experiments are investigations of the medium to high energy nuclear photoeffect in various p-shell nuclei; this territory has not been well explored, and the present experiments represent a considerable advance.

The high energy nuclear photoeffect is interesting because it is primarily a high momentum process, and should therefore be sensitive to short range effects between nucleons in the nucleus, effects to which most other nuclear processes are not sensitive.

The set of data gathered is sufficiently extensive to show that the simplest interpretation of the high energy nuclear photoeffect is very reasonable. Also it is found that the independent particle shell model is incapable of explaining experiment; short range residual interactions are necessary. but a popular method of introducing such interactions, relatively successful for some other high momentum processes, is shown to be inappropriate, and it is found that, in between the giant dipole resonance and the  $\pi$ -meson production threshold, the most important residual interaction is single  $\pi$ -meson exchange.

Chapter 1 of this thesis presents the details of the experiments performed and gives a general discussion of the nuclear photoeffect, Chapter 2 describes the experimental system, Chapter 3 describes the data analysis, Chapter 4 presents the results, and Chapter 5 discusses the results. Mathematical machinery may be found in the Appendices.

# CONTENTS

Preface	page	1
Acknowledgements		11
<b>CHAPTER 1</b>	<b>INTRODUCTION</b>	
1.1	Introduction	1
1.2	The experiments	3
1.3	The ( $\gamma$ ,p) reaction	6
1.4	Residual interactions	9
1.5	Reaction mechanism	12
1.6	Other single nucleon knock-out reactions	14
1.7	Experimental considerations	16
1.8	Summary	19
<b>CHAPTER 2</b>	<b>THE EXPERIMENTAL SYSTEM</b>	
2.1	The experimental system in general	20
2.2	Accelerator	21
2.3	Beam handling and energy analysis system	23
2.4	Scattering chamber	25
2.5	Bremsstrahlung radiators	26
2.6	Photomuclear targets	27
2.7	Magnetic spectrometer	30
2.8	Counters and counter ladder	33
2.9	Charge monitor	36
2.10	Signal processing electronics	38
2.11	Computer interface	40
2.12	Computer programme	42

## CHAPTER 3 DATA ANALYSIS

3.1	Introduction	page 44
3.2	Determination of proton peak area from raw data	45
3.3	Determination of the proton yield spectrum	49
3.4	Bremsstrahlung spectra	52
3.5	Calculation of the proton spectrum shape	55
3.6	Determination of the cross-sections	58

## CHAPTER 4 EXPERIMENTAL RESULTS

4.1	Introduction	61
4.2	Li <sup>6</sup>	65
4.3	Li <sup>7</sup>	67
4.4	C <sup>12</sup>	68
4.5	O <sup>16</sup>	69

## CHAPTER 5 DISCUSSION OF RESULTS

5.1	Description of results and qualitative deductions from results	71
5.2	Comparison with other ( $\gamma$ ,p) experiments	
5.2.1	Introduction	74
5.2.2	Li <sup>6</sup>	74
5.2.3	Li <sup>7</sup>	75
5.2.4	C <sup>12</sup>	76
5.2.5	O <sup>16</sup>	77
5.3	Comparison with theory	
5.3.1	( $\gamma$ ,p) calculations	79
5.3.2	Comparison with independent particle shell model calculations	
5.3.2.1	The ( $\gamma$ ,p) calculation developed for comparison with the present data	86
5.3.2.2	Li <sup>6</sup>	89
5.3.2.3	Li <sup>7</sup>	91

5.3.2.4	C <sup>12</sup>	page 93
5.3.2.5	O <sup>16</sup>	93
5.3.2.6	Conclusions	96
5.3.3	Comparison with calculations involving residual interactions	
5.3.3.1	Introduction	99
5.3.3.2	Li <sup>7</sup>	100
5.3.3.3	C <sup>12</sup>	101
5.3.3.4	O <sup>16</sup>	102
5.3.3.5	Conclusions	103
5.4	Momentum distributions	105
5.5	Conclusions	109
5.6	Future developments	110

#### APPENDICES

1	Alpha-calibration	113
2	Energy analysis system calibration	115
3	Spectrometer calibration	117
4	Relationship between counted protons and cross-section	119
5	Counter relative efficiencies	122
6	Counter absolute efficiency	124
7	Photon single difference technique	126
8	Calculation of a bremsstrahlung spectrum from a radiator of finite thickness	129
9	Energy loss and straggling of photoproduced charged particles in a photonuclear target	130
10	Energy straggling and spectrum dilation in absorbers	132
11	The ( $\gamma$ ,p) cross-section in the independent particle shell model - electric term only - no spin	135

12	The plane-wave ( $\chi, p$ ) matrix element - electric term only - no spin	page 138
13	The distorted-wave ( $\chi, p$ ) matrix element - electric term only - no spin	140
14	Optical potential - approximate methods	145
15	Fourier transforms	146
	<b>REFERENCES</b>	147

## 1.1 General Introduction

The experiments described in this thesis are investigations of the nuclear photoeffect in the  $\text{Li}^7$ ,  $\text{C}^{12}$  and  $\text{O}^{16}$  nuclei at photon energies between 40 and 105 MeV. These energies are considerably higher than the energy of the giant dipole resonance where the photon interacts with the nucleons as a whole; the photon interacts instead with individual nucleons. Hence such experiments are sensitive to the behaviour of individual nucleons in the nucleus.

The  $(\gamma, p)$  reaction, ejection of a photoproton, is a reaction which is particularly dependent on the high momentum components of the nuclear wavefunction, and is characterised, in the energy range mentioned above, by cross-sections which are generally accepted to be underestimated by shell model predictions. This is attributed to a deficiency of high momentum components in shell model wavefunctions because of their having been determined in a self-consistent potential thereby ignoring the explicit medium to short range part of the nucleon-nucleon interaction. The addition of such residual interactions to the shell model will alter the  $(\gamma, p)$  cross-section predictions. Comparison with experiment will then indicate the acceptable methods by which this addition could be implemented.

Experimental  $(\gamma, p)$  results in the energy range of interest here are not plentiful; the general problem of the non-existence of a source/.....

source of monochromatic photons and the particular problem of the low cross-section at high energy have troubled experimentalists for many years and have led to results whose accuracy and range are, in general, not noteworthy. However, at the University of Glasgow these problems have been largely overcome. The Glasgow 100 MeV electron linear accelerator has a reasonably high output current, and the count rate is perfectly satisfactory everywhere except at backward angles at around 100 MeV. The problem of the monochromatic photon source is overcome by using a photon single-difference technique developed at this University. When these two features are combined with the use of magnetic spectrometer carrying a set of energy sensitive counters in its focal plane to detect the protons, experiments which are significantly more accurate and wider in range than previous ones are possible.

It is hoped that the present experiment fulfils such aspirations, and will be able, with the help of suitable theoretical calculations, to provide some useful information.

## 1.2 The Experiments

The experiments described in this thesis were undertaken to provide a more stringent test of theoretical predictions, and they continue and greatly extend the previous ( $\gamma, p$ ) measurements made at The University of Glasgow. These previous measurements<sup>1,2</sup>, angular distributions of the  $\text{Li}^6$ ,  $\text{Li}^7$  and  $\text{C}^{12}$  ( $\gamma, p$ ) cross-sections to specific final states at a photon energy of 60 MeV, were the first such measurements to be made. Extension of these measurements to higher energies and other nuclei was desirable.

The experiments performed were measurements of the angular distributions of the following cross-sections:  $\text{Li}^7$  ( $\gamma, p$ ) at 80 MeV,  $\text{C}^{12}$  ( $\gamma, p$ ) at 80 and 100 MeV, and  $\text{O}^{16}$  ( $\gamma, p$ ) at 60, 80 and 100 MeV. In addition the  $\text{Li}^7$  ( $\gamma, p$ ) cross-section was measured at  $45^\circ$  at 100 MeV, and the  $\text{O}^{16}$  ( $\gamma, p$ ) cross-section was measured at  $45^\circ$ ,  $75^\circ$  and  $105^\circ$  at 95 MeV, and at  $45^\circ$  at 40, 50, 70, 90 and 105 MeV. The Glasgow 100 MeV electron linear accelerator was used. For the lithium and carbon experiments, the photon single-difference technique mentioned above was employed. This involves the difference of two bremsstrahlung spectra from beryllium and aluminium radiators and gives photons whose monochromaticity is  $\pm 1$  MeV FWHM. The technique is fully described in Appendix 7. For the oxygen experiment the difference technique was not required and bremsstrahlung from a gold radiator ( $.191 \pm .001$  gm/cm<sup>2</sup>,  $\sim .03$  radiation lengths) was used. The targets were  $\text{Li}^7$  metal (separated isotope), graphite and beryllium oxide. The targets were situated/.....

situated in a scattering chamber which also contained the bremsstrahlung radiators. A magnetic spectrometer, rotatable about the centre of the scattering chamber between about  $25^\circ$  and  $155^\circ$  with respect to the direction of the beam line, was used to momentum analyse the photoprotons. A set of ten plastic scintillation counters each with its own photomultiplier was employed in the focal plane of the spectrometer, and the signals from the photomultipliers were pulse height analysed and the spectra stored in a computer. Since the scintillation counters are energy sensitive, the desired proton contribution may be easily separated from any other particles and background which may be present. The total charge delivered to the bremsstrahlung radiators (which determines the numbers of photons delivered to the photonuclear target) was measured by integrating the current in the electron beam measured by a non-intercepting toroidal current transformer whose primary is the electron beam itself. For the photon difference technique to work satisfactorily, accurate determination of the total charge is important. The details of the experimental system are fully described in Chapter 2.

The cross-sections were obtained from the experimental proton energy spectra by fitting them with a sum of proton spectrum shapes, calculated from the photon spectrum, each of which corresponds to a different state in the residual nucleus. The fitting procedure determines the coefficient of each shape function in the sum, and these coefficients are the cross-sections to each state in the residual nucleus. Using this technique, individual  $C^{12}(\gamma, p) B^{11}$  cross-sections/.....

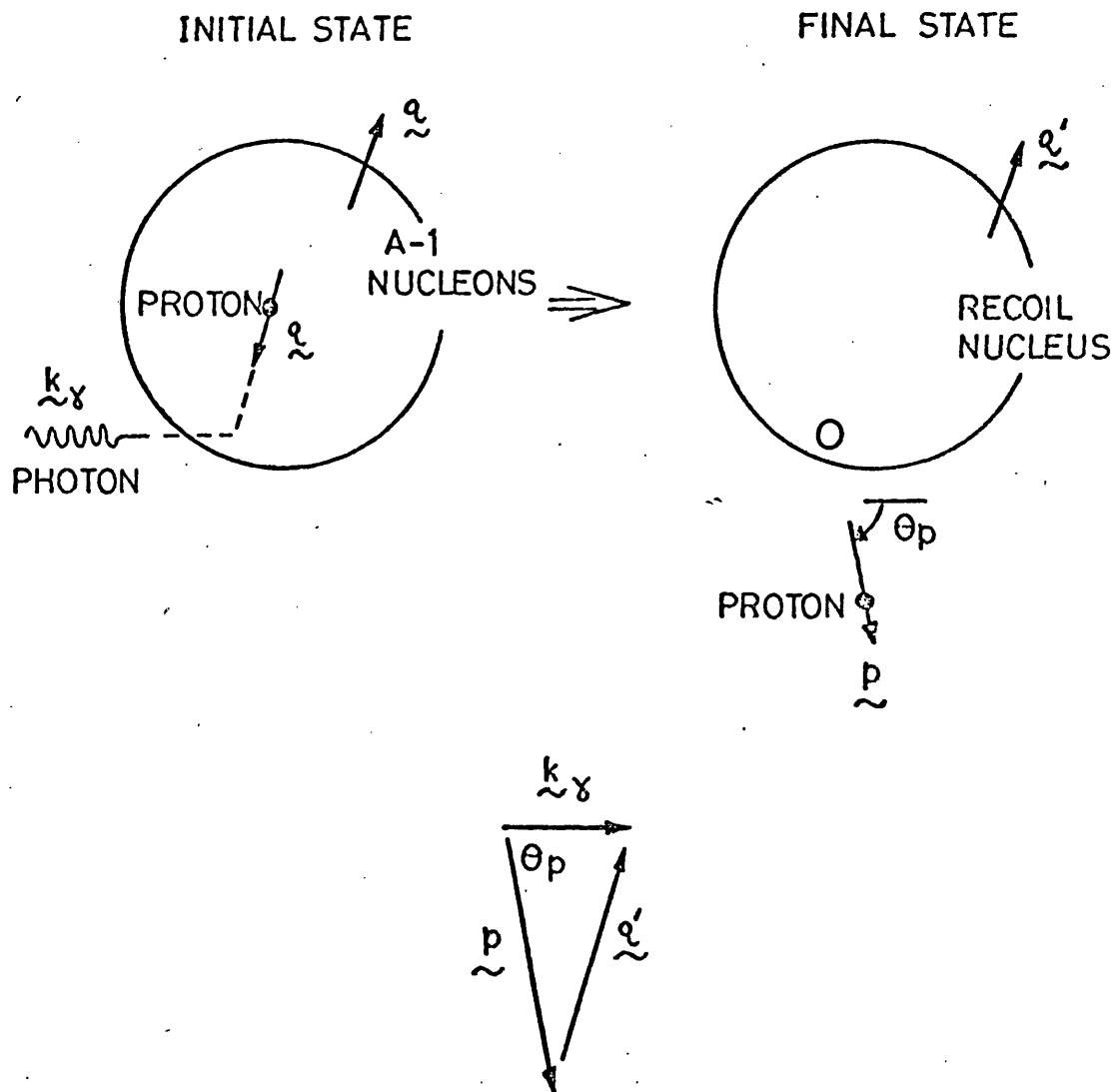
sections to the ground state, 2.12 MeV first excited state and the group of three states at 4.44, 5.02 and 6.74 MeV in  $B^{11}$  were separated. The  $Li^7 (\gamma, p) He^6$  cross-sections to the ground state and 1.80 MeV first excited state in  $He^6$  have not been completely separated because of the relative proximity of these two states and lack of statistical accuracy. For the  $O^{16} (\gamma, p) N^{15}$  reaction, only the cross-sections to the ground state of  $N^{15}$  have been determined. The beryllium in the beryllium oxide target used did not affect their measurements. Due to the differences in the proton separation energies and the masses of the  $Be^9$  and  $O^{16}$  nuclei, the protons from  $Be^9$  corresponding to the endpoint of the bremsstrahlung spectrum are at least 6 MeV below similar protons from  $O^{16}$ . Since there is no excited state of  $N^{15}$  with an excitation energy of less than 5.27 MeV, the top 5 MeV of the proton spectrum can only contain protons leaving  $N^{15}$  in its ground state, the cross-section to which may then readily be determined. The data analysis is fully described in Chapter 3.

### 1.3 The ( $\gamma, p$ ) Reaction

If a proton is ejected at  $90^\circ$  from  $O^{16}$  by a 100 MeV photon and the residual nucleus is left in its ground state, the proton energy is 81.8 MeV and hence a mismatch of  $\sim 410$  MeV/c exists between the momentum of the photon and that carried away by the proton (see Fig. 1.1). This difference can only be made up if the proton has this high momentum in the initial bound state, which is relatively unlikely. This is what is meant when it is stated that the ( $\gamma, p$ ) process is dependent on the high momentum components of the nuclear wavefunction. The momentum mismatch becomes greater as the angle at which the photoproton is ejected increases and as the photon energy increases, and the experimental ( $\gamma, p$ ) cross-section becomes smaller as the momentum mismatch increases. At Glasgow the highest momentum mismatch investigated is 455 MeV/c ( $O^{16}$  ( $\gamma, p$ )  $N_{g.s.}^{15}$  for  $E_\gamma = 100$  MeV at  $120^\circ$ ). Recently MIT<sup>3)</sup> has extended measurements on the  $O^{16}$  ( $\gamma, p$ )  $N_{g.s.}^{15}$  reaction up to 280 MeV at  $90^\circ$  corresponding to a momentum mismatch of 776 MeV/c.

The ( $\gamma, p$ ) cross-section is intimately related to the momentum wavefunction  $\phi(\underline{q})$  of the bound state (the Fourier transform of the bound state configuration space wavefunction). In the plane wave approximation (Appendix 12) the differential cross-section is directly proportional to  $|\phi(\underline{q})|^2$ . For a final state which is a scattering state of an appropriate optical potential (Appendix 13) the relationship, although equally intimate, is not so transparent. An experimental momentum distribution can be extracted from/.....

# DIRECT PHOTOPROTON EJECTION



KINEMATICS:  ${}^{16}_0(\gamma, p){}^{15}_{9s}$

$Q = -12 \text{ MeV}$

$E_\gamma = 100 \text{ MeV}$

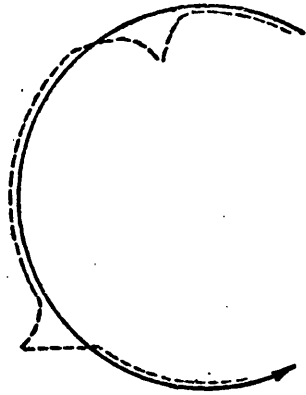
$\theta_p$	$E_p \text{ (MeV)}$	$p \text{ (MeV/c)}$	$q' \text{ (MeV/c)}$
30°	84.1	406.1	323.3
150°	79.5	394.4	483.7

FIG. 1.1

from the measured  $(\gamma, p)$  cross-sections; this is discussed in section 5.4. However, the resulting distribution depends on the plane wave formalism assumed. Probably the only reasonable way to derive a momentum distribution would be to search for a bound state wavefunction which, when used to calculate  $(\gamma, p)$  cross-sections, leads to best agreement with experiment; its Fourier transform would then give the momentum distribution.

Shell model predictions of  $(\gamma, p)$  cross-sections are inconsistent with experiment. These predictions are sensitive to the details of the bound state and the optical potential as well as to calculational details (see section 5.3), but for the  $O^{16}(\gamma, p) N_{g.s.}^{15}$  reaction, a reaction in which the overlap of the ground state of the target nucleus with the ground state of the residual nucleus is expected to be well described by a single particle wavefunction, the distorted wave calculation developed for the analysis of the experiments in this thesis shows the predicted shell model cross-sections to be too low by a factor of  $\sim 10$ . Also it will be shown in section 5.4 that the shell model momentum distribution underestimates the measured momentum distribution and does not reproduce the measured shape.

The predicted  $(\gamma, p)$  cross-sections are increased if short range residual interactions or correlations are incorporated; Fig. 1.3 provides some illustrations. So far these residual interactions have been treated by adding either Jastrow correlation factors or a single  $\pi$ -meson exchange potential to the shell model. The introduction of residual/.....



- NUCLEON PATH IN SHELL MODEL SINGLE PARTICLE POTENTIAL.  
--- NUCLEON PATH INCLUDING RESIDUAL INTERACTIONS.



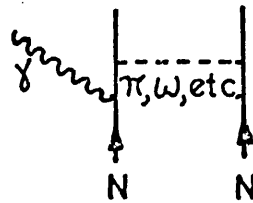
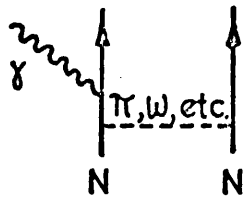
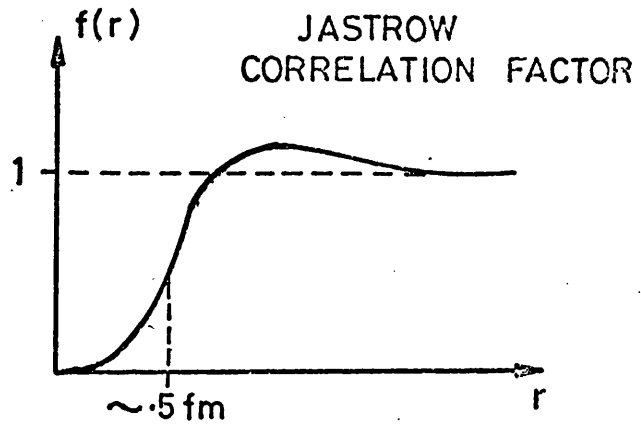
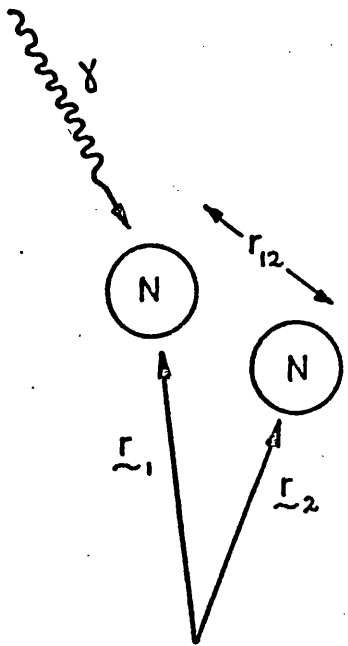
INTERACTION OF PHOTON WITH NUCLEON  
IN INDEPENDENT PARTICLE SHELL MODEL.

Fig. 1.2

residual interactions into  $(\gamma, p)$  calculations is discussed in section 5.3. Certainly this increases the proportion of high momentum components, and such calculations are more successful than pure shell model calculations. However, much work still remains to be done here. An unsuspected rise in the  $(\gamma, p)$  cross-section for  $\sim 300$  MeV photons has been very recently found at MIT<sup>3)</sup>, and this might be due to the formation of the  $\Delta(1236)$  isobar. It may be that agreement between theory and experiment will not be reached until all the contributions by the various mesons and isobars are included.

SHORT RANGE CORRELATIONS.

$$\Psi(\underline{r}_1, \underline{r}_2) = \psi_1(\underline{r}_1) \psi_2(\underline{r}_2) f(r_{12})$$



PHOTON INTERACTION WITH  
MESON EXCHANGE CURRENTS.

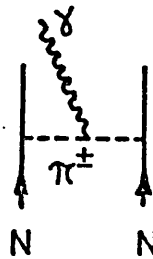
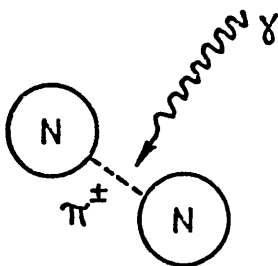


Fig. 1.3

#### 1.4 Residual Interactions

The independent particle shell model has well known inadequacies. While this model may explain the ground states of most nuclei, it is very obvious that it cannot explain the plethora of excited nuclear states found experimentally. Residual interactions must be introduced to produce configuration mixing giving a Hamiltonian which, to be useful, must be diagonalised in a truncated set of basis states. These residual interactions are, however, relatively weak and are treated as perturbations. They couple entire shell model orbits together. In general, they are not the residual interactions of importance when high momentum processes are considered. High momentum processes are those for which the characteristic momentum is higher than the Fermi momentum,  $\sim 1.4\text{fm}^{-1}$  or  $280\text{ MeV}/c$ , and for which strong short range residual interactions are important. The inclusion of strong residual interactions or correlations in the configuration mixing and diagonalisation procedures would require a prohibitively large set of basis states. The approach used for inclusion of short range residual interactions is much simpler and has been to start with independent particle shell model wave functions and phenomenologically insert some sort of correlation factor either in a wavefunction itself or a matrix element.<sup>4)</sup>

A nucleon in the nucleus may be pictured <sup>5)</sup> as spending most of its time travelling in a smooth curve (the solid line in Fig.1.2), corresponding/.....

corresponding to the single particle self-consistent potential. However, when the nucleon approaches close to another nucleon, the rapidly varying nucleon-nucleon potential leads to the generation of high momenta. The actual path travelled by the nucleon will, therefore, be more like the dotted line. Therefore on average, the actual wavefunction of the nucleon will contain more high momentum components than the corresponding shell model wavefunction.

There are many high momentum processes sensitive to these short range residual interactions. Any nuclear process which requires a high momentum to be provided by a bound nucleon or nucleons is appropriate. Some examples are: high energy photodisintegration ( $(\gamma, t)$ ,  $(\gamma, t n)$ , etc.), quasi-free scattering ( $(e, e'p)$ ,  $(p, 2p)$ ) and pick-up ( $(p, d)$ , etc.) reactions at high momentum transfer, absorption and production of  $\pi$ -mesons ( $(\pi, NN)$ ,  $(p, \pi)$ , etc.) and elastic electron scattering at high momentum transfer. For the  $(\gamma, p\pi)$  reaction, the relative success of the quasi-deuteron model<sup>5)</sup> shows the importance of short range residual interactions.

The lack of agreement of shell model predictions with experiment is well established for many such processes. The  $O^{16}$  nucleus is expected to be well described by the shell model. However, the measured electron scattering charge form-factor of  $O^{16}$  at momentum transfers of greater than about  $1.5 \text{ fm}^{-1}$  cannot<sup>6)</sup> be described by Woods-Saxon bound state wavefunctions. The nuclear absorption of a  $\pi$ -meson from a  $\pi$ -mesic atom results in a large momentum mismatch ( $\sim 550 \text{ MeV/c}$ ) and shell model calculations underestimate<sup>4)</sup> the absorption rates by several/.....

several orders of magnitude. This lack of agreement is held to be due to neglect of strong short range residual interactions.

The high momentum process in the experiments described in this thesis was the  $(\gamma, p)$  reaction. Advantages of the  $(\gamma, p)$  reaction include the absence of any coincidence requirements and an electromagnetic interaction which avoids the problem of the severe distortion involved if a strongly interacting projectile is used. Disadvantages include the difficulty of effectively procuring a source of reasonably monochromatic photons.

### 1.5 Reaction Mechanism

In a high energy ( $\gamma, p$ ) reaction, since the photon interaction is a one-body interaction, all the momentum carried by the incident photon is transferred to one bound proton (possibly via a meson). The proton is raised from a bound state of negative energy to a continuum state of positive energy, and so may travel out of the nucleus, being refracted by the final state potential in the process. The mass  $A$  target nucleus, in its ground state, has one proton knocked out of it, i.e. a hole state<sup>7)</sup> is produced, and given that the ejected proton is travelling more quickly than the rest of the nucleons in the nucleus, the remaining  $A-1$  nucleons are more or less just spectators. These  $A-1$  nucleons are not in their natural configuration, and so this hole state rearranges itself into the ground state or one of the excited states of the residual nucleus, the change in energy being the rearrangement energy.

The probability that some particular state in the residual nucleus is populated is determined by the fractional parentage coefficients involved in the expansion of the ground state of the target nucleus in terms of products of the various states of the residual nucleus and single particle states. This expansion limits the number of states which can be reached in the residual nucleus; for example, from conservation of parity, photoejection of a proton from the p-shell of  $O^{16}$  can only lead to positive parity states of  $N^{15}$  if the ground state of  $O^{16}$  includes 2p2h virtual excitations to the s,d-shell.

When/.....

When a nucleon is ejected from an inner shell deep in the target nucleus, the resulting hole state decays very quickly. The short lifetime is seen as the large width of the hole state, e.g. for  $C^{12}$ , the width of the s-hole state is  $\sim 10$  MeV, giving a lifetime of  $\sim 10^{-22}$  sec. Such a hole state is believed to decay mainly by the autoionisation<sup>8)</sup> process. In p-shell nuclei two nucleons in the  $p_{3/2}$ -shell interact, one dropping into the vacant  $s_{1/2}$ -hole and the other being ejected from the nucleus (a "nuclear Auger" proton). This ejected nucleon travels very slowly compared with the original proton involved in the knock-out reaction.

The spectrum of knock-out protons to be expected in p-shell nuclei is thus a clump of discrete states at a missing energy of  $\sim 15$  MeV, p-shell ejection, corresponding to the various fractional parentage coefficients, and a continuum of states at  $\sim 35$  MeV, s-shell ejection. The experimental proton spectrum from  $C^{12}$  1) is shown in Fig. 1.4. It agrees well with the above.

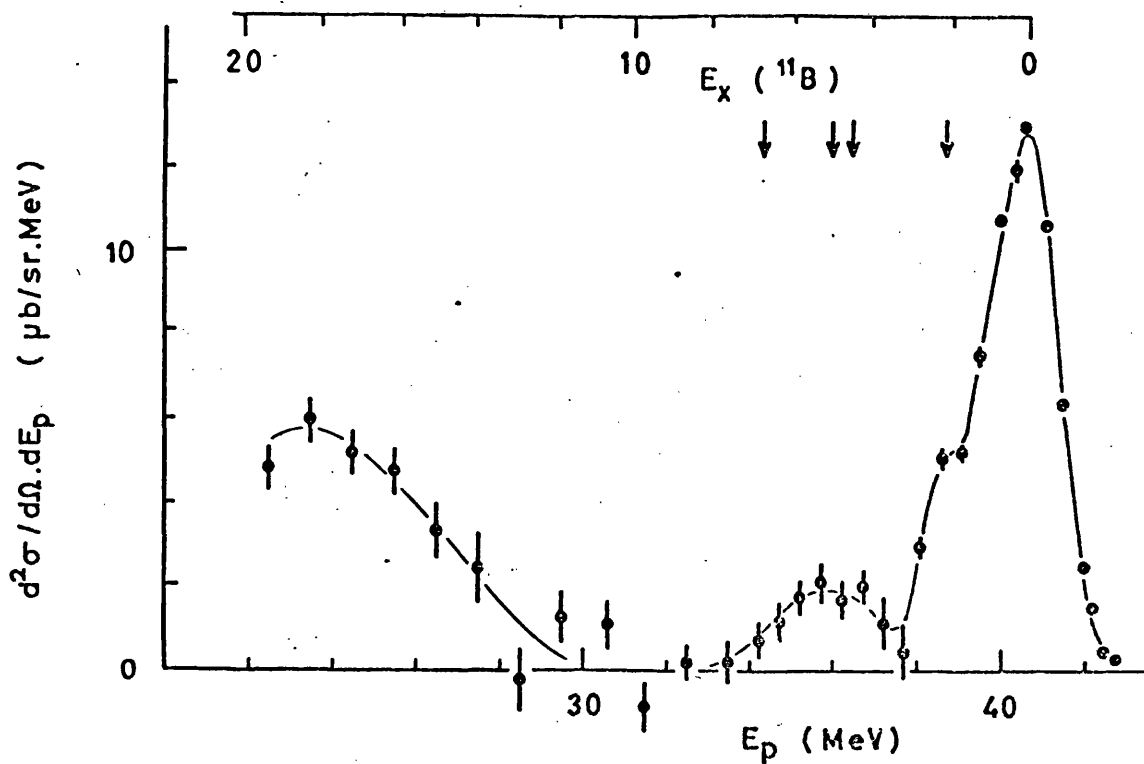


FIG. 1.4

The proton spectrum from the  $C^{12}(\gamma, p)$  reaction for  $E_\gamma = 60 \pm 1$  MeV,  $\Theta_{\text{lab.}} = 45^\circ$ . The excitation energy in the residual nucleus,  $B^{11}$ , is shown, and arrows indicate the low-lying states.

### 1.6 Other single nucleon knock-out reactions

All single nucleon knock-out reactions are capable of yielding information about the bound state from which the knocked-out nucleon was ejected <sup>9)</sup>.

The  $(e, e' p)$  quasi-free electron-proton scattering reaction <sup>10,52)</sup> is the single nucleon knock-out reaction which is most comparable with the  $(\gamma, p)$  reaction. The  $(e, e' p)$  reaction is just the  $(\gamma, p)$  reaction with a virtual photon substituted for the real photon. However, for a virtual photon energy and momentum may be chosen independently unlike for a real photon, and this leads to an extra degree of freedom <sup>10,11)</sup>. The  $(p, 2p)$  quasi-free proton-proton scattering reaction <sup>10)</sup> is similar to the  $(e, e' p)$  reaction. However, the  $(e, e' p)$  reaction has advantages over the  $(p, 2p)$  reaction in that the interaction with the nucleus of only one strongly interacting particle, the proton, is involved in the  $(e, e' p)$  reaction since the electromagnetic interaction is relatively weak; in the  $(p, 2p)$  reaction with its strongly interacting projectile and knocked-out proton absorptions of  $\sim 90\%$  are quite common. This means that the bound proton momentum distribution as deduced from an  $(e, e' p)$  experiment is "cleaner" than that deduced from a  $(p, 2p)$  experiment. However, the small interaction probability of the electron necessarily means that the  $(e, e' p)$  reaction cross-section is small compared with the  $(p, 2p)$  cross-section.

Other single nucleon knock-out reactions include the  $(p, d)$  and/.....

and  $(d, \text{He}^3)$  pick-up reactions, but these are not such good probes for momentum distributions due to the fact that the final particles, the deuteron or the  $\text{He}^3$ , are very much "dissolved" <sup>10)</sup> in the nucleus. In fact it has been shown <sup>9)</sup> that most of the deuterons produced by the  $(p, d)$  reaction at large angles are due to multiple scattering; the deuteron distribution therefore only very indirectly reflects the momentum distribution of the original bound neutron.

All these reactions yield spectroscopic factors, but it is the high momentum regions of the data which should most easily show short range effects. For a reasonably unambiguous interpretation only  $(e, e'p)$  experiments really can be considered because of distortion, and these coincidence experiments are difficult at high momentum transfer where the cross-sections are very low. The  $(e, e'p)$  experiment involving the highest momentum transfer is the experiment of Kübberling et al. <sup>12)</sup> at DESY which reaches 400 MeV/c, but it has poor resolution and cannot distinguish protons ejected from the different shells. At this momentum deviations from shell model predictions are apparent.

## 1.7 Experimental Considerations

The  $(\gamma, p)$  reaction is portrayed in Fig. 1.1. Ideally there is a beam of monochromatic photons of exactly known energy in the initial state and a means of detecting protons in the final state with an energy resolution such that all states in the residual nucleus can be separated. Beams of monochromatic photons are more difficult to obtain than beams of monochromatic charged particles, and this difficulty distinguishes photon experiments from charged particle experiments. The photon beam must be of a monochromaticity at least comparable with the desired separation of states in the residual nucleus.

At Glasgow positron annihilation and bremsstrahlung are the only methods of obtaining high energy photons<sup>13)</sup>. Positron annihilation in flight, the annihilation with electrons of a monochromatic beam of high energy positrons passing through some target material, produces, if only photons in a narrow forward cone are accepted, a photon spectrum with a sharp peak at about  $\frac{1}{2}$  MeV above the positron energy and a slowly rising low energy tail due to positron bremsstrahlung. But the photon yield is too low, principally because of the low conversion efficiency in the positron target in the accelerator, compared with the photon single-difference spectrum to be useful at high energies where the  $(\gamma, p)$  cross-section is low. This leaves bremsstrahlung, which may be used in several ways. The photon tagging technique, in which the energy of the secondary electron produced by the/.....

the bremsstrahlung process is measured in coincidence with the bremsstrahlung induced event, effectively gives photons whose monochromaticity is determined only by the accuracy to which the energy of the secondary electron can be measured. But this is only suitable for low count rates, and the high accelerator duty cycles required to reduce the random coincidence rates are not available. To obtain photons of reasonable monochromaticity from a bremsstrahlung beam requires some sort of difference or unfolding technique. Yield curve unfolding <sup>14,15)</sup> is much used. Here proton spectra are accumulated for bremsstrahlung with a whole series of closely spaced endpoint energies, and from these, by suitable unfolding machinery, the proton spectrum for photons whose energies are between the two highest endpoints is reconstructed. The Genoa-Turin group <sup>16,17,18)</sup>, for example, used such a technique with bremsstrahlung endpoint energies 2 MeV apart between 50 and 80 MeV. However, propagation of experimental errors through the unfolding procedure is a problem, and false structure can be generated. Because of the many measurements involved, this technique is slow. The single-difference technique is faster since only two bremsstrahlung spectra are involved in the subtraction. This technique is not new; Whitehead et al. <sup>19)</sup> used it almost twenty years ago. However, the single difference technique <sup>20)</sup> developed at this University and employed in the present experiments sets new standards in the degree of monochromaticity of the resulting photon difference spectrum. The FWHM of the photon peak is 2 MeV for peak energies/.....

energies between at least 50 and 100 MeV. This enables, for example, the cross-sections to the ground state and the 2.12 MeV first excited state of  $B^{11}$  in the  $C^{12} (\gamma, p) B^{11}$  reaction to be separately determined.

For the resolution of the experiment to be determined only by the photon source, the final state protons must be measured with considerably better energy resolution than the width of the photon source. This requires a magnetic spectrometer. The resolution of proton telescopes, as used, for example, by the Genoa-Turin group, is about 5% at best,  $\sim 2$  MeV for a 40 MeV proton, resolution much worse than the 1% of the magnetic spectrometer as used in this experiment.

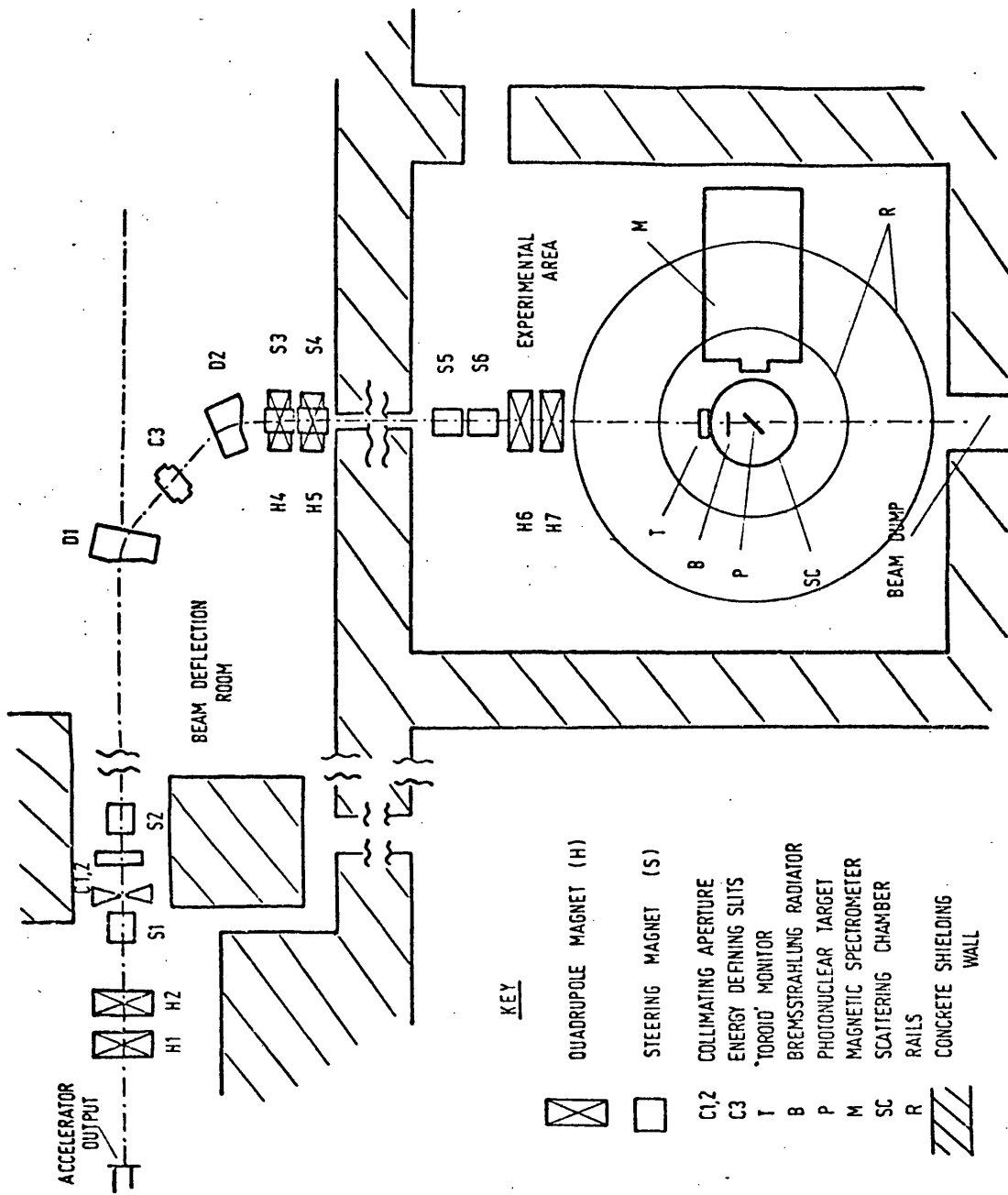
The cloud chamber, as used by Taran, Gorbunov and Osipova<sup>21,22,23)</sup> has some advantages when used for photodisintegration work. The energies and angles of all the charged reaction products may be measured, and ordinary bremsstrahlung may be used as the source of photons. Data on all possible photodisintegration processes may be obtained. Disadvantages, of course, are the large effort which must be devoted to the analysis and the low data collection rate.

1.8 Summary

The ( $\gamma, \beta$ ) experiments, the theoretical predictions and the conclusions are presented in the following four chapters. Mathematical machinery has been consigned to appendices. Chapter 2 describes the experimental system, Chapter 3 describes the data analysis procedures, Chapter 4 presents the results of the experimental measurements, and in Chapter 5 experiment is compared with theory and conclusions drawn.

CHAPTER 2 THE EXPERIMENTAL SYSTEM2.1 The experimental system in general.

The general experimental arrangement<sup>24)</sup> is shown in Fig. 2.1. Electrons from the accelerator are transported from the accelerator vault into the beam deflection room, where they are bent through  $90^\circ$  and energy analysed by energy defining slits placed after the first bending magnet. The energy analysed beam is then transported into the experimental igloo, where the scattering chamber and magnetic spectrometer are situated. Thick walls,  $\sim 8$  feet of concrete, separate the accelerator vault from the beam deflection room and the beam deflection room from the igloo. In the scattering chamber, the beam passes through a bremsstrahlung radiator producing a narrow cone of photons which is intercepted by the photonuclear target. Photoprotons from the target are detected by the magnetic spectrometer which carries a set of scintillation counters in its focal plane. The signals from the counter photomultipliers are carried by coaxial cables to the control room, where the signals are pulse height analysed. Finally the pulse height spectra are stored in a computer.



- KEY**
- QUADRUPOLE MAGNET (H)
  - STEERING MAGNET (S)
  - C1,2 COLLIMATING APERTURE
  - C3 ENERGY DEFINING SLITS
  - T "TOROID" MONITOR
  - B BREMSSTRAHLUNG RADIATOR
  - P PHOTONUCLEAR TARGET
  - M MAGNETIC SPECTROMETER
  - SC SCATTERING CHAMBER
  - R RAILS
  - CONCRETE SHIELDING WALL

FIG. 2.1 General layout of experimental system

## 2.2 Accelerator.

The electron linear accelerator is of the pulsed r.f. travelling wave type. There are three sections to the machine, each capable of imparting approximately 40 MeV to the electron beam, and each fed by a 20 MW (peak) klystron. The maximum energy attainable by the accelerator depends on the beam current and on the quality of the klystrons and the associated power electronics, but is typically 120 - 130 MeV. The electrons emerge from the accelerator with an energy spread of  $\sim 2\%$ .

The accelerator was pulsed at 100 p.p.s. phase-locked with the A.C. mains supply. The r.f. pulse length was 3.5  $\mu$ sec, giving a duty cycle of  $3.5 \times 10^{-4}$ . Peak currents of  $\sim 150$  mA are used, and with .75% energy analysis the mean current is  $\sim 15$   $\mu$ A. Phase-locking is important because the pulse forming networks which generated the voltage pulse applied across the klystrons were charged from power supplies which had some 50 c/s <sup>mains</sup> frequency ripple on their outputs. Also, the heater of the electron gun at the beginning of the accelerator was fed by 50 c/s A.C. These can lead to a 50 c/s modulation of the machine energy if the phases of the firing pulses are not chosen properly, and two distinct energies of electrons can be produced with a consequent reduction in the analysed current.

An attempt was made to obtain more current by pulsing the accelerator at 150 p.p.s. phase-locked with the A.C. mains supply.  
It/.....

It was found that an increase in current was possible but that the spacing of the three pulses had to be very carefully set up to allow the different voltages reached by the delay lines in the modulators for unequal intervals between pulses to compensate for the 50 c/s ripple on the D.C. charging supply and the gun.

### 2.3 Beam handling and energy analysis system.

The beam handling and energy analysis system is shown in Fig. 2.1. A pair of quadrupoles H1, H2 located just after the output of the accelerating structure focuses the beam through the rectangular collimating aperture C1, C2 which is made up of two sets of adjustable slits mounted at right angles. This aperture is the object for the energy analysis system, composed of bending magnet D1 and energy defining slits C3. The  $45^\circ$  magnet D1 has a uniform field and an exit pole edge rotation of  $26.5^\circ$ , which together produce a radial and an approximate vertical image at the position of the slits. The width of the energy defining slits C3 in conjunction with the size of the collimating aperture C1, C2 determines the energy resolution. Typically the energy resolution used is in the range .4 - 1.0%. Using the energy defining slits as an object, the second bending magnet D2, a mirror image of D1, together with the quadrupoles H4, H5 bend the beam through a further  $45^\circ$  and produce an approximately parallel beam for travelling the relatively long distance from the beam deflection room to the experimental area. There, using quadrupoles H6, H7, the energy analysed beam is finally focused on to the target. There are steering magnets throughout the system to assist in guiding the beam.

When the system is set up properly, a considerably diminished image of the collimating slits is produced at the target. This ensures that the electron energy and the position and size of the beam spot are unaffected by variations in accelerator performance.

The energy analysis system is basically that of Penner<sup>25)</sup>, but without the central quadrupole, which precludes achromaticism. In practice, this omission has no serious consequences.

Since the energy spread of the electrons produced by the accelerator substantially exceeds the desired spread, considerable power is dissipated in the slit jaws. This necessitates water-cooling.

The magnetic field in the bending magnet D1 is monitored using an N.M.R. probe. This probe is situated in a position which is reproducible to  $\frac{1}{2}$ mm which ensures a field monitoring constancy good to .003%. The frequency of the N.M.R. r.f. oscillator at resonance is used to measure the electron beam energy. The calibration of the energy analysis <sup>system</sup> is described in Appendix 2.

#### 2.4 Scattering Chamber.

The scattering chamber contains both the bremsstrahlung radiator and the target ladder, and is shown in Fig. 2.2. It is an evacuated aluminium cylinder, 10" in height and 18" in diameter with mountings for windows every  $7\frac{1}{2}^{\circ}$ . Normally, windows consisting of .001" kapton are mounted, but for some measurements, e.g. the alpha-calibration (Appendix 1), vacuum coupling is used between the scattering chamber and the spectrometer. The energy loss of 60 MeV protons in the windows is .03 MeV, but the 5 MeV  $\alpha$  - particles would almost stop. The target is observed through one of the windows by a television camera, and the picture is displayed on a monitor in the control room. After striking the photonuclear target, the beam passes through the .01" aluminium exit port of the scattering chamber and travels through air to the entrance of the beam dump about two yards away.

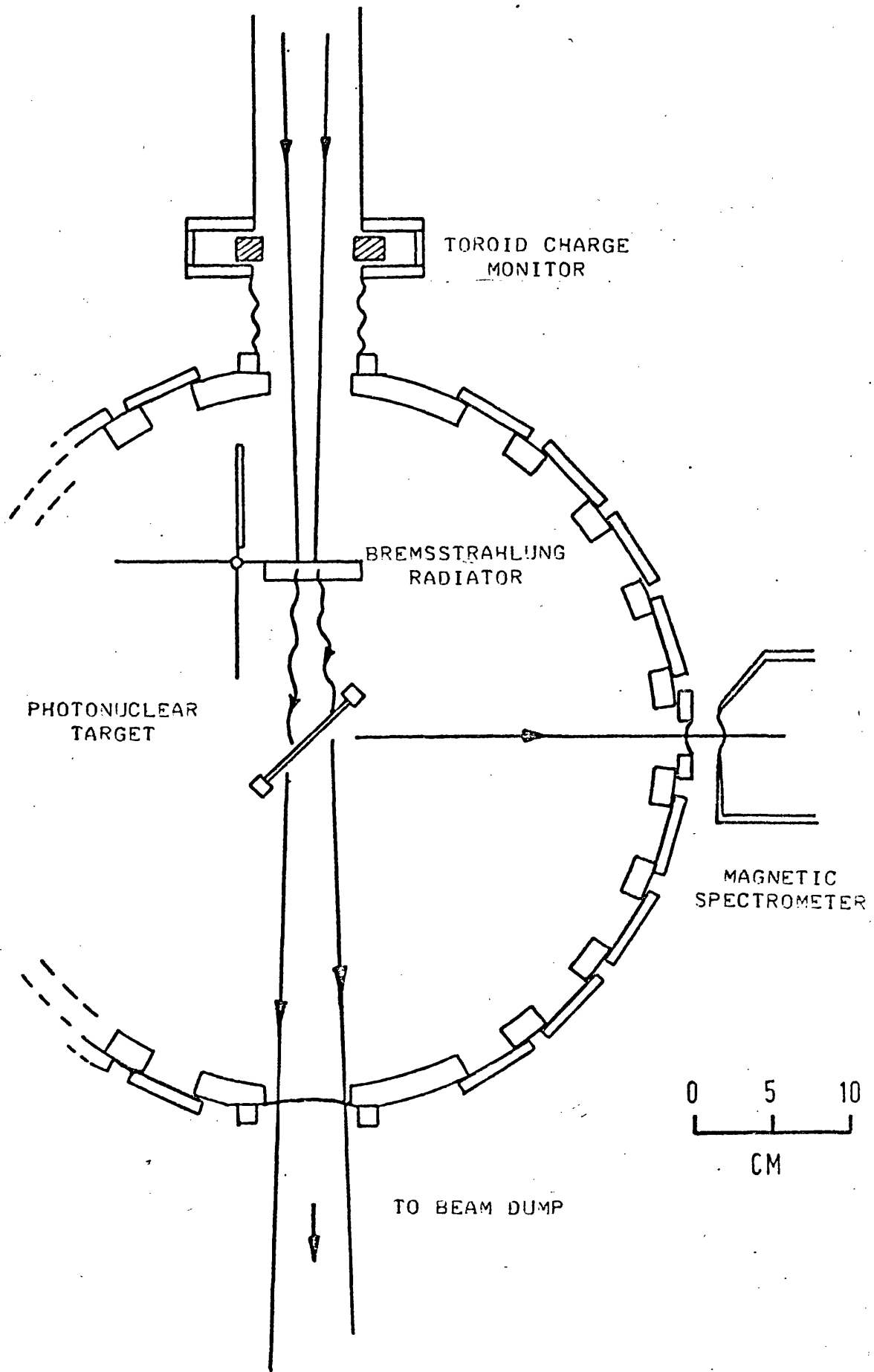


FIG. 2.2

SCATTERING CHAMBER AREA

## 2.5 Bremsstrahlung radiators.

The electron beam, with a known energy spread after analysis, enters the scattering chamber (see Fig. 2.2) and hits the current bremsstrahlung radiator. A total of four radiators may be mounted on the "radiator rotator", a device composed of a vertical shaft carrying four holders each in a vertical plane at right angles to its neighbours. The shaft is rotated by an electric motor mounted on the top of the scattering chamber. Mounted on the same shaft is a variable resistor, which together with a similar variable resistor in the control room forms a Wheatstone bridge. The radiator rotator may thus be set remotely to any angle. The reproducibility is  $1^\circ$  or .02% in radiator thickness.

Normally three radiators, Be, Al and Au, are mounted, the remaining fourth position being left blank to enable both visual inspection of the beam profile on a zinc sulphide or beryllium oxide target downstream from the radiator in the target ladder and measurement of electrodisintegration proton yields.

## 2.6 Photonuclear targets.

The photonuclear targets are mounted one above the other in the target ladder at the centre of the scattering chamber. The targets are nominally  $2\frac{1}{2}$ " wide by  $1\frac{1}{2}$ " high, and some have cross-lines drawn on them to locate the beam spot. By raising or lowering the target ladder pneumatically, any one of the targets may be selected for bombardment. The amount to which the position of the target ladder is reproducible is .1mm vertically.

The vertical position of the target is important because this determines the position of the beam spot relative to the spectrometer. A change in object position (the beam spot on the target) means a change of image position (the focused protons in the spectrometer focal plane) which is equivalent to a shift in energy. The above-mentioned reproducibility of .1mm is equivalent to a .01% change in energy, which is negligible. A telescope mounted on the spectrometer (see Fig. 2.3) may be used to align the targets.

The target ladder is made as thin as possible to minimise the yield of photoprotons from the target ladder itself. The photo-production of protons from the aluminium target ladder will be seen as a continuation of the proton spectrum past the endpoint for the  $C^{12}$  and  $O^{16}$  targets. The  $Q$  of the  $(\gamma, p)$  reaction in  $Al^{27}$  is -8 MeV; for  $C^{12}$  and  $O^{16}$  it is -16 and -12 MeV respectively). This effect has been seen, but only amounts to  $\sim .1\%$  of the real proton spectrum.

The/.....

The azimuthal position of the target ladder is a compromise between high proton energy losses and spectrum smearing and the target ladder's aluminium sides intercepting the beam. The configuration chosen has the normal to the target at  $45^\circ$  to the beam line.

The targets mounted in the target ladder were appropriate combinations of the following: a zinc sulphide target for inspection of the beam profile, a beryllium oxide target for the  $O^{16} (\gamma, p)$  experiment and for beam profile inspection at higher currents, a second beryllium oxide target for possible normalisation purposes as explained below, a thin (.01-.02") graphite target for the  $C^{12} (\gamma, p)$  experiment, a thick graphite target of well known and uniform thickness against which to normalise the thinner graphite target, and a lithium metal target (separated isotope  $Li^7$ ) for the  $Li^7 (\gamma, p)$  experiment.

The lithium target was made by rolling the lithium metal in a milled slot. Using the slot depth as the target thickness, this was  $108.8 \pm .3 \text{ mg/cm}^2$ . The thickness of the thin graphite target, made by machining away the central region of a thicker piece of graphite, was measured by comparing the proton yield from it with the yield from the thicker graphite target. Its thickness was  $74.4 \pm .8 \text{ mg/cm}^2$ . The beryllium oxide used as the oxygen target was obtained from the manufacturer with a uniformity stated to be  $5 \times 10^{-6}$  (<.1%). This was checked by measuring proton yields produced by bremsstrahlung with the beam spot at many different points on the target. Its thickness, 57.3/.....

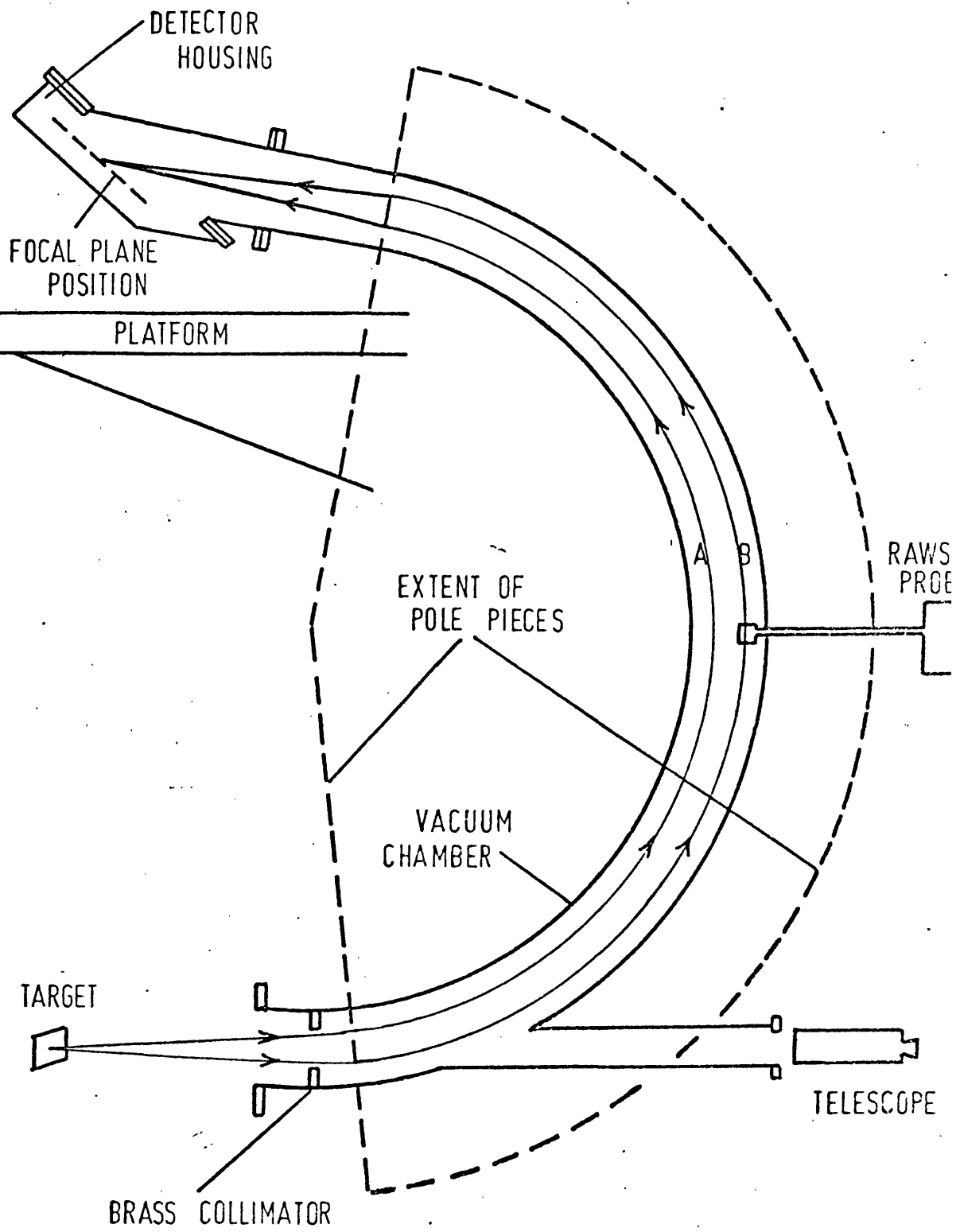
$57.3 \pm .3 \text{ mg/cm}^2$ , was simply obtained by measuring its area and weighing it. Another, <sup>nominally</sup> ~~normally~~ identical, beryllium oxide target was included in the target ladder for normalisation purposes since the beryllium oxide developed a brown burned appearance with time at the position of the beam spot. This second target was used only occasionally to check the ratio of its proton yield to that of the normal target. This was always found to be unity to within the statistical errors, thereby also confirming the assumption of uniformity.

## 2.7 Magnetic spectrometer.

The magnetic spectrometer is based on a design of Penner<sup>26)</sup>. Its parameters are listed in Table 2.1 and a diagram is given in Fig. 2.3.

The maximum magnetic rigidity of a particle which can be accepted by the spectrometer is  $\sim 375$  MeV/c, and a highly stabilised (3 parts in  $10^5$ ) 170V, 700A power supply provides the current for the windings. Both the spectrometer magnet windings and the power supply are water cooled. The spectrometer is pumped to a vacuum of  $\sim 10^{-4}$  torr, for which energy losses and scattering are negligible, even for a 5 MeV  $\alpha$ -particle. The spectrometer is mounted on a motor-driven carriage running on two concentric rails round the scattering chamber. Normally there is a small air gap,  $\sim \frac{1}{2}$ " , between the spectrometer entrance window, .001" mylar, and the scattering chamber window. The energy losses of a proton in the air gap and the spectrometer entrance window are both approximately equal to the energy loss in the scattering chamber window.

In the focal plane of the spectrometer, the number of counters, their width, and the spacing between them are decided by compromise. There is no point in having very narrow counters giving each counter an energy bite much less than the intrinsic resolution of the photon spectrum. Since pulse height spectra from the counters are accumulated, the number of counters which can be employed is limited by/.....



A,B: TWO EXTREME RAYS OF THE SAME MOMENTUM

FIG. 2.3

MAGNETIC SPECTROMETER

by the amount of memory available in the computer. The arrangement used is ten counters, each having a momentum bite of  $\sim .45\%$ , and with the spacing between one counter and the next  $\sim .6\%$  in momentum. Because a large region,  $\sim 6\%$ , of the focal plane is covered by the counter ladder, the images produced at the extreme counters in the ladder suffer in quality. However, by measuring the relative efficiencies (Appendices 4,5) of the counters this effect is almost completely eliminated.

The solid angle subtended by the spectrometer at the target, 10.00 milliradians, is defined by placing a brass collimator at the effective pole edge of the magnet. With this arrangement it has been experimentally verified<sup>1)</sup> that, to considerably better than 1%, no charged particles are lost between either of the two counters nearest the centre of the focal plane and the collimator.

The magnetic field is measured using a Rawson-Lush gaussmeter with the probe situated near the outer edges of the pole pieces. The stability of this gaussmeter is  $\sim 1$  part in  $10^5$ . The presence of the probe reduces the effective solid angle from 10.00 to 9.94 milliradians.

The measurements of the spectrometer parameters were made using a small  $\text{Pu}^{238}$   $\alpha$ -source and are described in ref. 1.

For/.....

# MAGNETIC SPECTROMETER CHARACTERISTICS

	theoretical	measured
field index $n$	.5	
field index $\beta$	.25	
radius	80 cm	
deflection angle	169.8 °	
image distance for object distance = 65.28 cm	65.28 cm	65.49 ± .25 cm
vertical (along focal plane) magnification	-1.00	-.95 ± .02
horizontal magnification	-1.00	-1.02 ± .02
dispersion	4.00	4.02 ± .06
focal plane angle	33° 29'	34° 27' ± 1° 36'
intrinsic resolution	.02%	< .05%

TABLE 2.1

For the present experiment, the spectrometer calibration had to be extended to higher momenta than any previously encountered. It was found that the calibration (magnetic rigidity as a function of magnetic field) became definitely non-linear towards maximum field due to saturation of the iron. The energy calibration of the spectrometer is described in Appendix 3.

For measurements using photons of about 90 MeV or greater, an absorber,  $\sim 1 \text{ gm/cm}^2$  of polythene, is placed, in air, between the spectrometer and scattering chamber to reduce the energy of the photo-protons. This absorber is clearly necessary if the proton momentum exceeds the upper limit of 375 MeV/c mentioned above. However, the absorber is also desirable when the proton momentum is near this limit because the spectrometer field may then be reduced from a value at which the iron is beginning to saturate.

## 2.8 Counters and counter ladder

The ten counters are mounted in the counter ladder in the focal plane of the spectrometer (see Fig. 2.4a). Each counter is block of NE102A plastic scintillator 6.0 x 2.5 x 1.5 cm and is coupled to a photomultiplier, type XP1110, encased in a mu-metal shield. The anode signal is taken to the control room by double shielded coaxial cable. The scintillator is mounted in vacuum and is optically coupled via a perspex light guide and a perspex vacuum window to the photomultiplier mounted in air (see Fig. 2.4b). Each scintillator is covered with thin aluminium foil (  $\sim .001$ " thick) to ensure good light collection, and a small slit is cut in the foil at the centre of the counter. This foil causes a negligible energy loss for protons, but defines the centre of the counter for the relatively low energy  $\alpha$ -particles used in the  $\alpha$ -calibration (Appendix 1.)

The counters are mounted every 2 cm along the ladder. This means that the ratio of counter bite to counter spacing is  $\frac{1.5 \text{ cm}}{2.0 \text{ cm}} = \frac{3}{4}$ . At any one spectrometer field setting the relative momenta seen by each of the counters at their centres is given by the  $\alpha$ -calibration which leads to the figures, quoted in the previous section, of  $\sim .6\%$  in momentum for counter spacing and  $.6 \times \frac{3}{4} = .45\%$  for the momentum bite. The ten counters, placed symmetrically with respect to the central orbit, are numbered 0 to 9 inclusive with counter 0 seeing the lowest energy particles at a given spectrometer field. (Therefore in counter number space the number of a counter on the central orbit is  $4\frac{1}{2}$ .)

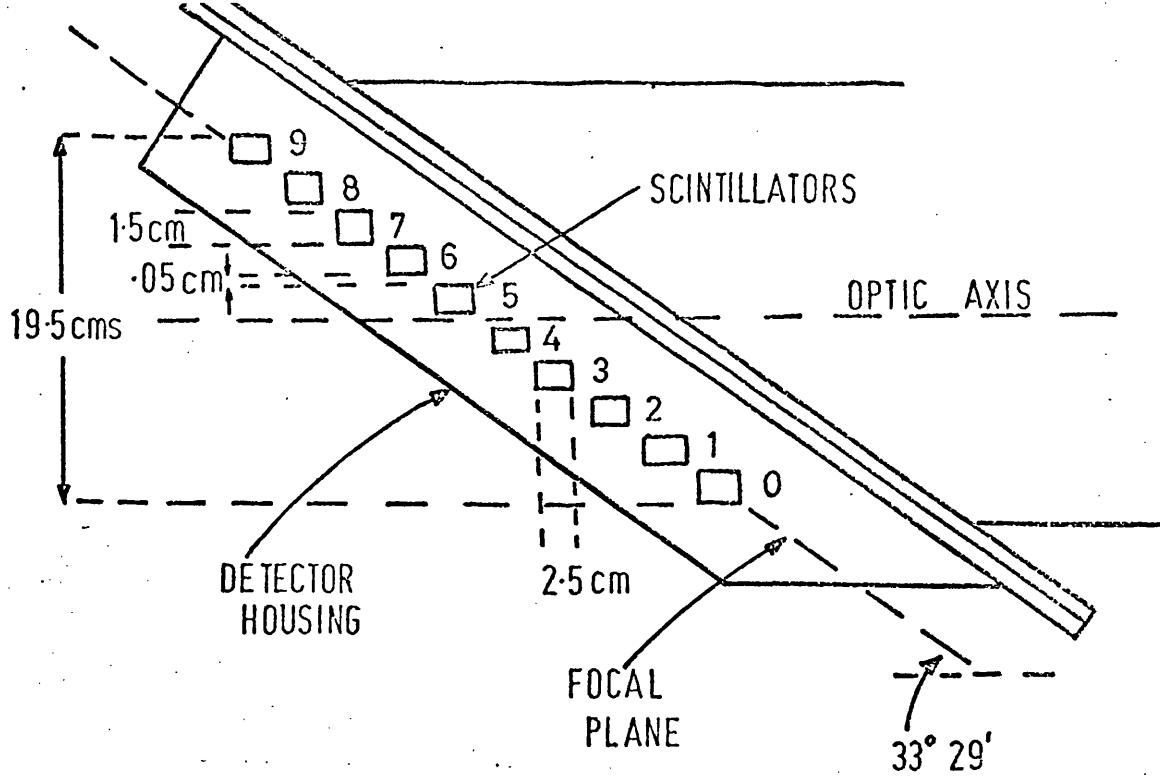


FIG. 2.4a Ladder counter and housing

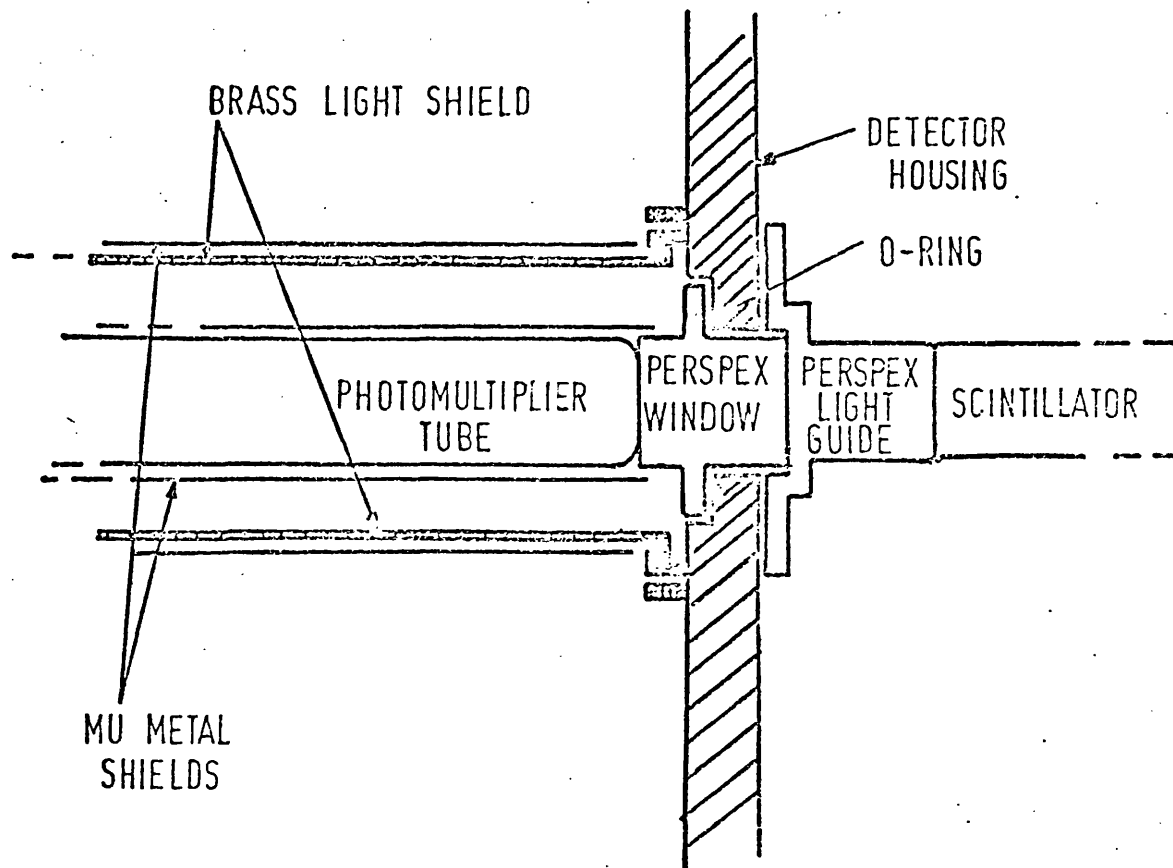


FIG. 2.4b Scintillation counter assembly (actual size)

Each counter is characterised by its own efficiency. This is factored into two parts, a general absolute efficiency involving multiple scattering and inelastic nuclear interactions in the scintillation material (Appendix 6), and a particular relative efficiency (Appendices 4,5) involving variations in dispersion etc. across the focal plane and loss of protons, due to incorrect magnetic field configurations, between the counters and the spectrometer entrance collimator. As discussed in section 2.7, there is no loss of protons between the centre of the focal plane and the collimator, and so for a counter at the centre of the focal plane the relative efficiency is unity.

The counters will stop protons with energies up to 55 MeV. Thereafter, as the proton energy increases, less and less energy is deposited in the counters, and this can finally cause difficulty in separating proton and deuteron peaks in the counter pulse height spectra. For example, 66 MeV protons deposit 33 MeV in the counters, the energy of a deuteron of the same magnetic rigidity. The absorber between the spectrometer and the scattering chamber, mentioned in section 2.7 in connection with high energy protons, is additionally useful here in separating such proton and deuteron peaks since the deuterons lose much more energy than the protons in the absorber.

Considerable shielding, placed both around the counters and around the various sources of background radiation, is required to reduce/.....

reduce the background at the counters to an acceptable level. Around the counters themselves approximately 4" of lead and 1' of borated paraffin wax is placed. Screening is also placed around three other sources of background radiation: firstly, scattered radiation associated with the beam where it just enters the experimental area, secondly, scattering when the beam passes through the bremsstrahlung radiator and the photonuclear target which are in the scattering chamber about 4' below the spectrometer focal plane, and thirdly, radiation from the beam dump. In addition to the effect of the shielding, the background is further reduced by the fact that pulses are only accepted from the counters for the duration of the beam pulse.

## 2.9 Charge Monitor.

The charge monitor used in these experiments was a non-intercepting beam current integrator<sup>27)</sup>. This is composed of a toroidal current transformer the primary of which is the electron beam, a linear gate which is only open for the duration of the beam pulse, and a current integrator whose digital output is scaled. Fig. 2.5 shows the arrangement. The toroidal transformer is placed just upstream from the scattering chamber as shown in Figs. 2.1 and 2.2.

The signal from the secondary of the current transformer or toroid is amplified, before transmission to the control room where the linear gate and current integrator are situated, by a low input impedance preamplifier mounted very close to the toroid itself. The preamplifier has to be encased in lead because of the high radiation levels experienced in the experimental area in the presence of the beam. A.C. coupling is used both between the current transformer and the preamplifier input and between the preamplifier output and the linear gate to minimise D.C. drift. The linear gate removes undershoot and any spurious pick-up between beam pulses. The scaler which is fed by the digital output of the integrator has automatic stop facilities incorporated in it, and these are used to ensure that each run is performed for the same amount of charge delivered to the bremsstrahlung radiator.

A high/.....

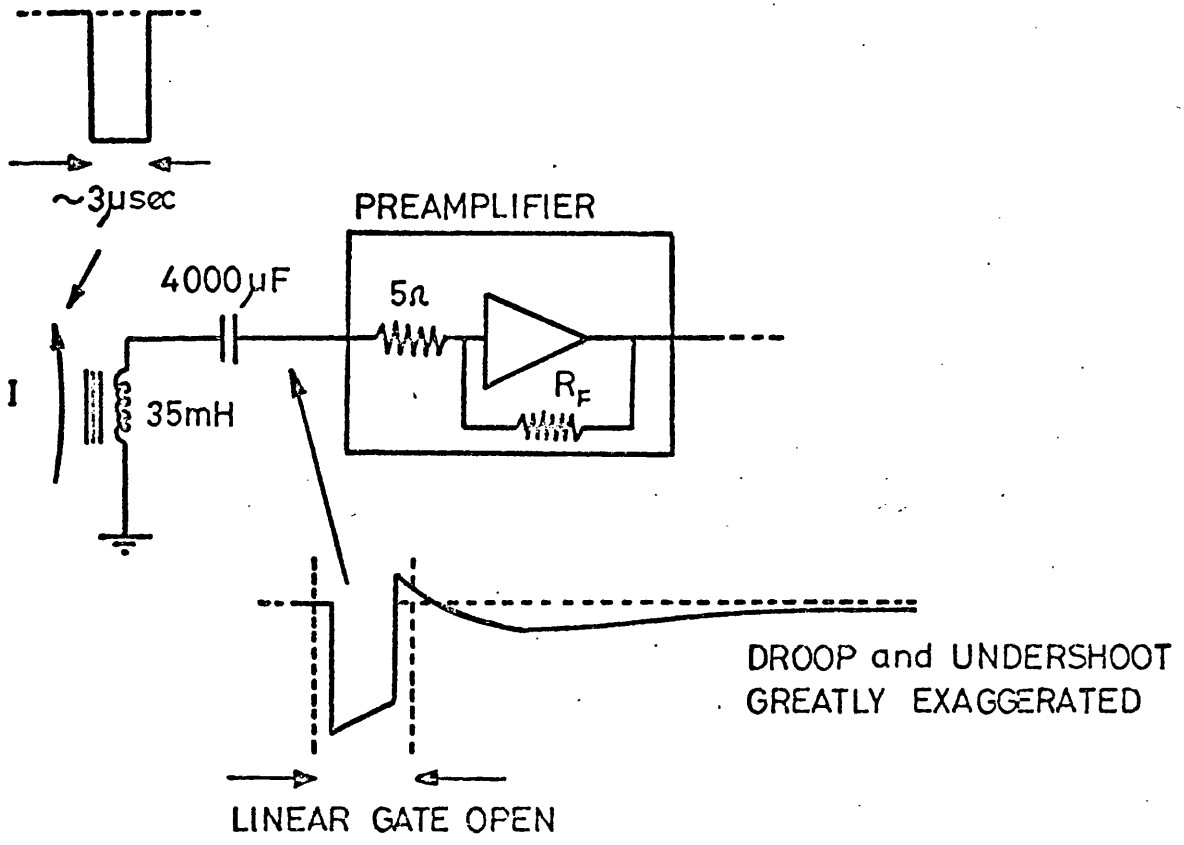
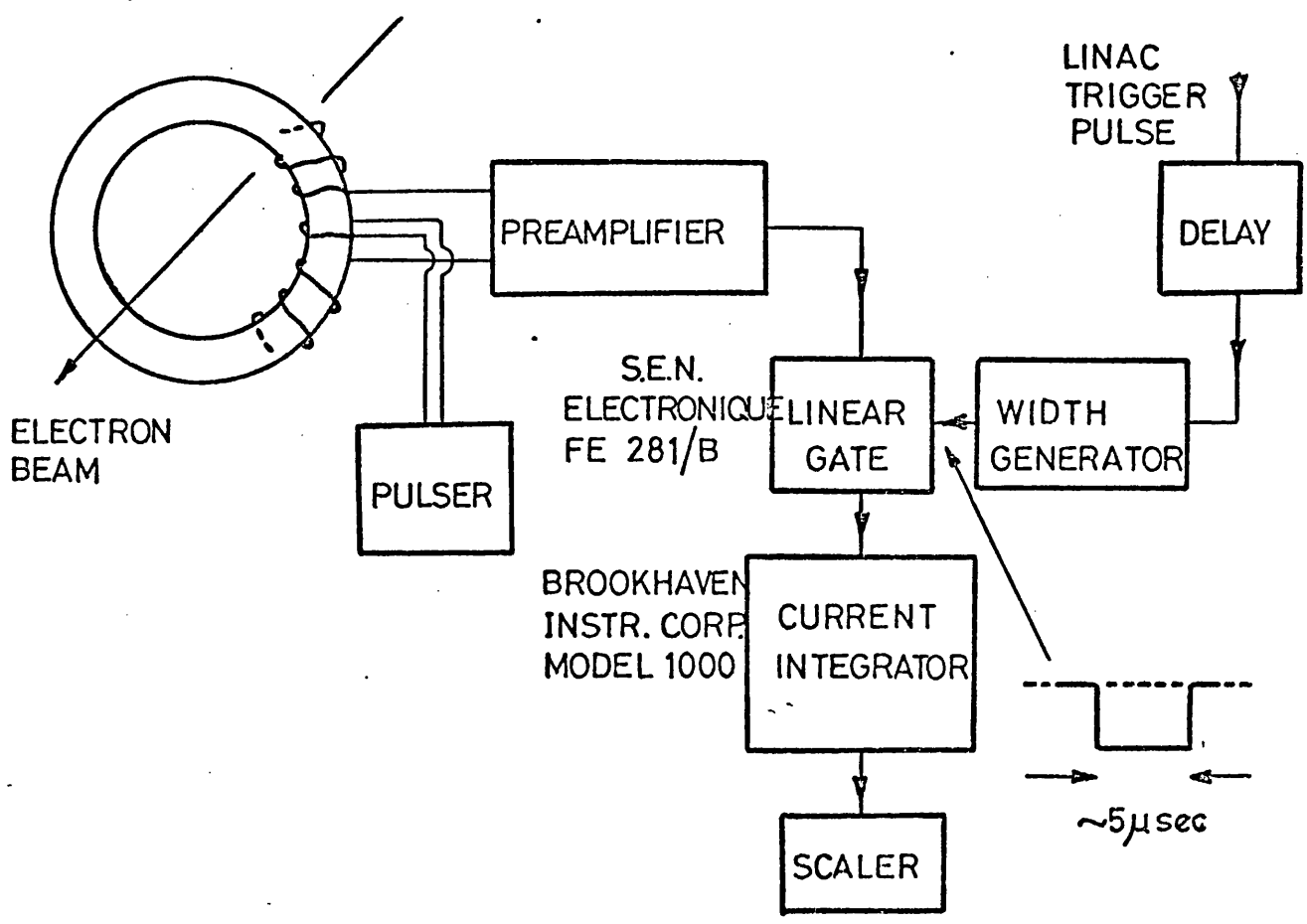


FIG. 2.5

A high standard of performance is required from the charge monitoring system. The toroid system is calibrated against a Faraday cup whose efficiency is .996 at the electron energies encountered<sup>28)</sup>. Over a range of mean beam currents of 0-12  $\mu\text{A}$ , the linearity and long term stability were found to be good to .5%, and this is satisfactory. Linearity is important because the analysed beam current wave form is anything but rectangular and varies throughout each run.

To guard against drift of the toroid system, a single turn calibration loop is incorporated in the toroidal current transformers. This can be fed by a precision pulser, and after the end of every few runs, the pulser is connected to the calibration loop and the response of the toroid checked.

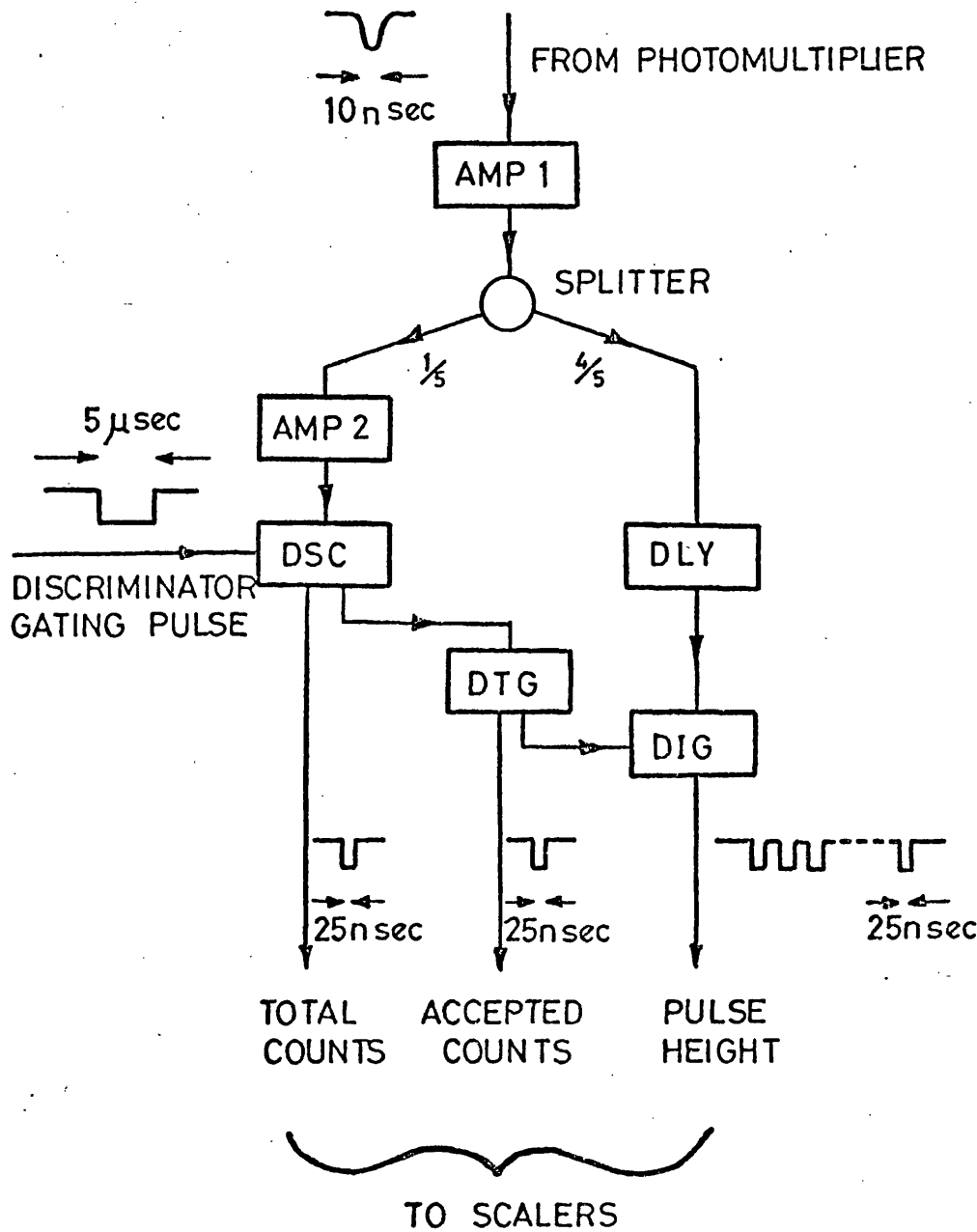
## 2.10 Signal processing electronics

One channel of the signal processing electronics is shown in Fig. 2.6. There are ten such identical channels.

The pulse from the anode of the scintillation counter photomultiplier is first amplified in a variable gain fast amplifier. The signal path then divides, the amplified pulse being fed to both a discriminator and a digitiser. The discriminator is set to remove small background pulses; the digitiser will only digitise a pulse present at its linear input if a gating pulse is simultaneously present at its gate input. The process of digitising can take up to  $\sim 20$   $\mu\text{sec}$ , a time considerably longer than the duration of the 3  $\mu\text{sec}$  beam pulse. Therefore only one counter pulse every beam pulse can be digitised. By feeding the output of the discriminator to the gate input of the digitiser through the dead time generator, a device which produces at its output a replica of a short pulse applied to its input if a similar pulse were not present in the previous 50  $\mu\text{sec}$ , only one counter pulse above the discriminator threshold is digitised every beam pulse.

The digitiser produces a train of output pulses, the number of pulses in which is proportional to the height of the counter pulse. The delay precedes the linear input of the digitiser to compensate for the propagation delay through the second amplifier, the discriminator and the dead time generator. The total number of counter pulses above the/.....

SIGNAL PROCESSING ELECTRONICS - ONE CHANNEL



AMP 1, AMP 2

LECROY VARIABLE GAIN AMPLIFIER TYPE 133B

DSC

EG&G DIFFERENTIAL DISCRIMINATOR TYPE TD101/N

DTG

DEAD TIME GENERATOR

DLY

EG&G VARIABLE DELAY TYPE DB 463

DIG

LECROY GATED DIGITISER TYPE 143 B

FIG. 2.6

the discriminator threshold is provided by the output of the discriminator. The number of pulses accepted for pulse height analysis is provided by the output of the dead time generator. The ratio of these two numbers defines the dead time correction.

Thus from each counter every beam pulse three numbers are produced:

- 1) total number of counts 0,1,2, but  $\geq$  accepted counts
- 2) accepted number of counts 0,1
- 3) a number proportional to the height of the pulse  
(if any) in 2).

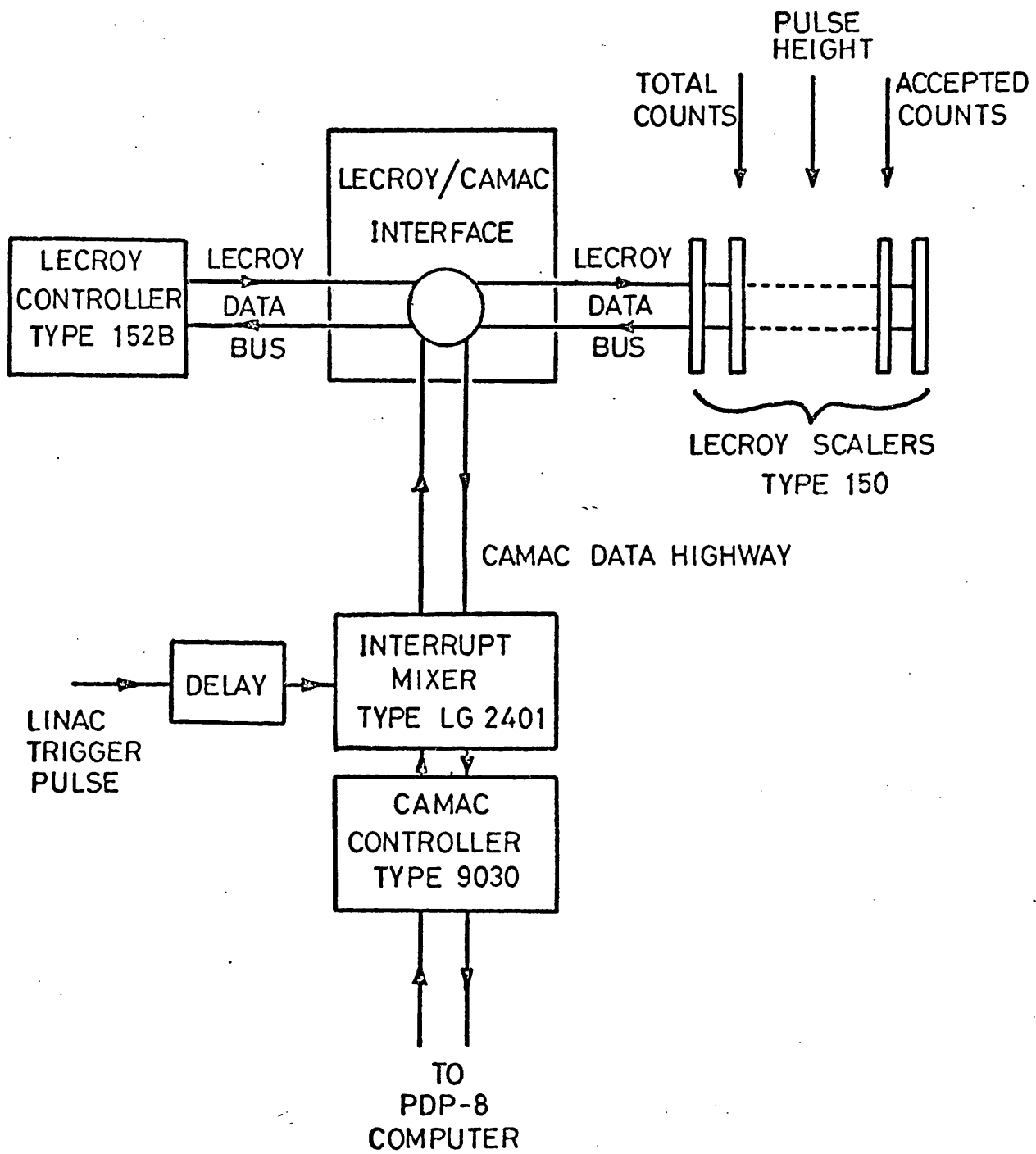
The thirty numbers which characterise the response of the counter ladder to a beam pulse are stored in a Lecroy type 150 scaling system. At the end of each beam pulse the scalers are read by the computer as described in the next two sections.

## 2.11 Computer interface

The interface used to transfer information from the Lecroy scaling system to the computer was composed of commercial CAMAC modules and a custom built Lecroy/CAMAC interface, and is shown in Fig. 2.7. The Lecroy/CAMAC interface allows either the Lecroy controller or the CAMAC controller to control the Lecroy scaling system, and this interface is itself controlled by the CAMAC controller. The computer controls the CAMAC controller which is treated as a peripheral device such as a teletype.

The Lecroy scalers are connected in a "daisy-chain" pattern in which, in response to suitable commands, each scaler in turn presents the number contained in it to the Lecroy data bus. Scalers 1-10 contain the pulse height information from the ten counters, scalers 11-20 the accepted number of counts, and scalers 21-30 the total number of counts. The thirty scalers are read by the computer after every beam pulse.

After each beam pulse is over, an interrupt is sent through the interrupt mixer to the computer. The interrupt signal is the linac trigger pulse delayed by about 50  $\mu$ sec to ensure that the pulse trains from the digitisers are over. The CAMAC controller is then given control of the Lecroy scaling system. The scalers are inhibited so that no further counts can be accumulated. Then the contents of each scaler presented in turn on the Lecroy data bus are read by computer. After/,.....



COMPUTER INTERFACE ELECTRONICS

FIG. 2.7

After the last scaler has been read, all the scalers are cleared in readiness for the next beam pulse.

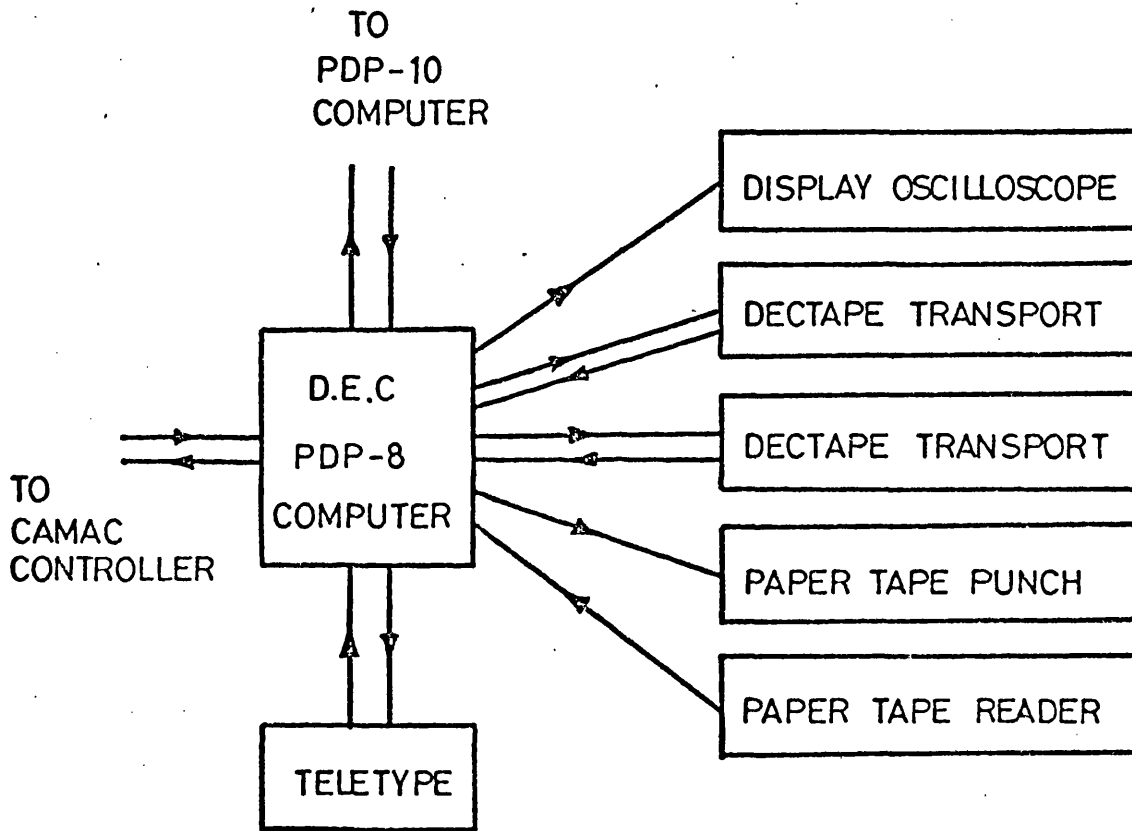
Canberra type 1492 scalers are used for accumulating the charge delivered to the bremsstrahlung radiator, the time elapsed, the number of beam pulses, etc. By tying the inhibit line of these scalers to the inhibit line of the Lecroy system, it is arranged that a single push-button will start the entire data acquisition machinery. By using the automatic stop facility on the Canberra scalers, all data collection ceases when some predetermined amount of charge has been delivered to the bremsstrahlung radiator.

## 2.12 Computer programme

Data acquisition is handled by a D.E.C. PDP-8 computer (see Fig. 2.8). Normally the computer performs two simultaneous functions: firstly, reading the scalers and updating the counter pulse height spectra stored in the computer memory, and secondly, displaying the spectra for on-line visual analysis.

On receipt of an interrupt request from the interface, the computer jumps out of the display routine and reads the scalers as described in section 2.11. As the contents of the scalers are successively deposited in the accumulator, the appropriate memory locations are updated: for a total or accepted number of counts, the contents of the relevant memory location is increased by an amount equal to the number received from the scaler, while for a number representing a pulse height (a channel number) the memory location representing the contents of that channel is increased by one. After reading all thirty scalers, the computer returns to the display routine.

The form of the display and the data displayed may be changed at will. By typing appropriate commands on the teletype keyboard, any of the ten counter spectra or the spectra of the upper or lower set of five counters may be presented to an oscilloscope display. The scale of the display is set by the computer switch register. The ability to monitor all the counter spectra as they accumulate is most useful. A typical spectrum, showing protons, deuterons and tritons, is shown in Fig. 3.2.



COMPUTER CONFIGURATION

It may happen that, because of the 12-bit word length of the PDP-8, the contents of some channel or channels may overflow. The computer programme tests for this condition, and, if found, increases the contents of an overflow channel by one. The overflow channel ~~is~~ used is channel 1 of the 200-channel pulse height spectrum. In subsequent analysis, the proton peak area is increased by an addend of the product of  $2^{12}$  and the number of overflows found.

The programme used for data acquisition began as a standard D.E.C. kicksorting programme, but has been considerably modified and extended. For example, a facility has been included for communicating with the larger D.E.C. PDP-10 computer through the PDP-8 teletype during data accumulation and display.

After every run, the ten spectra stored in memory may be typed out on the teletype, written out on DEC-tape, punched out on paper-tape, or transferred directly to magnetic storage on the PDP-10 for further analysis.

CHAPTER 3 DATA ANALYSIS3.1 Introduction

For all experimental data accumulated, the same analysis procedure was followed. The general order is:

- 1) determination of the number of protons incident on the counters by finding the areas of the proton peaks in the pulse height spectra accumulated in the computer (the raw data),
- 2) determination from 1) of the experimental proton yield spectrum differential in proton energy and solid angle,
- 3) calculation of the photon spectrum incident on the photonuclear target,
- 4) calculation from 3) of the shape of the proton spectrum seen by the spectrometer,
- 5) fitting of the calculated spectrum shape to the experimental spectrum to obtain the cross-section.

### 3.2 Determination of proton peak area from raw data

In general, the proton peak whose area is required sits on a rising background. The area of the proton peak must then be found by adding up all the counts in the channels spanning the peak (the "added" region) and subtracting the appropriate contribution due to the background. This is shown in Fig. 3.1.

The amount to be subtracted from the total area under the peak, the contribution due to the background, is obtained by defining two regions on either side of the peak, "fitted" regions, and fitting the same function to both these regions simultaneously. This procedure interpolates the background under the peak which may then be subtracted to obtain the area due to the protons above. Each counter has a 200-channel spectrum, and the functions fitted are series of Legendre polynomials,

$$a_0 P_0 + a_1 P_1 + a_2 P_2 + \dots + a_n P_n$$

the data being scaled so as to map channels 0-200 on to the real axis between -1 and +1. This has been done in order that the Legendre polynomials, which are orthogonal over the interval  $[-1,+1]$ , are approximately orthogonal over the region which is fitted, and because, assuming the proton peak to be located at about channel 100, the few lowest order Legendre polynomials automatically have the right sort of shape to fit the background.

The/.....

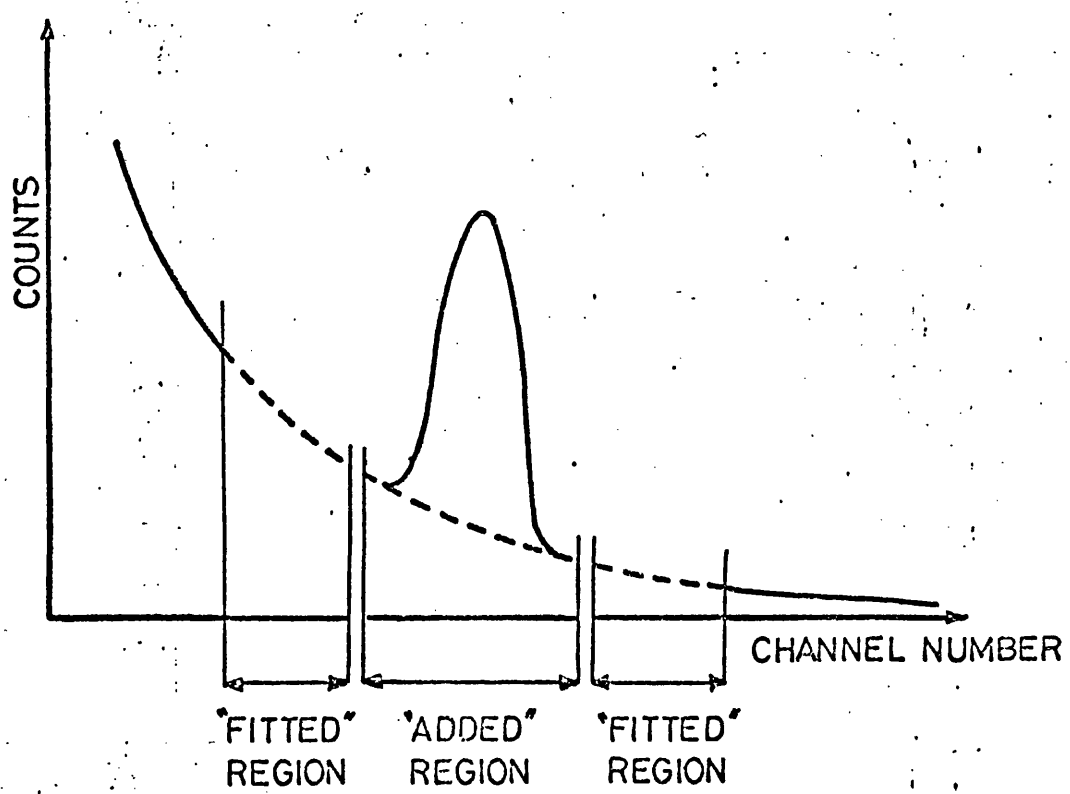
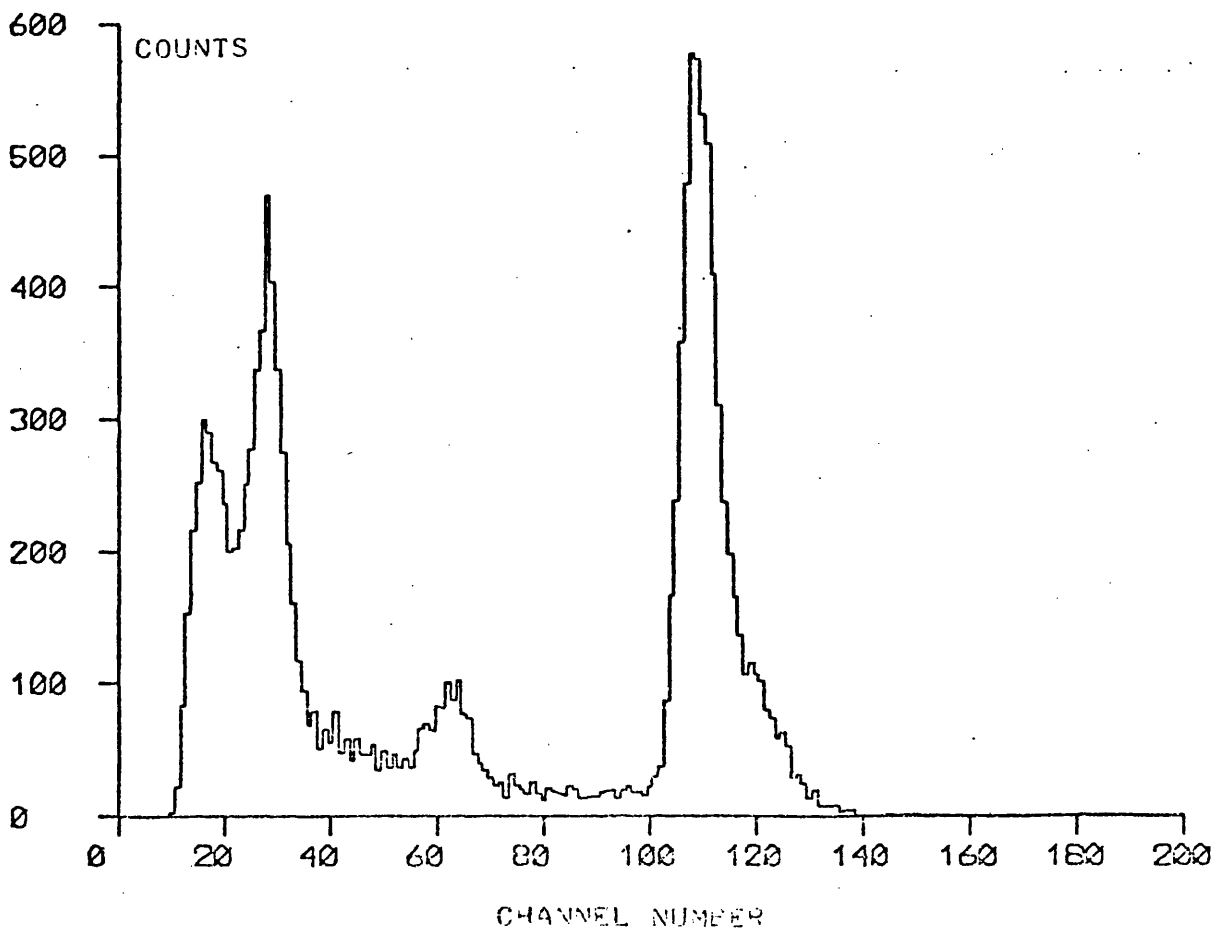


FIG. 3.1 IDEALISED PULSE HEIGHT SPECTRUM

FIG. 3.2 TYPICAL PULSE HEIGHT SPECTRUM



The maximum order of Legendre polynomial in the series,  $n$ , is determined by visual inspection. The "fitted" and "added" regions are chosen using the on-line interactive graphics facilities of the University of Glasgow D.E.C. PDP-10 computer. The raw data, from one counter of the ladder of ten, is displayed on a visual display unit and the channels over which the counts are to be added up and the background fitted are chosen using a cursor mechanism. The data, with the fitted curve, is then redrawn. If the fit is acceptable, i.e. if the  $\chi^2$  of the fit is sensibly near to unity and if by visual inspection the fitted curve seems to make a good interpolation of the background under the peak, then the next counter is considered. If not, then the order of the series is changed, with or without some small changes in the channel numbers until an acceptable fit is obtained.

It is recognised that this procedure of a somewhat subjective nature, but tests have been performed in which different people have fitted the same raw data in order to estimate the probable error. This error has always been less than 2%. A typical counter pulse height spectrum is shown in Fig. 3.2.

The area of the proton peak in a counter pulse height spectrum is the ordinate, at some proton energy, of a proton yield spectrum produced by bremsstrahlung. When using the photon single difference technique, the proton yield spectrum corresponding to the difference of the two bremsstrahlung spectra involved is obtained by subtracting/.....

subtracting the two proton yield spectra produced by the two bremsstrahlung spectra. The subtraction is performed by taking the difference of corresponding counter pulse height spectra and then evaluating the area, in the manner described above, of the proton peak in the resulting counter pulse height difference spectrum. This is better than evaluating the areas of the proton peaks in the two counter pulse height spectra corresponding to the two bremsstrahlung spectra and then subtracting these two areas because in the first method most of the background in the counter pulse height spectra cancels and two different fits to the background are avoided.

The dead-time corrections are applied at this stage in the analysis, each counter's peak area being multiplied by the appropriate correction.

For several reasons the number of counts in the proton peak obtained as described above is not the same as the actual number of protons incident on the counter. These reasons are: firstly, multiple scattering in a counter may cause a proton to leave the counter through the sides before it has deposited enough energy to be included in the proton peak area seen in the pulse height spectrum, secondly, inelastic nuclear interactions in a counter produce a low energy tail whose area is excluded from the area of the proton peak, and thirdly, on the low energy side of the peak the fitted curve is actually/.....

actually fitted to the sum of the background and the low energy tail and not to the background alone. The second and third effects are shown in Fig. A6.1. Corrections for these effects have been calculated and are combined to give the absolute efficiency of the counters as described in Appendix 6.

As can be seen in Fig. 3.2, apart from the proton peak there may be peaks in the counter pulse height spectra corresponding to the presence of other positively charged reaction products. Deuterons and tritons are in evidence in the example shown. These have a half and a third respectively of the energy of a proton of the same magnetic rigidity and are therefore easily distinguished if the protons stop in the counter. Alpha particles of the same magnetic rigidity as protons, on the other hand, have the same energy, but the light output of NE102A<sup>29)</sup> for an alpha particle is less than half that for a proton of the same energy, and so again alpha particles could be distinguished from protons. He<sup>3</sup> particles are not generally seen. A He<sup>3</sup> particle of the same magnetic rigidity as a proton has four-thirds of its energy, and for protons near the endpoint this is not kinematically possible.

### 3.3 Determination of the proton yield spectrum

After the area of the proton peak  $C_J(\bar{p})$  in each counter pulse height spectrum has been found, the experimental proton yield spectrum differential in proton energy and solid angle

$$\frac{d^2N}{dE d\Omega}$$

(number of protons per MeV per steradian) is calculated from

$$C_J(\bar{p}) = \frac{d^2N}{dE d\Omega} \bar{E} \frac{1 + \frac{\bar{E}}{2m}}{1 + \frac{\bar{E}}{m}} \bar{\epsilon} \tau_J(\bar{E}) \eta(\bar{E})$$

as described in Appendix 4. Here

$$\bar{E} \frac{1 + \frac{\bar{E}}{2m}}{1 + \frac{\bar{E}}{m}} \bar{\epsilon}$$

is the product of the energy and solid angle bites,  $\tau_J$  is the relative efficiency of counter J and  $\eta$  is the absolute efficiency of the counter. Usually several different spectrometer magnetic field settings are used at any one photon energy and angle so that the region of interest near the endpoint is covered in detail. For each spectrometer field setting, through the spectrometer energy calibration (Appendix 3) the proton energy corresponding to each counter in the ladder is determined. The result is the experimental differential proton yield spectrum as a function of energy. Four such spectra are shown in Figs. 4.2, 4.3, 4.4, and 4.5.

For the  $O^{16}(\gamma, p)$  experiment, which used bremsstrahlung from a Au radiator ( $.191 \pm .001 \text{ gm/cm}^2$ ) as the source of photons, the electrodisintegration correction was applied at this point in the analysis/.....

analysis. The contribution by virtual photons to the proton yield in this experiment is about one third of the total. This is unlike the case of the carbon and lithium experiments, performed using the Be-Al photon single difference technique, where the contribution by virtual photons to the proton yield is considerably less than 10%. The factor of some 30% for the Au radiator may obviously be made arbitrarily small by increasing the radiator thickness, which would also increase the proton yield and therefore, for the same run-time, improve the statistical accuracy of the experiment. However this produces the disadvantage of increased smearing, due to electron energy losses in the radiator, of the endpoint region, the region of interest in these experiments, which is bound to lead to increased uncertainties when the cross-section is extracted by fitting a calculated shape to the experimental data. Another disadvantage is that the effect of any uncertainty in the energy loss straggling distribution is magnified when the radiator thickness is increased. The thickness of the Au radiator was chosen to be  $\sim .03$  radiation lengths; this is a reasonable compromise.

To evaluate the proton yield spectrum due to real photons alone, the electrodisintegration proton spectrum obtained with no radiator in place was subtracted from the sum of the electrodisintegration and photodisintegration proton spectra obtained with the radiator. The subtraction was performed in the way described above for the photon single difference technique. For each radiator-out run the energy of the incident electrons from the accelerator was reduced/.....

reduced from the radiator -in value to the most probable energy with which an electron emerges from the radiator. This reduction in energy was  $\sim .2$  MeV.

Not every radiator-in run had a radiator-out partner. The idea behind this was to avoid duplicating information and wasting time. For example, at backward angles, where the cross-section can become very small, the radiator-out run was often omitted for this reason. About half of the runs performed using the Au radiator had an electrodisintegration companion.

In order to apply the electrodisintegration correction to those runs which had no comparable electrodisintegration data, the ratio of the proton yield due to real photons alone to that due to real and virtual photons was obtained for the BeO target, by using the areas of the proton peaks in the counter pulse height spectra, as a function of  $E_\gamma/E_{\gamma_0}$ , where  $E_{\gamma_0}$  is the photon endpoint energy and  $E_\gamma$  is calculated on the assumption that all protons are produced by the  $O^{16}(\gamma, p) N^{15}_{g.s.}$  reaction. There was no significant variation of this ratio with either photon endpoint energy or angle. The ratio was almost constant, independent of  $E_\gamma/E_{\gamma_0}$ , but what little variation there was was parameterised by a quadratic function of  $E_\gamma/E_{\gamma_0}$ . (Assuming the ratio to be constant, its value would have been  $.677 \pm .002$ ).

For runs for which there was no electrodisintegration subtrahend, this ratio was used to multiply  $C_J'(\bar{p})$ , the area of the proton peak in the counter pulse height spectrum due to real and virtual photons, to give  $C_J(\bar{p})$ , the area due to real photons alone.

### 3.4 Bremsstrahlung spectra

The bremsstrahlung formula used for the real photon spectra was the extreme-relativistic Bethe-Heitler<sup>30)</sup> formula with the Coulomb correction and intermediate screening. This is basically a Born-approximation formula, and so it is wrong near the endpoint. For the bremsstrahlung cross-section at the endpoint, the calculations of Deck, Mullin, and Hammer<sup>31)</sup> were used. This leaves a gap of  $\sim 1$  MeV between the endpoint and the upper limit of validity of the Bethe-Heitler formula where there is no satisfactory theory. A complete spectrum was constructed by joining the endpoint cross-section to the Bethe-Heitler cross-section with a straight line tangential to the Bethe-Heitler curve at the point of contact<sup>20)</sup>. The effects of electron-electron bremsstrahlung were included. For the virtual photon spectrum, the formula used was that of Barber and Wiedling<sup>32)</sup> and Dalitz and Yennie<sup>33)</sup>. This formula evaluates the electric dipole term only, and only applies to spin zero nuclei. Both these restrictions raise doubts as to the accuracy of the formula.

There are three effects which must be considered when calculating the bremsstrahlung spectra at the photonuclear target, and these are: the finite energy spread of the incident electron beam, the electron energy losses in the radiator, and the straggling in the energy losses. The details are described in Appendices 7 and 8.

The/.....

The test of whether the virtual photon cross-section formula is accurate is to compare cross-sections obtained using real photons only and using virtual photons only. This was done for the  $O^{16}(\gamma, p)$  reaction at 80 MeV at  $30^\circ$ ,  $45^\circ$  and  $60^\circ$ . Proton yields were obtained from the photonuclear target with both the Au radiator in and out. The protons due to real photons alone were unambiguously identified by subtracting radiator-out runs from radiator-in runs. The radiator-out runs give the protons due to virtual photons directly. It was found that the  $(\gamma, p)$  cross-sections evaluated in these two ways were different by  $\sim 20\%$ , those evaluated using virtual photons being the larger. A similar effect has been observed by Ticcioni et al.<sup>35)</sup> in the  $He^3(\gamma, p)$  photodisintegration and electrodisintegration cross-sections. Here the ratio of the electrodisintegration to the photodisintegration cross-sections varies from  $1.06 \pm .02$  at 20 MeV to  $.95 \pm .05$  at 60 MeV. It is likely that the expression for virtual photon production is in error. The restrictions mentioned above point to this, and, furthermore, the real photon extreme-relativistic Bethe-Heitler formula is considered<sup>30)</sup> to be good to  $\pm 2\%$ .

Uncertainties in the virtual photon spectrum are of little significance in the data analysis employed here. For the Be-Al photon/.....

photon single difference technique (Appendix 7) the energies of the incident electrons are chosen to be such that the virtual photons in the difference spectrum largely cancel, the virtual photon peak area being considerably less than 10% of the real photon peak area. Thus uncertainties of 20% in a quantity which contributes less than 10% to a total are unimportant. In the case of the  $O^{16}$  experiment using bremsstrahlung, the correction for virtual photons was obtained from the data themselves thus avoiding the use of a doubtful theoretical form of the virtual photon spectrum.

### 3.5 Calculation of the proton spectrum shape

The proton spectrum shape  $\phi$  to be fitted to the experimental data is calculated from the photon spectrum and involves the following: the angle at which the proton is ejected, the  $Q$  of the  $(\gamma, p)$  reaction to the required state in the residual nucleus, the energy dependence  $s(E_\gamma, E_{\gamma_0})$  of the  $(\gamma, p)$  cross-section, the factor  $\frac{dE_\gamma}{dE_p}$  to transform elementary photon energy intervals to elementary proton energy intervals, the energy loss and straggling of the protons in the photo-nuclear target and the polythene absorber (if used) between the scattering chamber and the spectrometer, and the finite energy bite of the counters. After photoejection of a proton, the residual nucleus may be left in any one of the ground state or the various excited states. Thus the spectrum shape to be fitted to the data is the sum

$$a_0\phi_0(E_p) + a_1\phi_1(E_p) + a_2\phi_2(E_p) + \dots$$

where  $\phi_i(E_p)$  is the spectrum shape, as a function of proton energy  $E_p$ , of ejected protons leaving the residual nucleus in the  $i^{\text{th}}$  state, and the coefficients  $a_i$  are numbers determined by the fitting procedure proportional to the absolute cross-sections to the various states. The details of the calculation are given in Appendices 4 and 9.

The energy dependence of the  $(\gamma, p)$  cross-section  $s(E_\gamma, E_{\gamma_0})$ , which is the ratio of the cross-section at  $E_\gamma$  to that at  $E_{\gamma_0}$  and which is necessary to calculate a proton spectrum from a photon spectrum spanning a finite energy interval, is calculated in a self-consistent manner./.....

manner. The data is first fitted with a spectrum shape assuming a cross-section independent of energy,  $s_0$  say, where  $s_0(E_\gamma, E_{\gamma_0}) = 1$  independent of  $E_\gamma$ . This yields a first approximation  $s_1(E_\gamma, E_{\gamma_0})$ . The data is then fitted again using  $s_1(E_\gamma, E_{\gamma_0})$  as the energy dependence, which yields  $s_2(E_\gamma, E_{\gamma_0})$ . The process is iterated, and it has been found that only two iterations are necessary to ensure convergence to .1%. The energy dependence used was that of the cross-section at  $45^\circ$ , and from the results it may be seen that this is perfectly satisfactory for forward angles. At backward angles the energy dependence might be different, but here the statistics are worse, and so the problem is less relevant.

The protons are produced throughout the photonuclear target material, and hence lose different amounts of energy. For monochromatic photons incident on the target and a  $(\gamma, p)$  reaction between states of zero width, assuming no energy straggling of protons in the target, the emergent proton distribution is rectangular. Including straggling, the distribution is rounded off somewhat. The appropriate energy straggling distribution for the proton energies and target thicknesses used in these experiments is that of Landau<sup>36,37</sup>). However, this distribution has no reasonable analytic form, and to avoid spending a needlessly long time evaluating the double integral involved numerically (Appendix 9) the straggling function was approximated by a reasonably simple triangular function and one of the integrations, that over the target thickness, performed analytically. The remaining integration over energy was performed numerically.

As discussed in section 2.7, at photon energies of about 90 MeV or greater, it is necessary to place an absorber of thickness  $\sim 1 \text{ gm/cm}^2$  between the scattering chamber and the spectrometer. When used, the spectrum of protons leaving the target is shifted down in energy by the energy-dependent energy loss in the absorber. The energy loss straggling distribution for  $1 \text{ gm/cm}^2$  of polythene and  $\sim 75 \text{ MeV}$  protons has the Gaussian form<sup>36)</sup>, and therefore an appropriate Gaussian shape was folded into the spectrum. Since the function describing the energy loss distribution in an absorber,  $s(E_0, x, E)$ , where  $E_0$  is the incident energy,  $x$  is the thickness of the absorber and  $E$  is the final energy, is not simply a function of the two variables  $E_0 - E$  and  $x$ , the spectrum must also be multiplied by the factor

$$\frac{(dE/dx)_{E = E_{\text{incident}}}}{(dE/dx)_{E = E_{\text{final}}}}$$

to transform elementary energy intervals  $dE_{\text{incident}}$  to  $dE_{\text{final}}$ .  
(Appendix 10.)

The finite energy bite of the counters is assumed to be a rectangular distribution whose width can be calculated from the alpha-calibration (Appendix 1) and the geometry of the counter ladder. This distribution is folded into the spectrum in the spectrometer to give the spectrum as seen by the counters.

### 3.6 Determination of the cross-sections

The fitting of the calculated spectrum shape

$$a_0\phi_0(E_p) + a_1\phi_1(E_p) + a_2\phi_2(E_p) + \dots$$

to the experimental spectrum was performed using the method of least-squares<sup>38)</sup>. Typical fits are shown in Figs. 4.2, 4.3, 4.4 and 4.5.

It often happens that the statistical accuracy of the data is not adequate to determine the cross-section to each individual state. In such cases, however, the cross-section to a group of neighbouring states is well determined. However, the errors in the individual cross-sections are correlated, and these correlations must be considered when evaluating the error in the sum of the cross-sections to the group of states.

Implicit in the procedure for fitting the calculated shape to the experimental spectrum is the assumption of an exact knowledge of the energy abscissae of the points forming the experimental spectrum. It is clear that a small shift ( $\approx \frac{1}{2}$  MeV) in the abscissae could have a significant effect on the cross-sections produced from the fit, and such uncertainties could easily be caused by the use of incorrect energy losses in the bremsstrahlung radiators or the windows of the scattering chamber etc. as well as incorrect energy calibration of the magnetic spectrometer or the electron beam energy analysis system. To circumvent this difficulty, the abscissae of the points forming the experimental spectrum are allowed a small measure of freedom characterised/.....

characterised by a parameter  $E_{\text{shift}}$  measuring the difference, at the particular energy concerned, between the nominal energy calibration and the actual calibration desired. The value of the parameter is taken to be that value when the fit of the calculated to the experimental spectrum is best. The same value of  $E_{\text{shift}}$  (to within  $\sim .02$  MeV) is always obtained at the forward angles of a given angular distribution (where the statistics are best) but the value of  $E_{\text{shift}}$  is different for different angular distributions at different photon energies showing that the actual deviation from the nominal energy calibration is energy-dependent. A typical value of  $E_{\text{shift}}$  encountered in the analysis was .4 MeV. This technique allows the experiment to determine its own energy calibration.

The absolute cross-sections are related to the coefficients  $a_i$  of the fit by

$$\frac{ds}{d\Omega} = \frac{A}{\bar{\epsilon} N_A n_e x} a_i$$

as described in Appendix 4, where  $A$  is the atomic weight of the target,  $\bar{\epsilon}$  is the product of the momentum bite of the counters and the solid angle subtended by the spectrometer,  $N_A$  is Avogadro's number,  $n_e$  is the number of electrons delivered to the bremsstrahlung radiator and  $x$  is the target thickness. As discussed in section 2.6, the normal to the target is at  $45^\circ$  to the beam line; consequently the effective thickness is the actual thickness multiplied by  $\sqrt{2}$ . The number of electrons incident on the bremsstrahlung radiator is obtained from the toroid current monitor (section 2.9.) The momentum bite of the counters/.....

counters and the solid angle subtended by the spectrometer are discussed in sections 2.7 and 2.8.

The total cross-sections presented in this thesis were derived from the angular distributions by fitting them with the series

$$\frac{d\sigma}{d\Omega} = \sum_{l=0}^n a_l P_l(\cos\theta)$$

Since  $\int_0^\pi P_l(\cos\theta) 2\pi \sin\theta d\theta$  is only non-zero for  $l = 0$ , the total cross-section is given by  $4\pi a_0$ . Different numbers of terms in the above series were tried in the fitting procedure, the best fit usually being obtained for  $n = 4$  or  $5$ . Fig. 3.3 and Table 3.1 show a typical case.

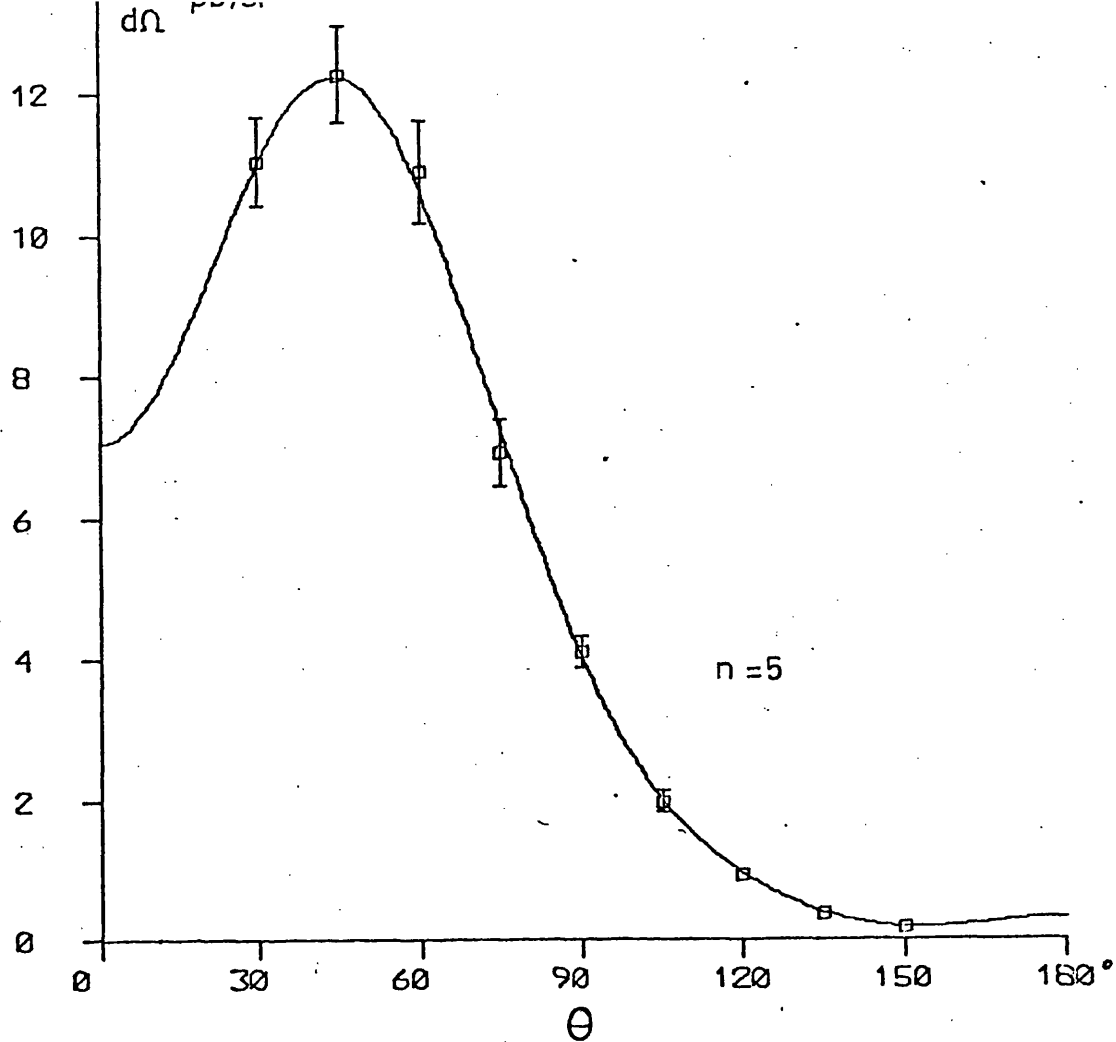


FIG. 3.3  $^{16}\text{O}(\gamma, p)^{15}\text{N}$  g. s.  $E_\gamma = 60$  MeV

Fit  $\sum_{l=0}^n a_l P_l(\cos\theta)$  to experimental angular distribution

n	$\chi^2$	$a_0$
1	50.74	3.466
2	5.42	5.179
3	4.87	5.160
4	1.45	5.243
5	.24	5.242
6	.31	5.217

TABLE 3.1

## CHAPTER 4 EXPERIMENTAL RESULTS

### 4.1 Introduction

This chapter presents the experimental measurements made of the cross-sections of the  $(\gamma, p)$  reaction at photon energies between 40 and 105 MeV in  $\text{Li}^{6,7}$ ,  $\text{C}^{12}$  and  $\text{O}^{16}$ . These are all p-shell nuclei, and the cross-sections presented are for ejection of p-shell protons. A few of the measurements detailed in this thesis are the results of reanalysis of already published data<sup>2)</sup>. These are included because they have been reanalysed in a much more satisfactory way. The present analysis techniques permits extraction of cross-sections to individual states in the residual nucleus from the experimental data; previous analyses<sup>1,2)</sup> made no such pretension. The 60 MeV data for the  $\text{Li}^{6,7}$  and  $\text{C}^{12}$   $(\gamma, p)$  reactions is the result of reanalysis; all other data is new.

As previously stated, two different sources of photons were used in these experiments. For the  $\text{Li}^{6,7}$  and  $\text{C}^{12}$  experiments the photon single difference technique was employed (Appendix 7), whereas bremsstrahlung derived from a Au radiator of thickness  $\sim .03$  radiation lengths was employed for the  $\text{O}^{16}$  experiment. Since the first excited states of  $\text{N}^{15}$ , the residual nucleus in the  $\text{O}^{16}$   $(\gamma, p)$  reaction, are at 5.27 and 5.30 MeV above ground state, and are of opposite parity to the ground state which makes their population less likely, all protons produced within about 5 MeV of the endpoint must be due to the population of the ground state in the residual nucleus. For the  $\text{Li}^{6,7}$  and/.....

and  $C^{12}$  experiments, there are excited states of the residual nuclei relatively near the ground states. To separate these states, the increased resolution of the single difference technique is necessary.

The most significant systematic errors in the cross-sections are those in the photon difference spectrum due to uncertainties in the electron energy losses in traversing the bremsstrahlung radiators and in the absolute efficiency of the counters. Less significant errors are those in the momentum bite of the spectrometer, the Bethe-Heitler bremsstrahlung cross-section, the target thickness, the solid angle of the spectrometer and the number of electrons delivered to the bremsstrahlung radiator.

The area of the peak in the photon difference spectrum is principally determined by the energy losses of the electrons in the radiator,  $\sim 2$  to  $3$  MeV for the Be radiator (See Appendix 7.) The sensitivity of the difference spectrum to the electron energy losses has been investigated by recalculating the bremsstrahlung and virtual photon spectra for different energy losses. It was found that if the energy losses are changed by 10% then the peak area of the photon difference spectrum changes by 22%. The energy losses used (see Appendix 7) have been experimentally verified to  $\sim 4\%$ . The uncertainty in the photon difference peak was estimated to be 11%. This uncertainty is not present in the cross-sections measured using the single Au bremsstrahlung spectrum.

The/.....

The virtual photon spectrum, as calculated in section 3.4, was shown there to be wrong by  $\sim 20\%$ . Whether this 20% error in the spectrum is due to an incorrect shape or magnitude or (most probably) both is not known. But the contribution to the photon difference spectrum by virtual photons is less than 10% and so this uncertainty is not important. Virtual photons are more important in the Au photon spectrum where they form 1/3 of all photons. But here, as described in section 3.4, the virtual photon contributions were removed in a self-consistent manner.

The systematic error in the counter absolute efficiencies was  $\sim 4\%$ , the Bethe-Heitler cross-sections were allowed an uncertainty of  $\sim 3\%$ , and the remaining uncertainties were estimated at  $\sim 4\%$ .

The systematic error in  $\text{Li}^{6,7}$  and  $\text{C}^{12}$  cross-sections is 22%; for the  $\text{O}^{16}$  cross-sections the systematic error is 11%.

To investigate the consistency of the two different methods, and to determine the long-term reproducibility and stability of the experimental system, the cross-section of the  $\text{C}^{12}(\gamma, p)\text{B}^{11}$  reaction as a function of photon energy was again measured using the bremsstrahlung spectrum employed in the  $\text{O}^{16}$  experiment. The populations of the individual states in  $\text{B}^{11}$  could not be determined by this method; instead, the sum of the cross-sections to the ground state and first excited state (2.12 MeV) has been evaluated. This check is relevant for two reasons: firstly, the photon difference spectrum, being the difference/.....

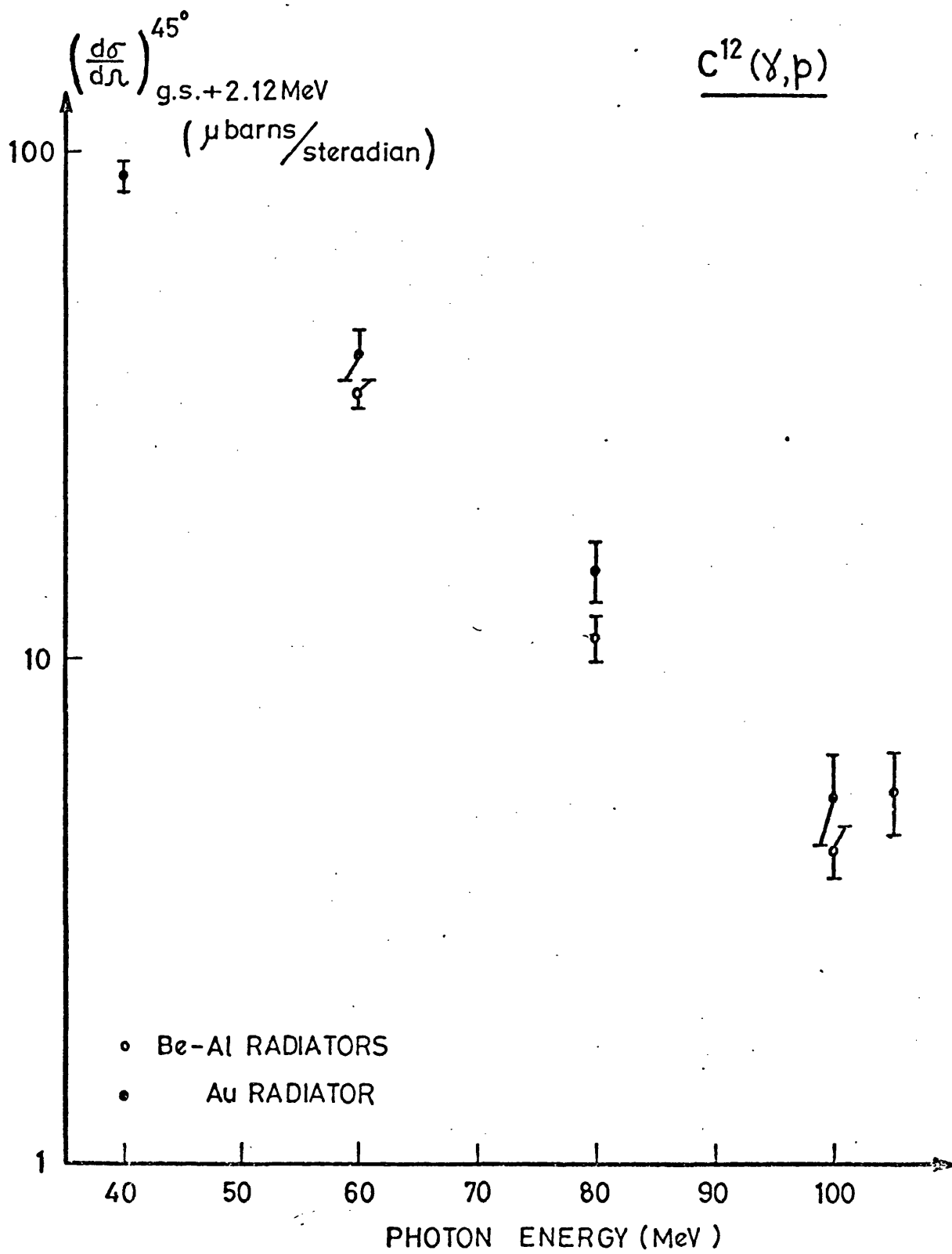


FIG. 4.1

difference of two very similar bremsstrahlung and virtual photon spectra, is very dependant on the accuracy of these two pairs of spectra, and secondly, the  $O^{16}$  and  $Li^7$  and  $C^{12}$  experiments were separated, in time, by one year during which the experimental apparatus was disassembled and subsequently rebuilt.

The sum of the cross-sections of the  $C^{12} (\gamma, p) B_7^{11}$  reaction to the ground state and first excited state of  $B_7^{11}$ , as measured using the two different photon spectra, is shown in Fig. 4.1 as a function of photon energy. It can be seen that the cross-sections measured with the single Au bremsstrahlung spectrum are consistently higher, by  $\sim 25\%$ , than those measured with the photon difference spectrum. The difference is, however, consistent within the errors, and this is taken to be good agreement.

4.2 Li<sup>6</sup>

Fig. 4.2 shows the experimental proton spectrum from the  $\text{Li}^6 (\gamma, p) \text{He}^5$  reaction at a photon energy of 60 MeV and  $45^\circ$ . The spectra at other angles are similar.  $\text{He}^5$  has an excited state ( $\frac{1}{2}^-$ )  $2.6 \pm .4$  MeV above the ground state ( $\frac{3}{2}^-$ )<sup>39</sup> and there is no known further excited state until the 16.70 MeV  $\frac{3}{2}^+$  state. Both the ground state and the 2.6 MeV state are of finite width, the width of the ground state being  $.58 \pm .02$  MeV and the width of the 2.6 MeV state being  $4 \pm 1$  MeV. From the experimental proton spectrum it is obvious that both states are populated. Because of this, the extraction of cross-sections by the fitting procedure described in Chapter 3 was modified. The widths of the states, .58 MeV for the ground state and 4 MeV for the 2.6 MeV state, were folded into the calculated proton spectrum shape before fitting it to the experimental spectrum. Various different shapes were assumed. Gaussians and Lorentzians were tried, but, without truncation, their tails produced protons past the endpoint (negative excitation energy of the nucleus). Rectangles, of widths .58 MeV and 4 MeV, were finally chosen, and the sensitivity of the cross-section to such a choice was determined by repeating the procedure for  $2/3$  and  $4/3$  of the above widths. The error assigned for the uncertainty in the widths of the states is 2%.

Fig. 4.6 shows and Table 4.1 gives the angular distribution of the cross-section of the  $\text{Li}^6 (\gamma, p) \text{He}^5$  reaction at a photon energy of/.....

of 60 MeV leading to population of the ground state and the first excited (2.6 MeV) state in  $\text{He}^5$ . The errors shown are statistical. The ratio of the population of the 2.6 MeV state to that of the ground state is not very well determined, because of the uncertainties in the widths of the states, the uncertainty in the spectrometer energy calibration (section 3.6), the uncertainty in the photon difference spectrum shape and statistical inadequacy, but is between 1 : 1 and 3 : 1.

### 4.3 Li<sup>7</sup>

Fig. 4.3 shows the experimental proton spectrum from the  $\text{Li}^7 (\gamma, p) \text{He}^6$  reaction at a photon energy of 80 MeV at  $45^\circ$ . The spectra at other energies and angles are similar.  $\text{He}^6$  has an excited state (2+) 1.80 MeV above the ground state (0+)<sup>39</sup>). The 1.80 MeV state is .11 MeV wide; this finite width was neglected. From examination of the experimental spectra it is evident that both states are populated.

Figs. 4.7 and 4.8 show and Table 4.2 gives the angular distribution of the cross-section of the  $\text{Li}^7 (\gamma, p) \text{He}^6$  reaction at photon energies of 60 and 80 MeV leading to population of the ground state and the first excited (1.80 MeV) state of  $\text{He}^6$ . The cross-section to the same states for a photon energy of 100 MeV was only measured at  $45^\circ$ . The energy dependence of the cross-section is shown in Fig. 4.15. The errors shown are statistical. The ratio of the population of the 1.80 MeV state to that of the ground state is, as in the case of the  $\text{Li}^6 (\gamma, p)$  reaction above, not very well determined, the uncertainty in the spectrometer energy calibration and photon difference spectrum and lack of statistical accuracy being responsible. For 60 MeV this ratio varies from  $(\frac{1}{2} \pm \frac{1}{2}) : 1$  at forward angles to  $(3 \pm 1) : 1$  at backward angles, whereas at 80 MeV the ratio varies from  $(1\frac{1}{2} \pm \frac{1}{2}) : 1$  at forward angles to  $(4 \pm 2) : 1$  at backward angles.

4.4 C<sup>12</sup>

Figs 1.4 and 4.4 show the experimental proton spectra from the  $C^{12}(\gamma, p)B^{11}$  reaction at a photon energy of 60 MeV at  $45^\circ$  and at  $135^\circ$ .  $B^{11}$  has low-lying negative parity states (like the ground state  $\frac{3}{2}^-$ ) at 2.12 MeV ( $\frac{1}{2}^-$ ), 4.44 MeV ( $\frac{5}{2}^-$ ), 5.02 MeV ( $\frac{3}{2}^-$ ) and 6.74 MeV ( $\frac{7}{2}^-$ )<sup>40</sup>. The next negative parity state is at 8.57 MeV. Usually the experimental proton spectra extend to 7 or 8 MeV excitation energy, so only the four states mentioned above are considered. There is no evidence for population of the positive parity states at 7.30 and 8.00 MeV. This therefore presumably also applies to the positive parity 6.79 MeV state.

There are obviously two distinct clumps of states populated whose behaviour with angle is quite different. The experimental resolution is not sufficient to separate each individual state in the higher excitation energy clump. Only the sum of the cross-section to the 4.44, 5.02 and 6.74 MeV states is determined. However, the statistical accuracy of the data is good enough to permit separation of the ground state and the 2.12 MeV state.

The angular distributions of the  $C^{12}(\gamma, p)B^{11}$  cross-section at photon energies of 60, 80 and 100 MeV are shown in Figs 4.9, 4.10, 4.11 and 4.20, and are given in Table 4.3. The energy dependence of the differential cross-section at  $45^\circ$  is shown in Fig. 4.16, and the energy dependence of the total cross-section is shown in Fig. 4.17. The errors shown are statistical.

4.5  $O^{16}$ 

All the experimental results listed so far (sections 4.2, 4.3 and 4.4) were obtained using the Be-Al photon single-difference technique, but bremsstrahlung from a Au radiator was used for the  $O^{16}$  experiment. The proton energy spectra obtained using bremsstrahlung are not so immediately meaningful as those obtained with the photon difference spectrum .

Fig. 4.5 shows the experimental proton spectra from the  $O^{16}(\gamma, p)N^{15}$  reaction at 60 MeV bremsstrahlung endpoint energy at  $45^\circ$ . It is evident that fitting a calculated shape to the upper 5 MeV (approximately) of the photon spectrum yields an accurate value of the cross-section leading to the (negative parity) ground state of  $N^{15}$ . There is no evidence for the population of the two positive parity states at 5.27 and 5.30 MeV. The next negative parity state is at 6.32 MeV<sup>41)</sup>, but the second rise in the proton spectrum cannot be ascribed purely to the population of this state, since the use of a BeO target means that protons from  $Be^9$  are present in addition to the protons from  $O^{16}$ . Because of the differences in the Q-values and masses of the two nuclei, the top few MeV of protons come solely from  $O^{16}$ . The difference between the energies of threshold protons from  $O^{16}$  and  $Be^9$  is a function of photon energy and angle ranging from 6.00 MeV for  $E_\gamma = 60$  MeV and  $\theta_p = 30^\circ$  to 9.71 MeV for  $E_\gamma = 100$  MeV and  $\theta_p = 120^\circ$ . Unfortunately the relation is such that the difference is/.....

is largest where the statistical accuracy of the proton spectrum is worst. This was found to preclude fitting of the 6.32 MeV state (and any higher negative parity state) since some 2 to 3 MeV of proton spectrum of good statistical accuracy is necessary to obtain a meaningful fit.

Figs. 4.12, 4.13, 4.14 and 4.21 show and Table 4.4 gives the angular distributions of the  $O^{16}(\gamma, p)N^{15}$  reaction leading to the ground state of  $N^{15}$  at photon energies of 60, 80 and 100 MeV. Fig. 4.18 shows the energy dependence of the same cross-section at  $45^\circ$  between photon energies of 40 and 105 MeV, and Fig. 4.19 shows the energy dependence of the total cross-section. The errors shown are statistical.

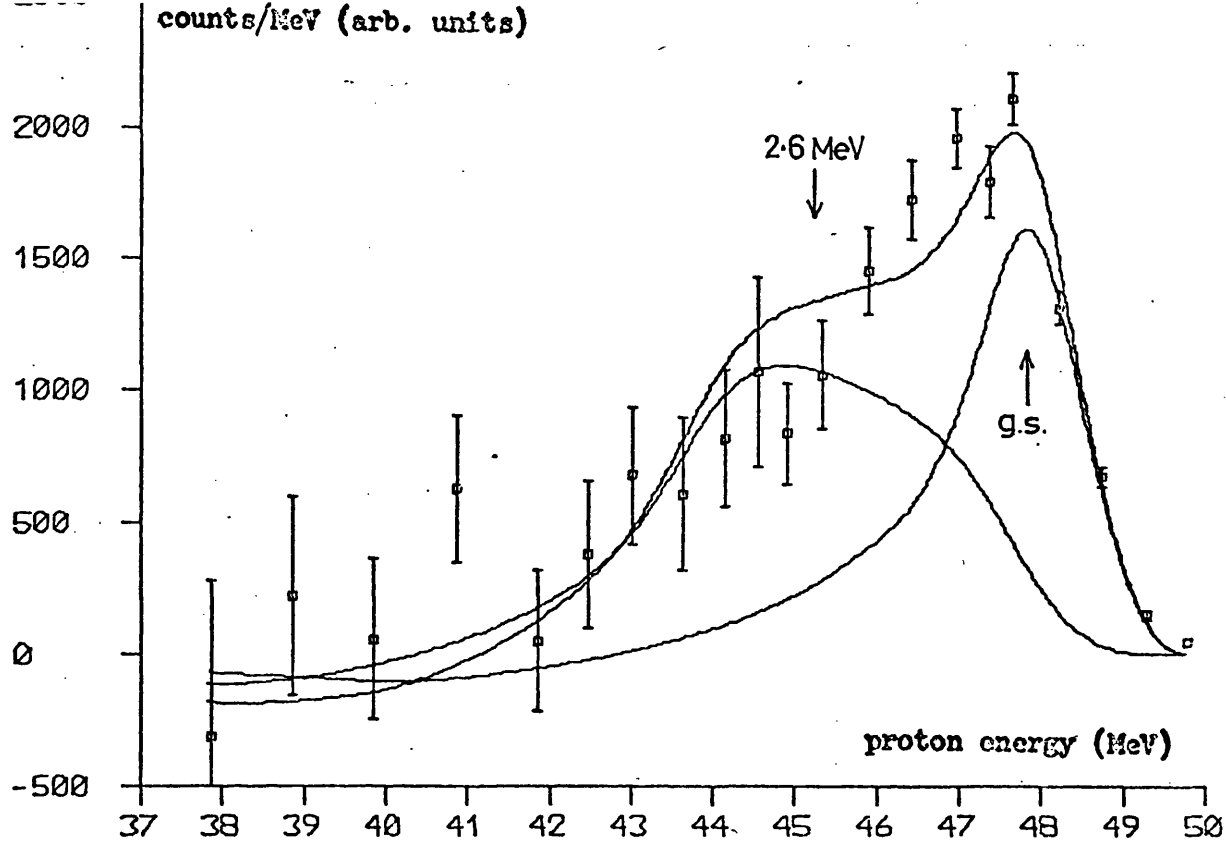
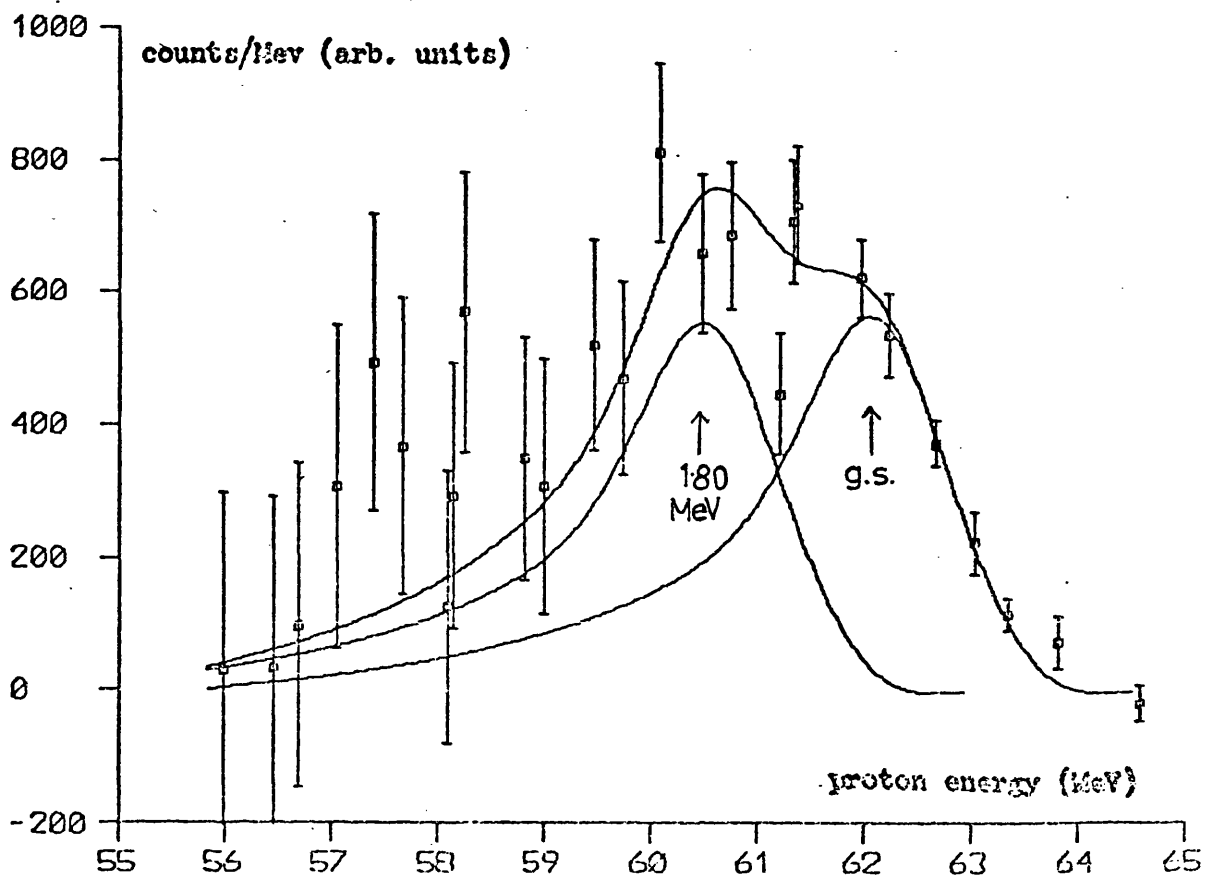


FIG 4.2  $\text{Li}^6(\gamma, p)\text{He}^5$   $E_\gamma = 60 \text{ MeV}$   $45^\circ$  proton spectrum

FIG 4.3  $\text{Li}^7(\gamma, p)\text{He}^6$   $E_\gamma = 80 \text{ MeV}$   $45^\circ$  proton spectrum



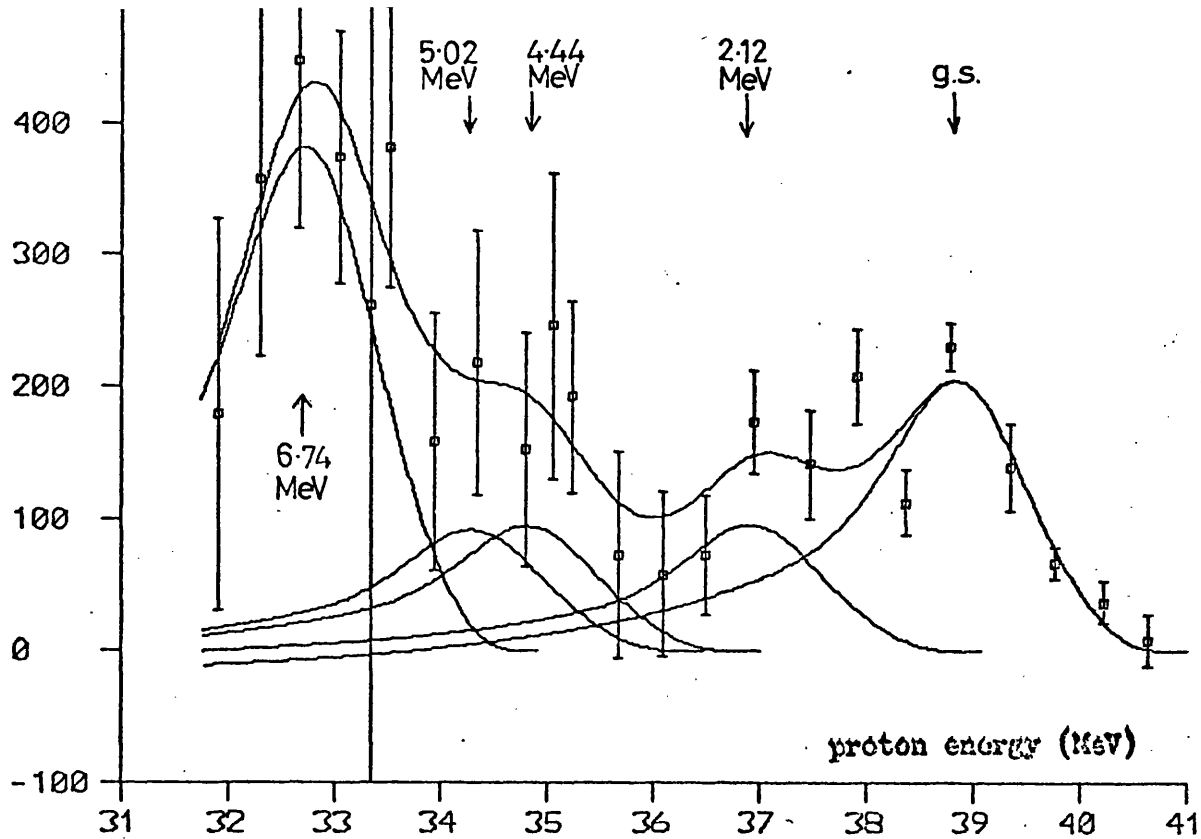
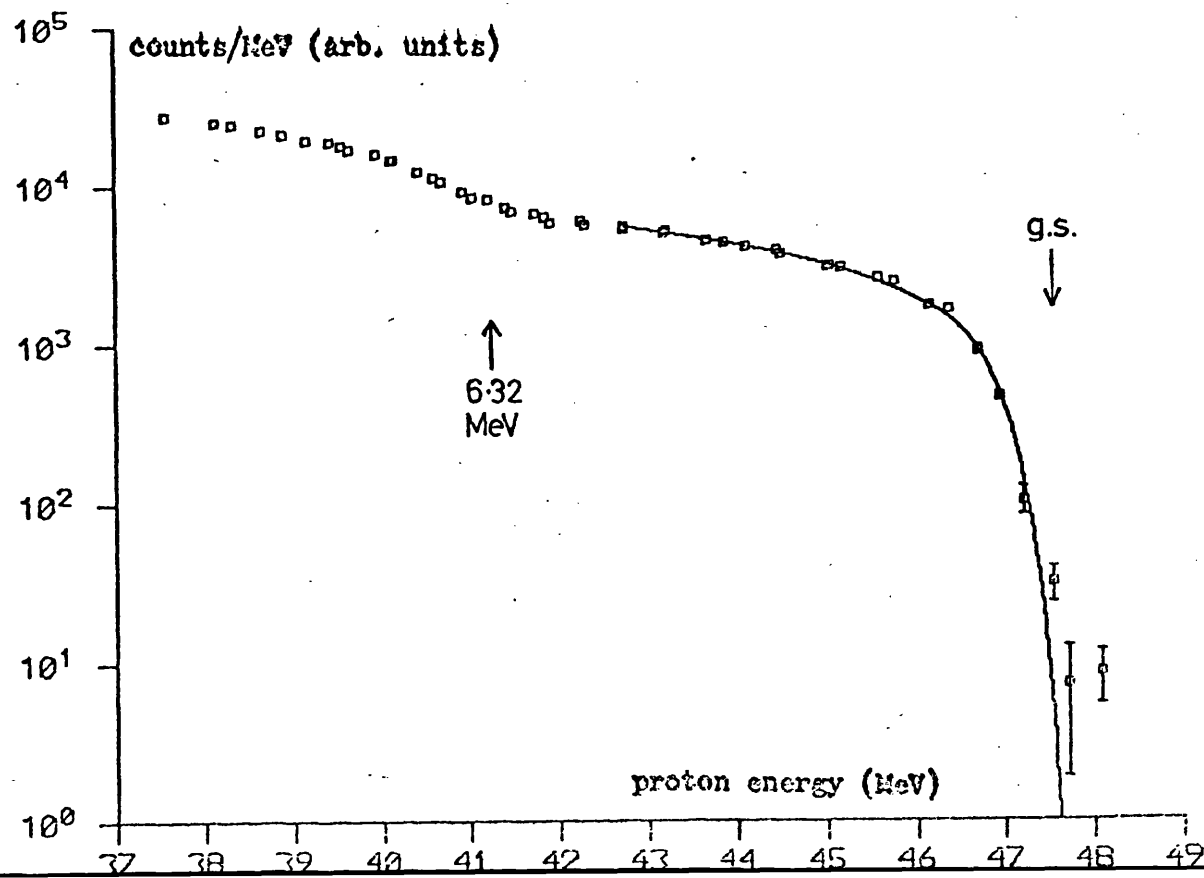


FIG 4.4  $^{12}\text{C}(\gamma, p)^{11}\text{B}$   $E_\gamma = 60 \text{ MeV}$   $135^\circ$  proton spectrum

FIG 4.5  $^{16}\text{O}(\gamma, p)^{15}\text{O}$   $E_\gamma = 60 \text{ MeV}$   $45^\circ$  proton spectrum



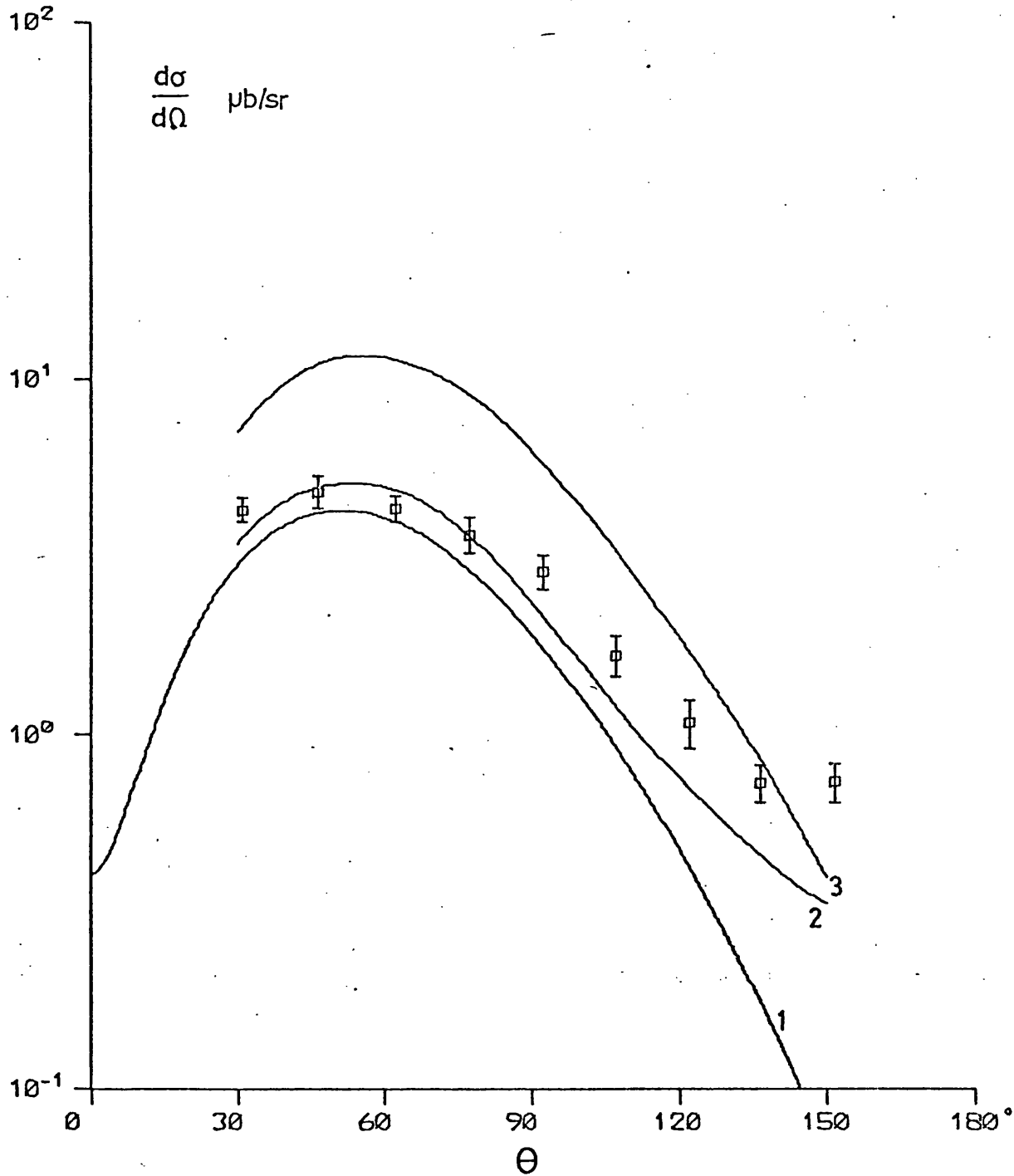


FIG. 4.6  $\text{Li}^6(\gamma, p)\text{He}^5$   $E_\gamma = 60 \text{ MeV}$

□ present experiment: g. s.+ 2.6 MeV s.

1) present calculation

2) Radhakant: surface absorption

3) Radhakant: volume absorption

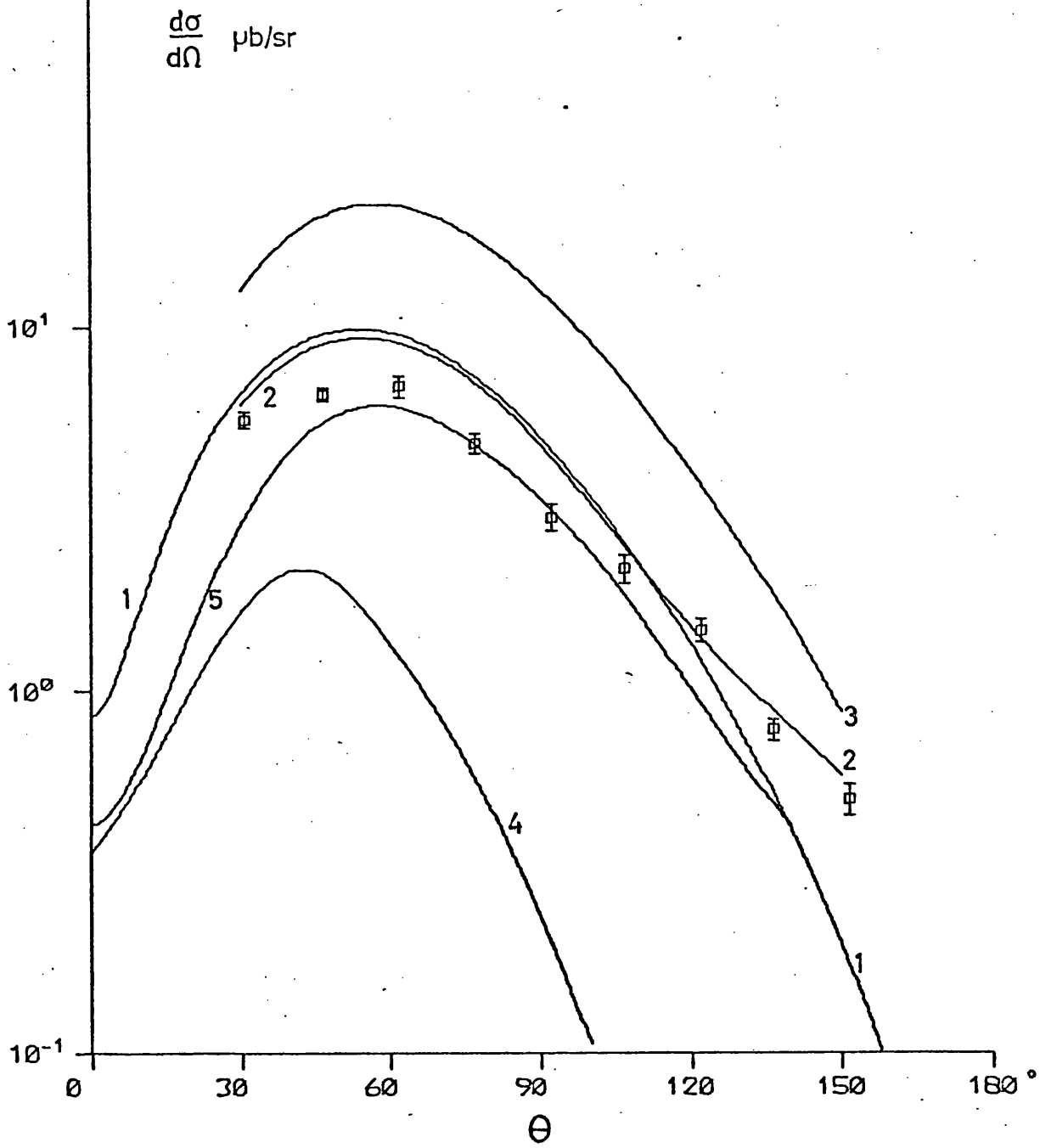


FIG. 4.7  $\text{Li}^7(\gamma, p)\text{He}^6$   $E_\gamma = 60 \text{ MeV}$

- present experiment: g.s.+1.80 MeV s.
- 1) present calculation
- 2) Radhakant: surface absorption
- 3) Radhakant: volume absorption
- 4) Weise: s.m.
- 5) Weise:  $\bar{q}_c = 300 \text{ MeV}/c$   $\Delta q_c = 100 \text{ MeV}/c$

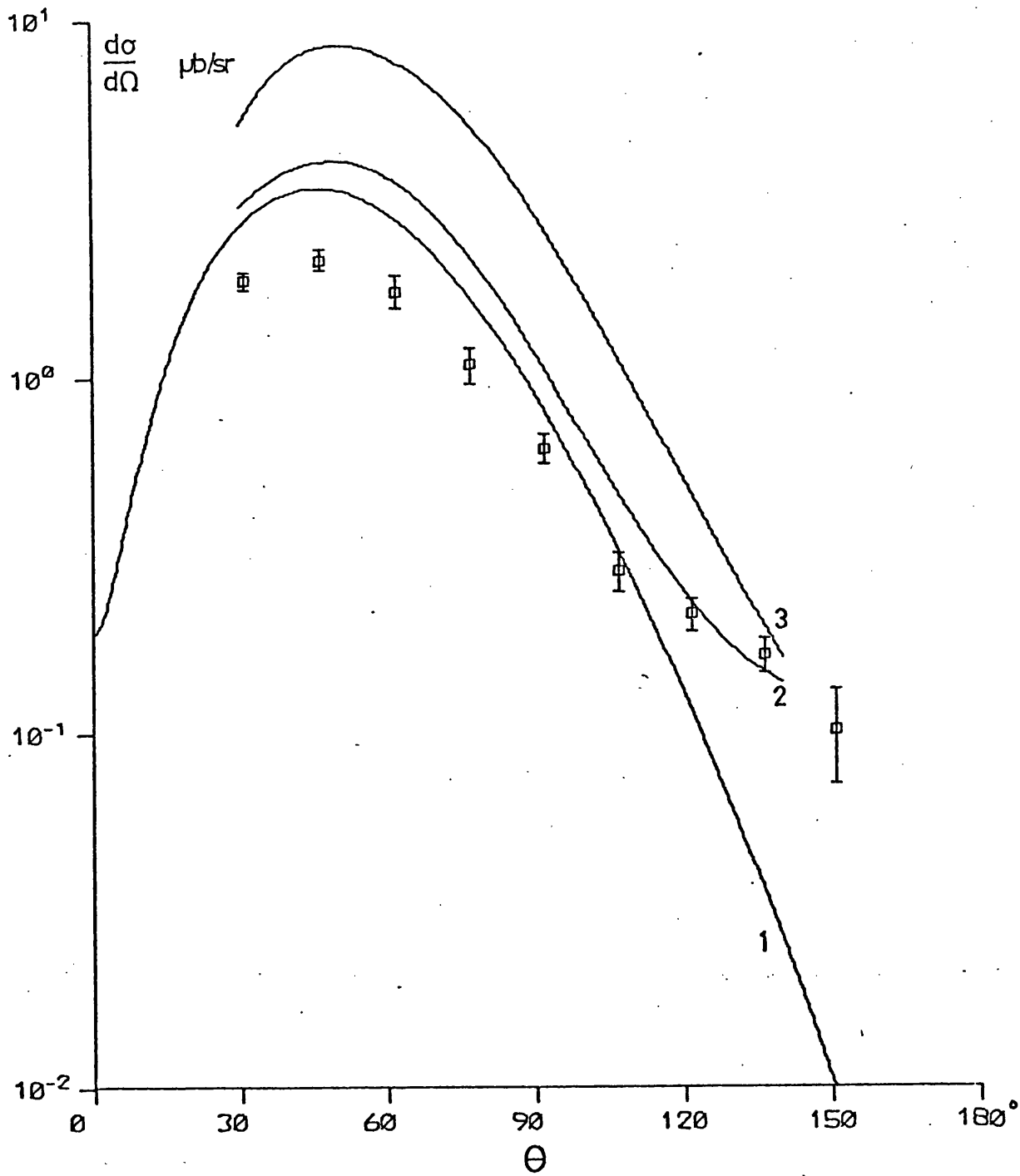


FIG. 4.8  $\text{Li}^7(\gamma, p)\text{He}^6$   $E_\gamma = 80 \text{ MeV}$

□ present experiment: g. s. + 1.80 MeV s.

1) present calculation

2) Radhakant: surface absorption

3) Radhakant: volume absorption

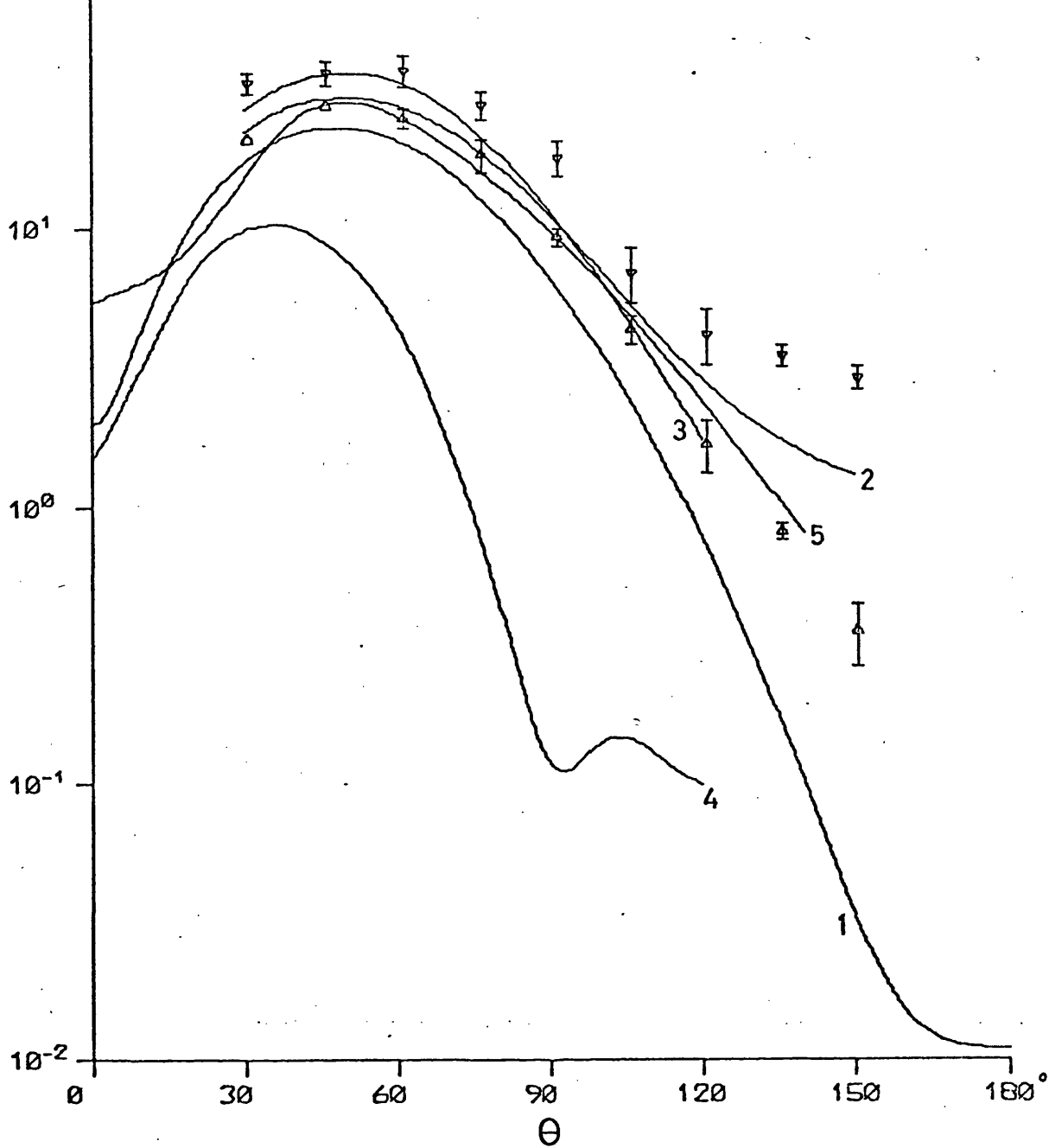


FIG. 4.9  $C^{12}(\gamma, p)B^{11}$   $E_\gamma = 60$  MeV

$\Delta$  present experiment: g. s.

$\nabla$  present experiment: g. s. + 2.12 + 4.44 + 5.02 + 6.74 MeV s.

1) present calculation

2) Radhakant: surface absorption

3) Radhakant: volume absorption

4) Weise: s.m.

5) Weise:  $\bar{q}_c = 300$  MeV/c  $\Delta q_c = 100$  MeV/c

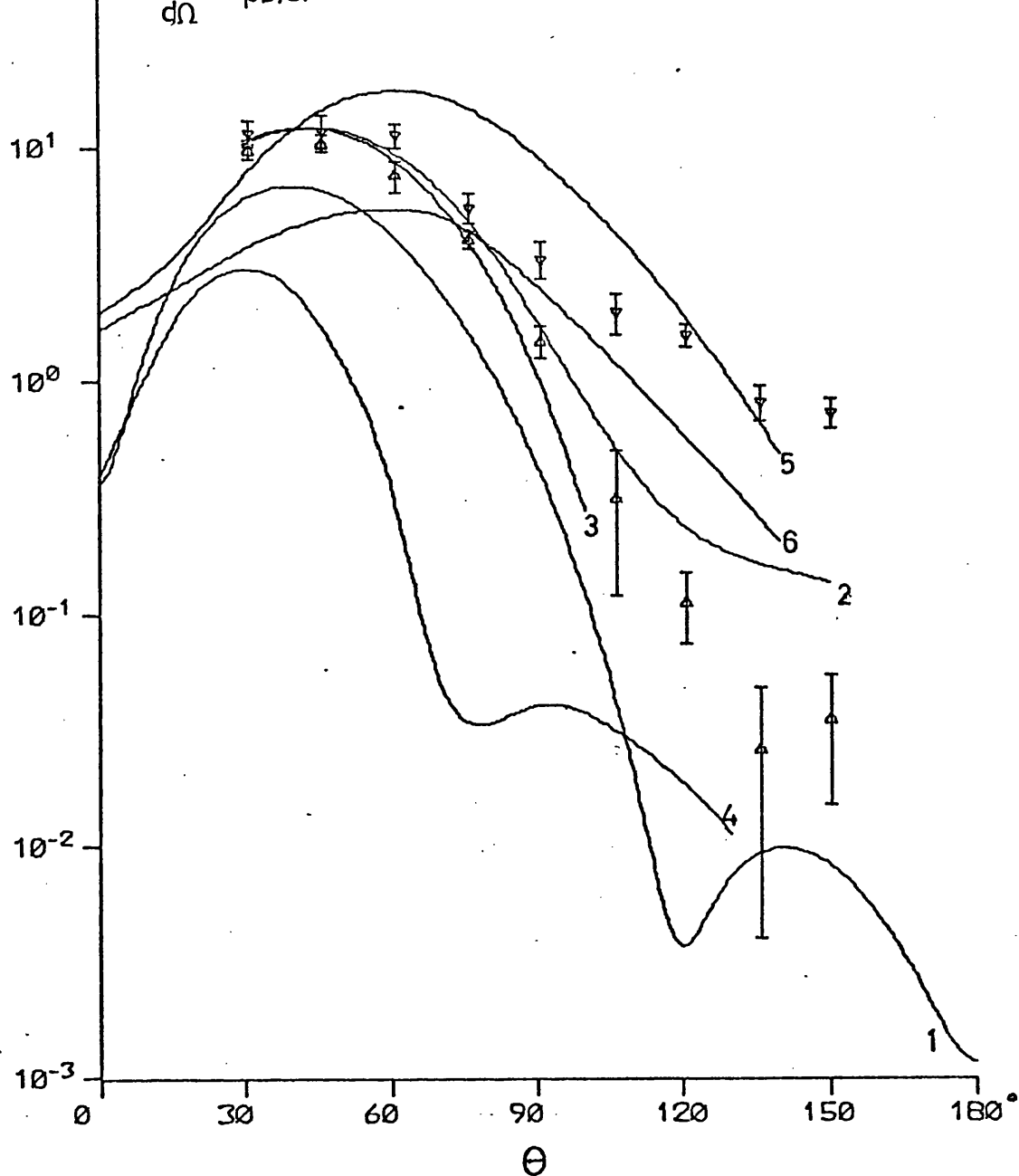


FIG. 4.10  $Cl_2(\gamma, p)B^{11}$   $E_\gamma = 80$  MeV

- △ present experiment: g. s.
- ▽ present experiment: g. s. + 2.12 + 4.44 + 5.02 + 6.74 MeV s.
- 1) present calculation
- 2) Radhakant: surface absorption
- 3) Radhakant: volume absorption
- 4) Weise: s.m.
- 5) Weise:  $\bar{q}_c = 300$  MeV/c  $\Delta q_c = 100$  MeV/c
- 6) Weise:  $\bar{q}_c = 350$  MeV/c  $\Delta q_c = 100$  MeV/c

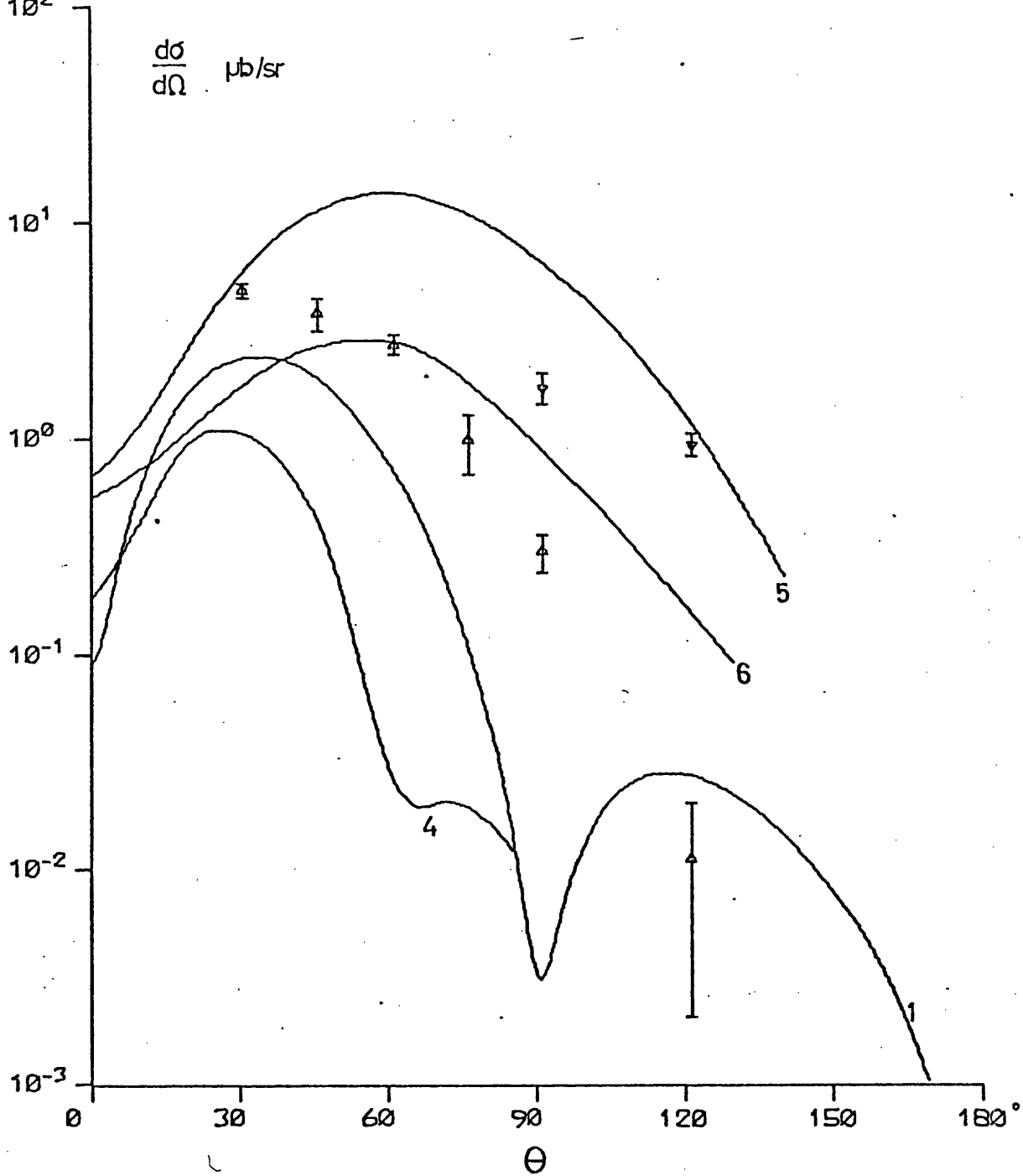


FIG. 4.11  $C^{12}(\gamma, p)B^{11}$   $E_{\gamma} = 100$  MeV

- Δ present experiment: g. s.
- ▽ present experiment: g. s. + 2.12 + 4.44 + 5.02 + 6.74 MeV s.
- 1) present calculation
- 4) Weise: s.m.
- 5) Weise:  $\bar{q}_c = 300$  MeV/c  $\Delta q_c = 100$  MeV/c
- 6) Weise:  $\bar{q}_c = 350$  MeV/c  $\Delta q_c = 100$  MeV/c

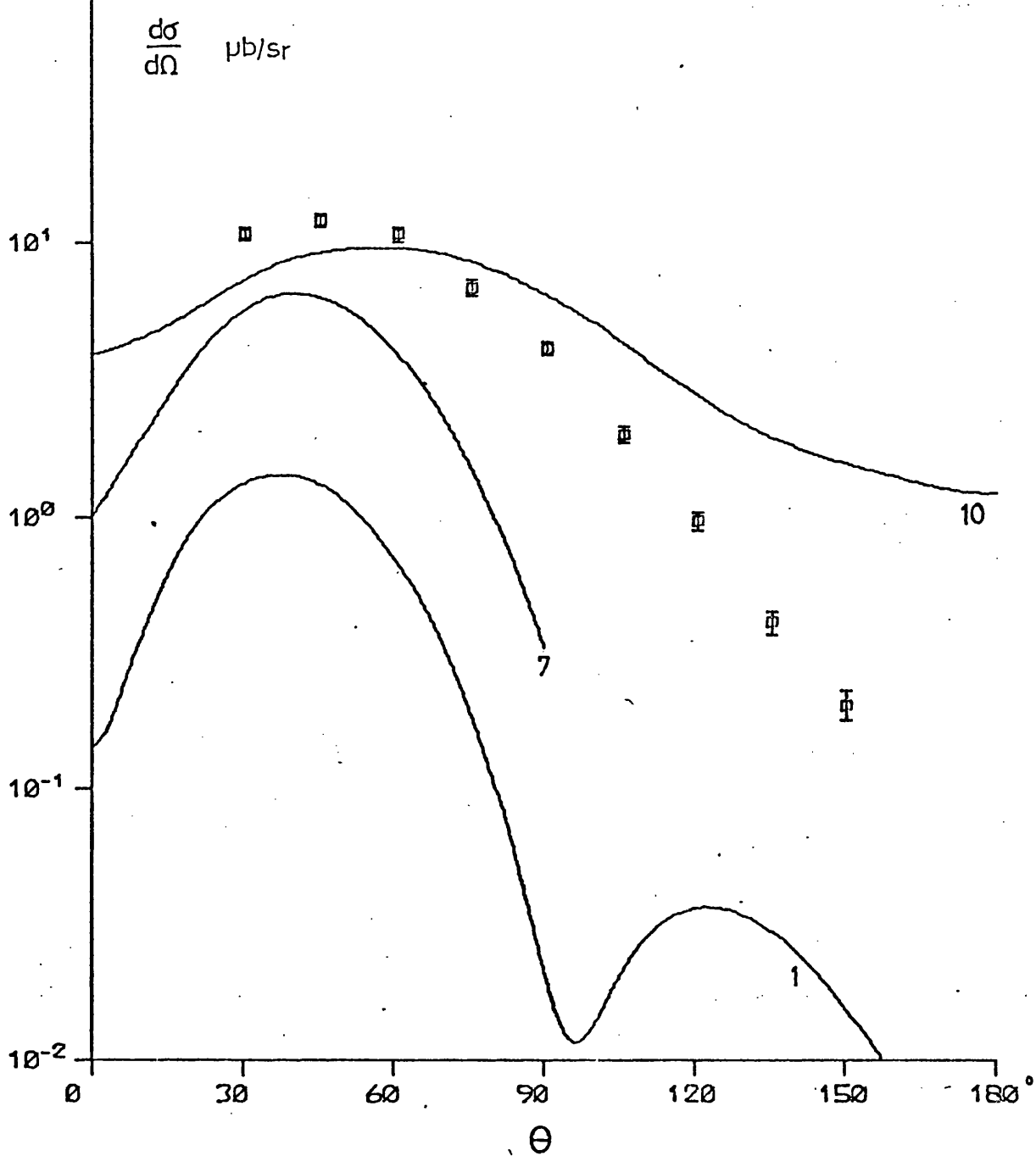


FIG. 4.12  $^{16}\text{O}(\gamma, p)^{15}\text{N}$   $E_\gamma = 60$  MeV

- present experiment: g. s.
- 1) present calculation
- 7) Fink et al: non-orthog.
- 10) Hebach:  $\pi$ -exch.

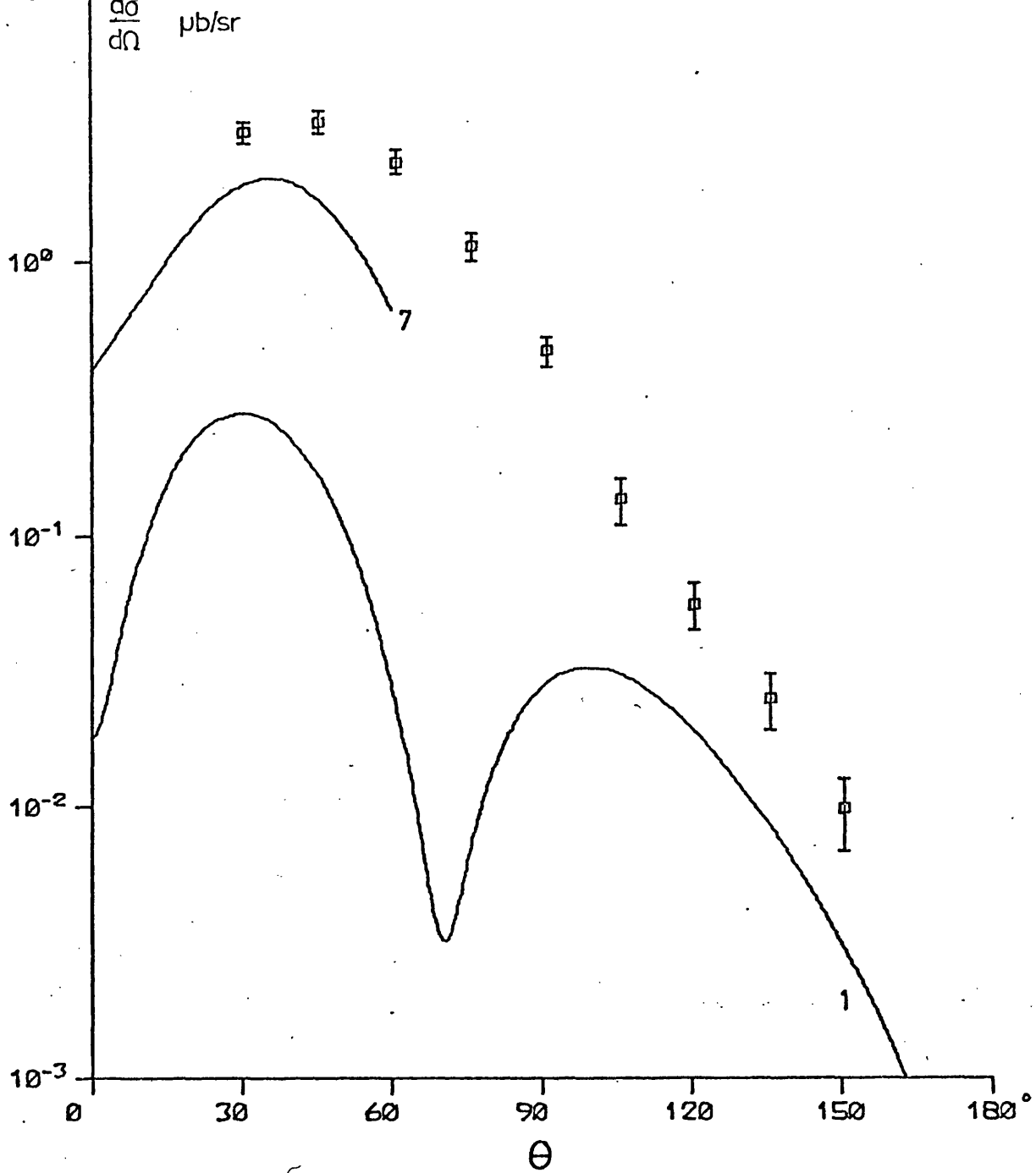


FIG. 4.13  $^{16}\text{O}(\gamma, p)^{15}\text{N}$   $E_\gamma = 80 \text{ MeV}$

□ present experiment: g. s.

1) present calculation

7) Fink et al: non-orthog.

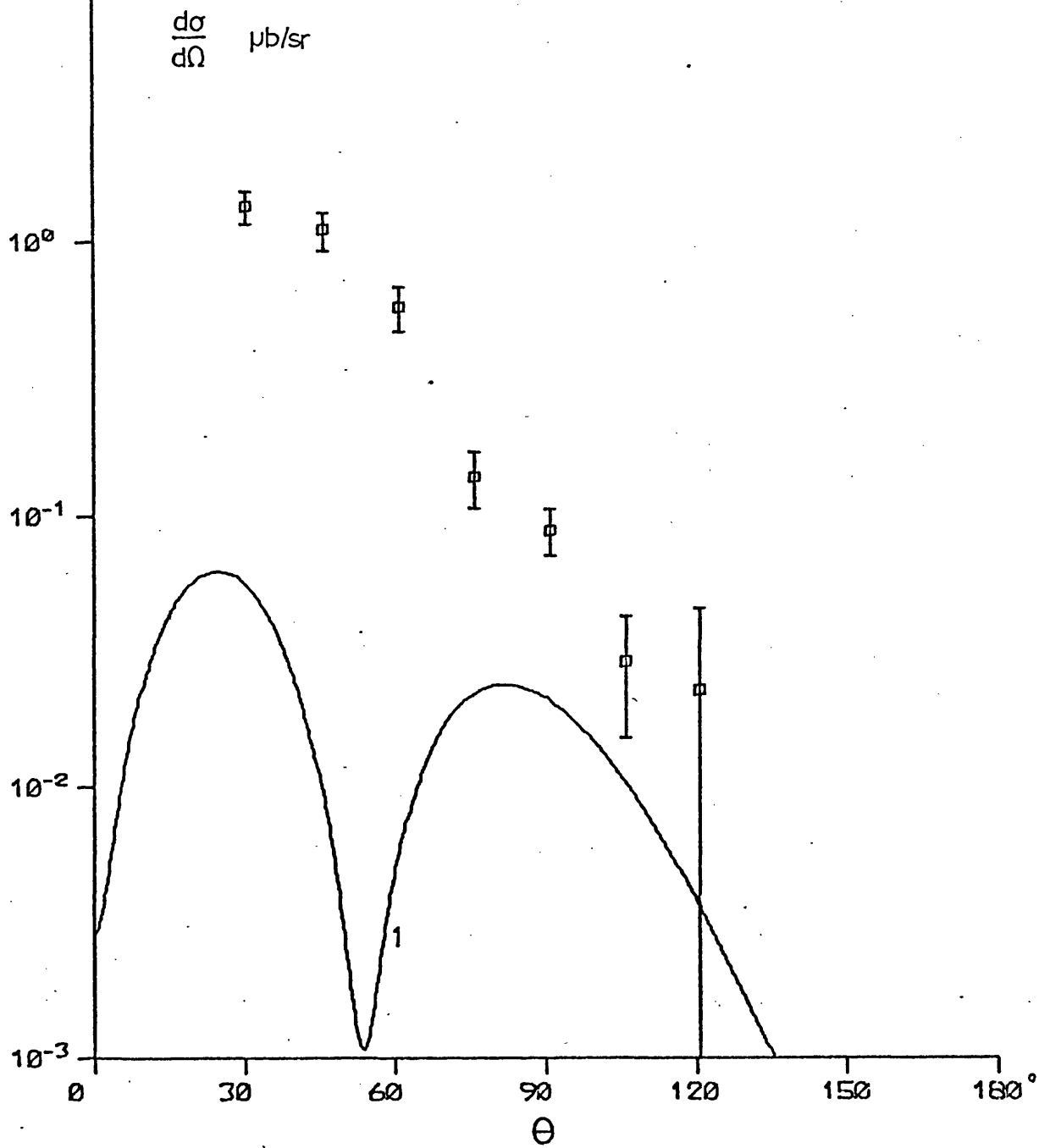


FIG. 4.14  $^{16}\text{O}(\gamma, p)^{15}\text{N}$   $E_\gamma = 100 \text{ MeV}$

present experiment: g.s.

1) present calculation

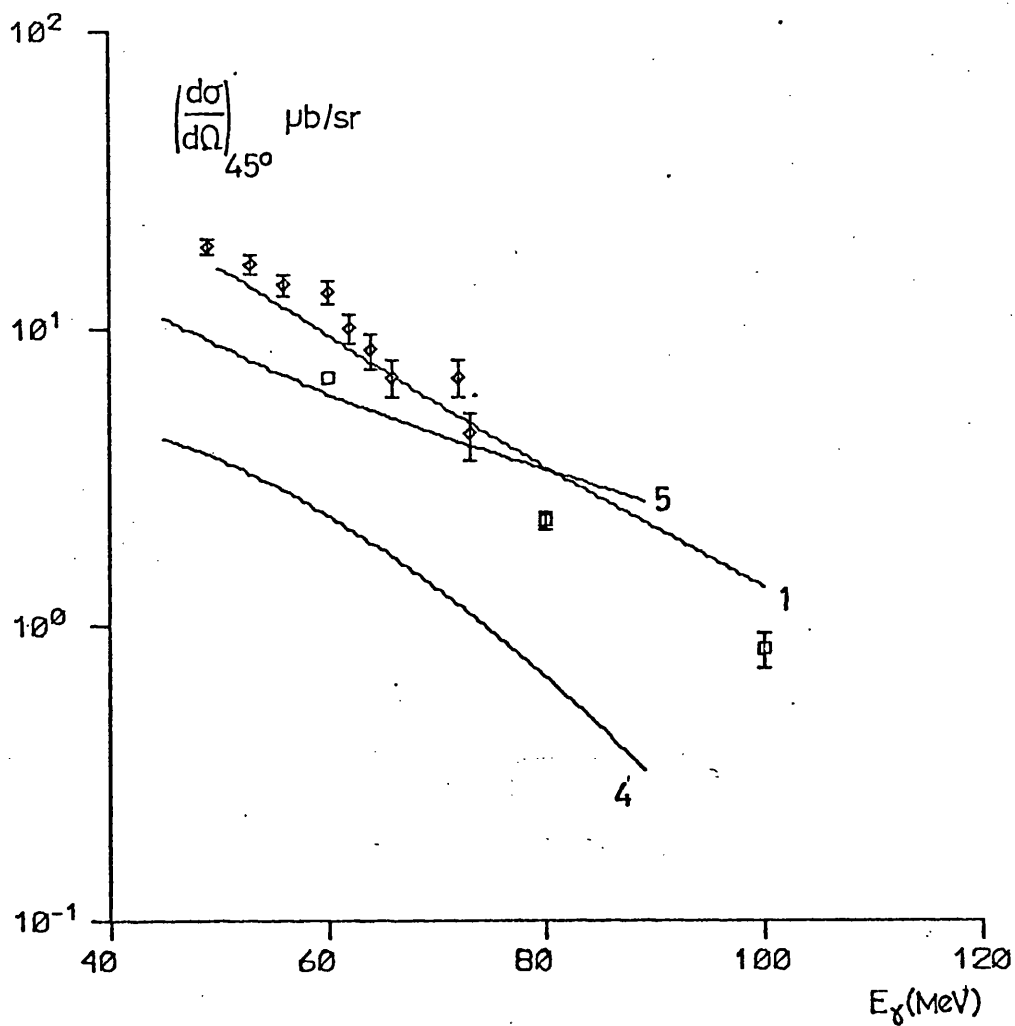


FIG. 4.15  $\text{Li}^7(\gamma, p)\text{He}^6$

□ present experiment: g.s.+1.80 MeV s.

◇ Sanzene et al.

1) present calculation

4) Weise: s.m.

5) Weise:  $\bar{q}_c = 300 \text{ MeV}/c$   $\Delta q_c = 100 \text{ MeV}/c$

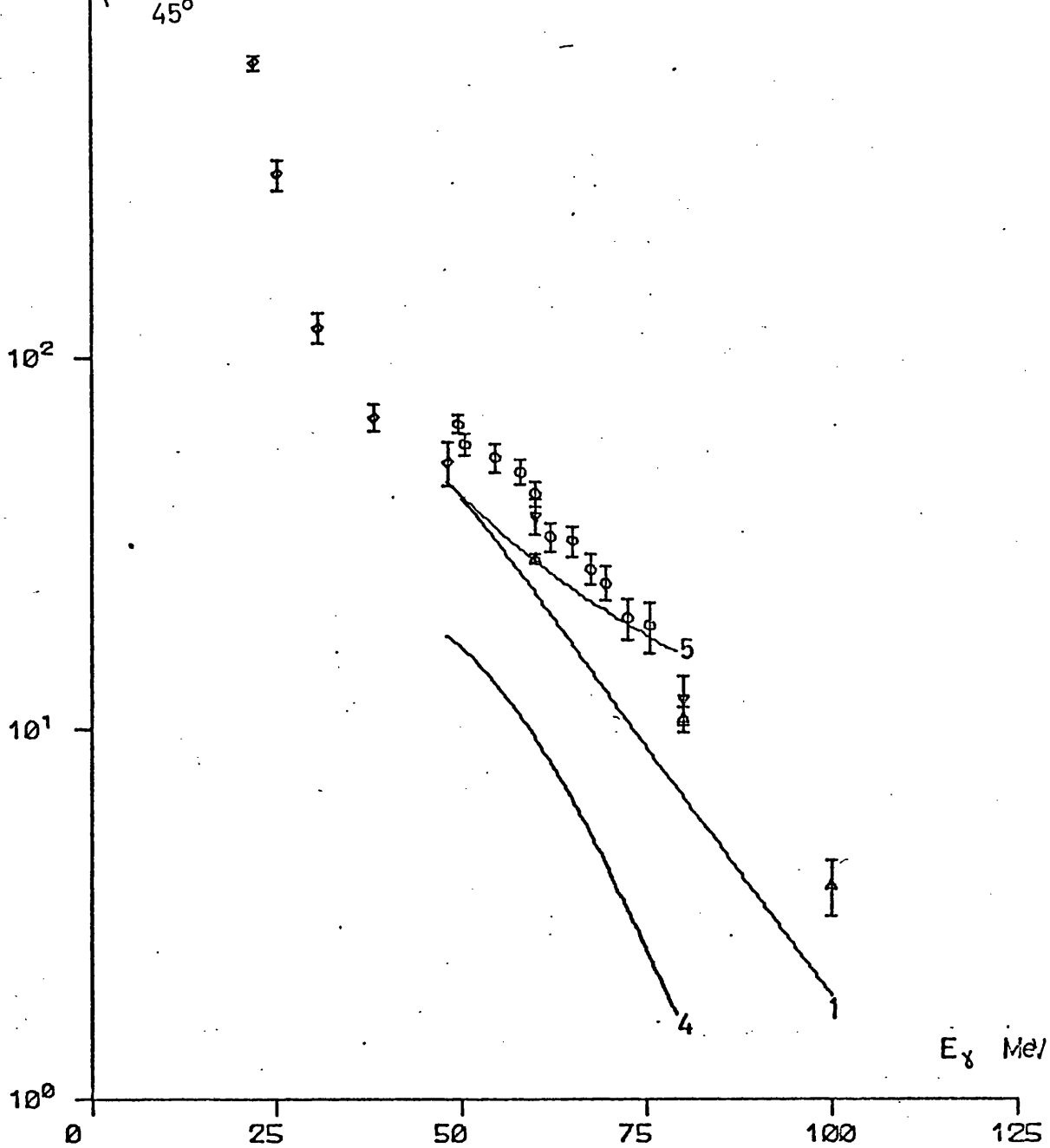


FIG. 4.16  $C^{12}(\gamma, p)B^{11}$

△ present experiment: g.s.

▽ present experiment: g.s.+2.12+4.44+5.02+6.74 MeV s.

◇ Penner and Leiss

○ Manuzic et al.

1) present calculation

4) Weise: s.m.

5) Weise:  $\bar{q}_c = 300$  MeV/c  $\Delta q_c = 100$  MeV/c

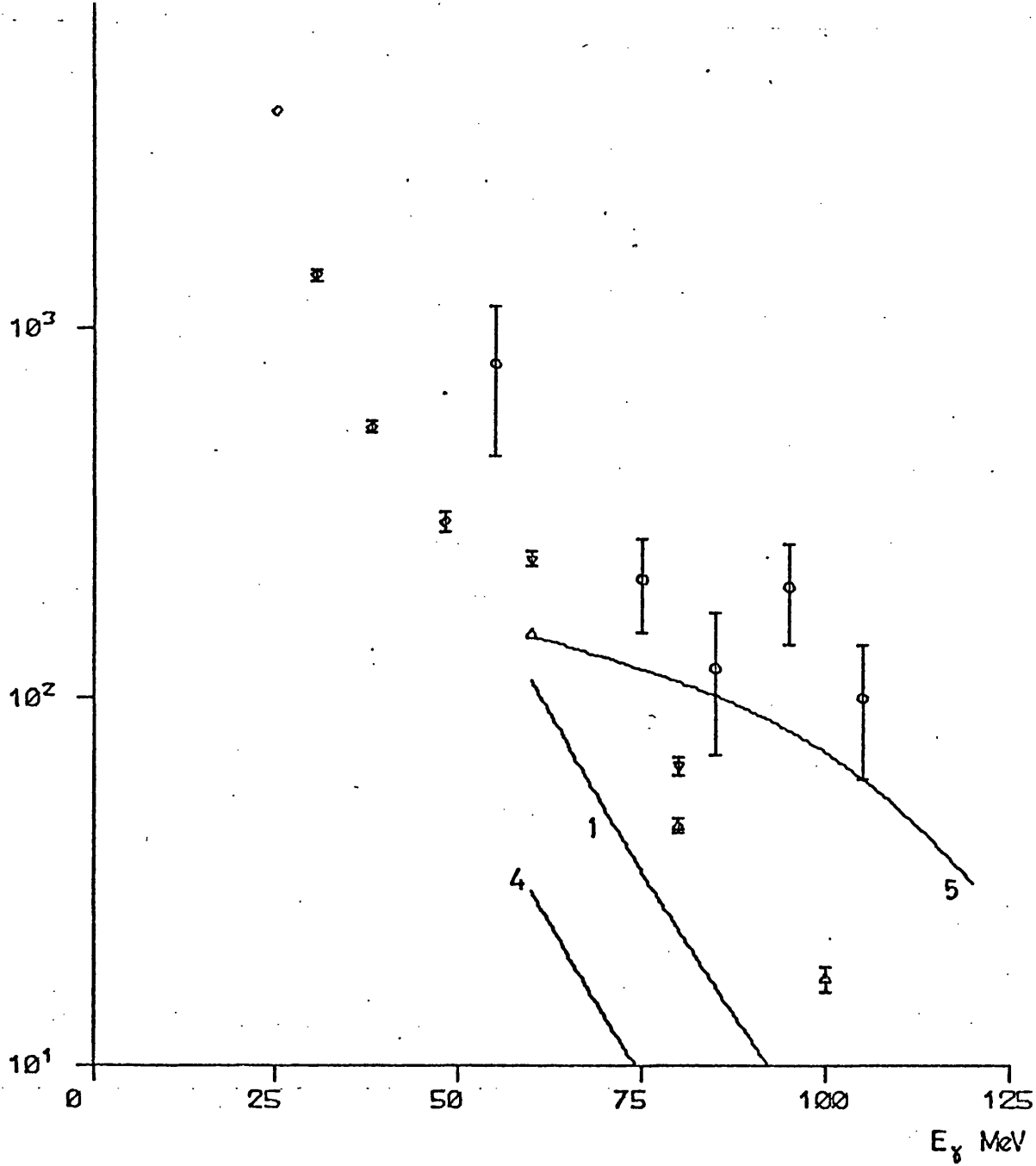


FIG. 4.17  $C^{12}(\alpha, p)B^{11}$

- $\Delta$  present experiment: g. s.
- $\nabla$  present experiment: g. s.+2.12+4.44+5.02+6.74 MeV s.
- $\diamond$  Penner and Leiss
- $\circ$  Taran and Gorbunov
- 1) present calculation
- 4) Weise: s.m.
- 5) Weise:  $\bar{q}_c = 300 \text{ MeV}/c$   $\Delta q_c = 100 \text{ MeV}/c$

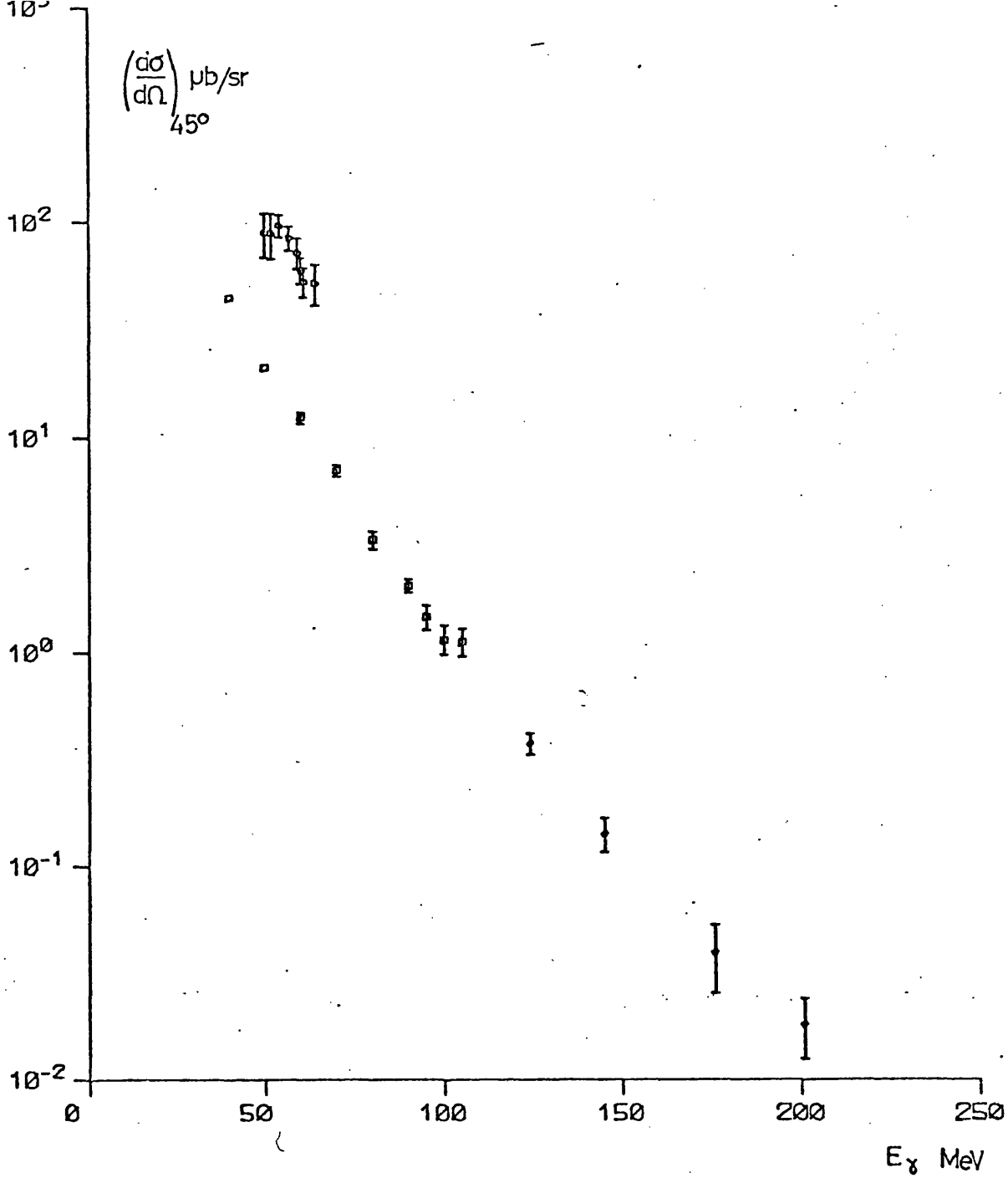


FIG. 4.18  $^{16}\text{O}(\gamma, p)^{15}\text{O}$

□ present experiment: g.s.

◇ H.I.T: g.s.

○ Mancini et al.

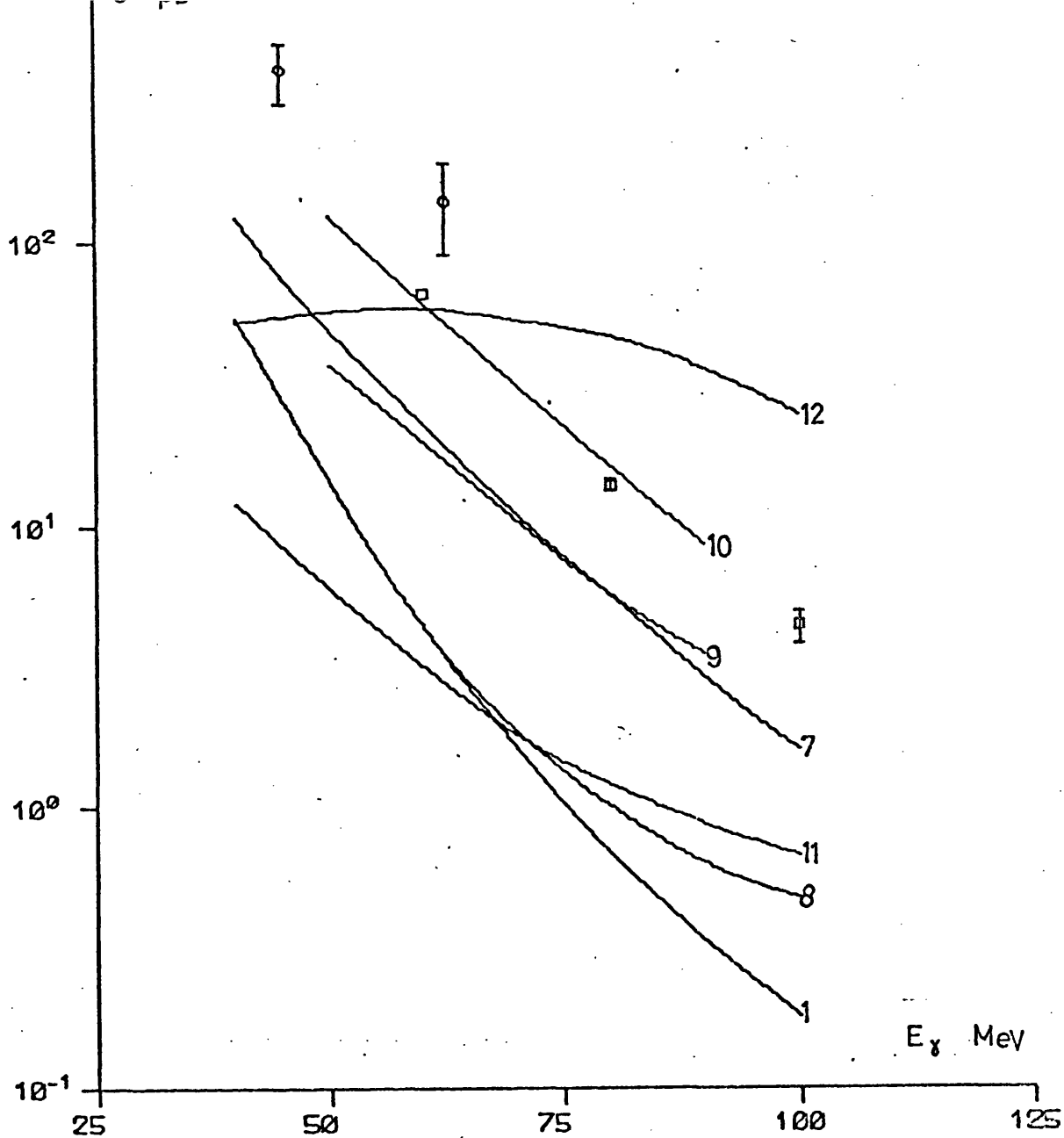


FIG. 4.19  $O^{16}(\gamma, p)N^{15}$

- present experiment: g.s.
- Gorbunov and Osipova
- 1) present calculation
- 7) Fink et al: non-orthog.
- 8) Fink et al: orthog.
- 9) Hebach: s.m.
- 10) Hebach:  $\pi$ -exch.
- 11) Weise: s.m.
- 12) Weise:  $q_c = 300 \text{ MeV}/c$

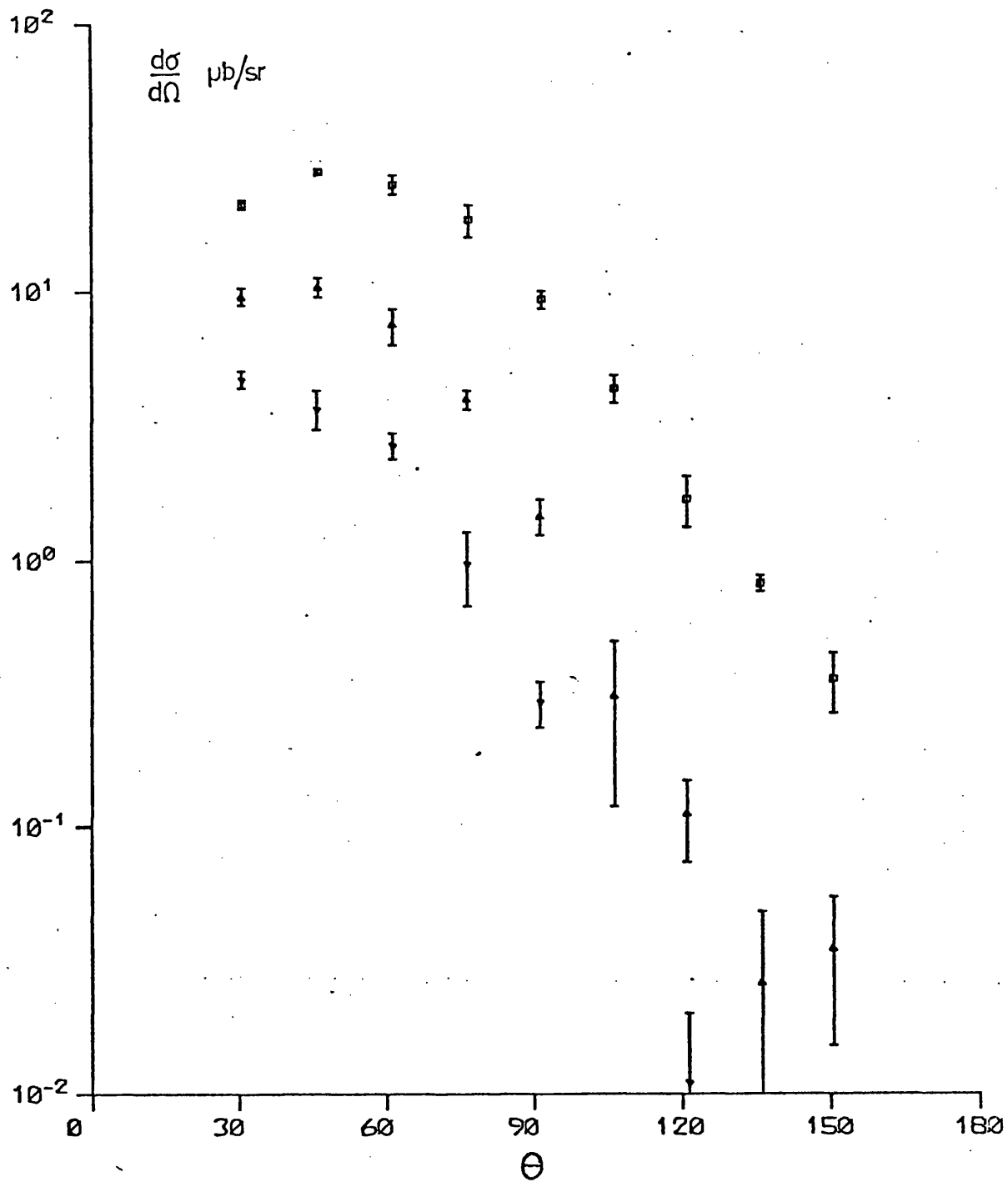


FIG. 4.20  $C^{12}(\gamma, p)B^{11}$  g.s.

- $\square$  present experiment:  $E_\gamma = 60$  MeV
- $\triangle$  present experiment:  $E_\gamma = 80$  MeV
- $\nabla$  present experiment:  $E_\gamma = 100$  MeV

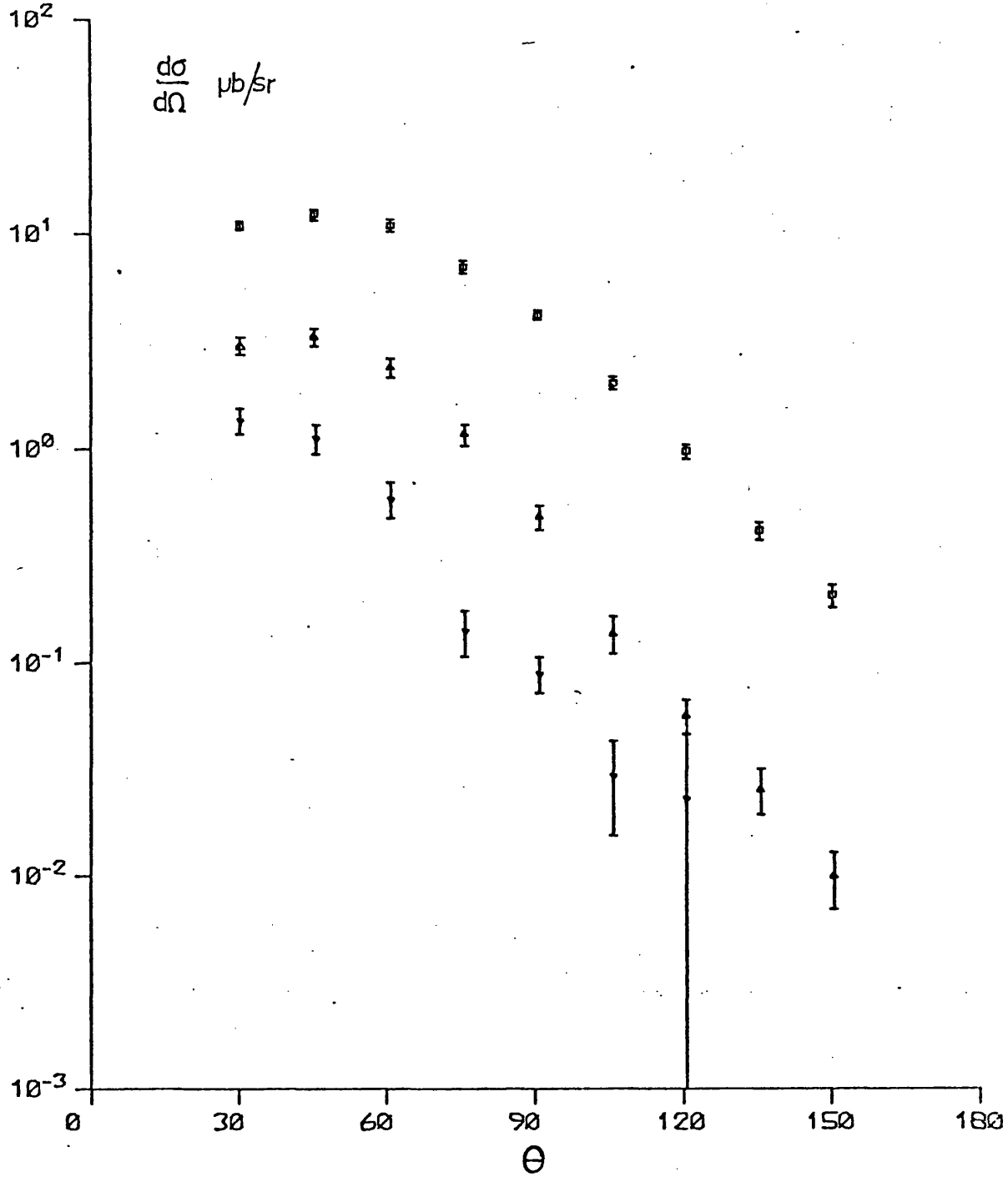


FIG. 4.21  $^{16}\text{O}(\gamma, p)^{15}\text{N}$  g. s.

- present experiment:  $E_\gamma = 60$  MeV
- △ present experiment:  $E_\gamma = 80$  MeV
- ▽ present experiment:  $E_\gamma = 100$  MeV

$\text{Li}^6(\gamma, p)\text{He}^5 \quad \left(\frac{d\sigma}{d\Omega}\right)_{\text{lab.}} \quad (\mu\text{b}/\text{sr}) \text{ to He}^5 \text{ states at } E_x \text{ (MeV)}$

$E_{\gamma, \text{lab.}}$ (MeV)	$\theta_{\text{lab.}}$	$E_x$	
		0.0 + 2.6	
60	30.0	4.55 ± .36	
	45.2	5.05 .52	
	60.4	4.46 .38	
	75.3	3.72 .42	
	90.4	2.88 .32	
	105.1	1.64 .22	
	120.4	1.05 .17	
	135.1	.696 .084	
	150.6	.692 ± .089	
		34.1 ± 1.6	$\sigma_{\text{total}} (\mu\text{b})$

Additional systematic error ± 22% common to all points

TABLE 4.1

$\text{Li}^7(\gamma, p)\text{He}^6 \quad \left(\frac{d\sigma}{d\Omega}\right)_{\text{lab.}} \quad (\mu\text{b}/\text{sr}) \text{ to He}^6 \text{ states at } E_x \text{ (MeV)}$

$E_{\gamma, \text{lab.}}$ (MeV)	$\theta_{\text{lab.}}$	$E_x$	
		0.00 + 1.80	
60	30.0	5.89 ± .31	
	45.2	6.80 .31	
	60.4	7.06 .50	
	75.3	4.86 .32	
	90.4	3.01 .27	
	105.1	2.15 .19	
	120.4	1.43 .11	
	135.1	.750 .050	
	150.6	.477 ± .049	
		43.8 ± 1.2	$\sigma_{\text{total}} (\mu\text{b})$
80	30.2	1.98 ± .12	
	45.1	2.25 .15	
	60.1	1.80 .18	
	74.9	1.10 .13	
	90.0	.632 .059	
	105.1	.282 .036	
	120.0	.210 .023	
	135.1	.159 .018	
	149.9	.096 ± .028	
		11.39 ± .39	$\sigma_{\text{total}} (\mu\text{b})$
100	45.0	.828 ± .113	

Additional systematic error ± 22% common to all points

TABLE 4.2

$C^{12}(\gamma, p)B^{11}$   $\left(\frac{d\sigma}{d\Omega}\right)_{lab.}$  ( $\mu b/sr$ ) to  $B^{11}$  states at  $E_x$  (MeV)

$E_{\gamma lab.}$ (MeV)	$\theta_{lab.}$	$E_x$			$\sigma_{total}$ ( $\mu b$ )
		0.00	0.00 + 2.12	0.00 + 2.12 + 4.44 + 5.02 + 6.74	
60	30.3	21.7 ± 1.0	27.4 ± 1.4	34.6 ± 3.1	
	45.4	28.7 1.0	33.4 1.9	37.5 4.0	
	60.4	25.5 2.1	30.1 2.2	37.8 4.9	
	75.6	18.6 2.6	21.9 1.4	28.2 3.4	
	90.4	9.32 .70	11.65 .95	18.1 2.7	
	105.2	4.31 .52	5.21 .60	6.9 1.6	
	120.3	1.66 .36	2.76 .32	4.13 .92	
	135.1	.798 .058	1.20 .12	3.42 .31	
	150.0	.349 ± .090	.749 ± .092	2.84 ± .27	
		148.9 ± 4.6	182.7 ± 5.8	238.1 ± 11.7	
80	30.2	9.96 ± .82	10.85 ± .93	11.9 ± 1.5	
	45.1	10.70 .88	11.00 1.11	12.1 1.9	
	60.1	7.63 1.17	9.08 .72	11.6 1.4	
	75.1	4.03 .35	4.09 .39	5.53 .81	
	90.0	1.46 .23	1.49 .25	3.30 .59	
	105.2	.31 .19	.30 .12	1.94 .39	
	120.0	.110 ± .037	.302 .066	1.51 .18	
	135.1	≤ .047	.082 .043	.78 .14	
	149.9	.033 ± .016	.060 ± .034	.71 ± .11	
		44.9 ± 2.1	48.4 ± 2.2	65.4 ± 3.9	
100	30.2	4.94 ± .40	5.63 ± .36		
	45.0	3.79 .66	4.14 .50		
	60.1	2.74 .31	2.82 .30		
	75.0	.98 .30	1.22 .24		
	90.0	.293 .057	.277 .094	1.68 ± .28	
	120.1	≤ .020	.069 ± .024	.90 ± .11	
	17.2 ± 1.4	19.6 ± 1.1		$\sigma_{total}$ ( $\mu b$ )	

Additional systematic error ± 22% common to all points

TABLE 4.3

$C^{12}(\gamma, p)B^{11}$   $\left(\frac{d\sigma}{d\Omega}\right)_{lab.}$  ( $\mu b/sr$ ) to  $B^{11}$  states at  $E_x$  (MeV)

$E_{\gamma, lab.}$ (MeV)	$\theta_{lab.}$	$E_x$	
		2.12	4.44 + 5.02 + 6.74
60	30.3	5.4 ± 1.6	6.7 ± 2.7
	45.4	4.9 2.3	4.3 3.5
	60.4	4.8 2.2	7.4 4.4
	75.6	3.3 1.2	6.3 2.9
	90.4	2.37 .94	6.5 2.4
	105.2	.90 .54	1.7 1.5
	120.3	1.13 .40	4.26 .90
	135.1	.397 .050	2.22 .30
	150.0	.413 ± .101	2.09 ± .25
	80	30.2	
45.1			1.1 1.3
60.1			2.5 1.2
75.1			1.46 .67
90.0			1.81 .57
105.2			1.62 .32
120.0			1.21 .16
135.1			.71 .14
149.9			.65 ± .11
100	90.0		1.41 ± .26
	120.1		.83 ± .11

Additional systematic error ± 22% common to all points

TABLE 4.3 (continued)

$^{16}\text{O}(\gamma, p)^{15}\text{N}$   $\left(\frac{d\sigma}{d\Omega}\right)_{\text{lab.}}$  ( $\mu\text{b}/\text{sr}$ ) to  $^{15}\text{N}$  states at  $E_x$  (MeV)

$E_{\gamma, \text{lab.}}$ (MeV)	$\theta_{\text{lab.}}$	$E_x$	
		0.00	
60	30.1	11.04 ± .63	
	45.0	12.30 .69	
	60.1	10.92 .73	
	75.0	6.94 .47	
	90.0	4.12 .23	
	105.2	2.00 .15	
	120.0	.953 .076	
	135.1	.405 .040	
	149.9	.200 ± .025	
		65.8 ± 2.0	$\sigma_{\text{total}}$ ( $\mu\text{b}$ )
80	30.2	3.07 ± .29	
	45.0	3.34 .33	
	60.0	2.38 .25	
	75.0	1.16 .14	
	90.1	.478 .061	
	105.1	.135 .027	
	120.0	.0554 .0106	
	135.1	.0249 .0059	
	150.0	.0096 ± .0029	
		13.95 ± .74	$\sigma_{\text{total}}$ ( $\mu\text{b}$ )
95	45.0	1.45 ± .18	
	75.0	.331 .062	
	105.0	.0401 ± .0096	
100	30.0	1.39 ± .20	
	45.0	1.14 .18	
	60.0	.589 .114	
	75.0	.140 .033	
	90.0	.0883 .0175	
	105.0	.0288 ± .0138	
	120.0	≤ .0451	
		4.43 ± .59	$\sigma_{\text{total}}$ ( $\mu\text{b}$ )
40	45.0	44.1 ± 1.3	
50		21.2 .7	
70		6.97 .45	
90		2.04 .14	
105		1.12 ± .17	

Additional systematic error ± 11% common to all points

TABLE 4.4

CHAPTER 5 DISCUSSION OF RESULTS5.1 Description of results and qualitative deductions from results

On examining the angular distributions of photoprotons presented in Chapter 4, two features become obvious: all angular distributions of protons from all the nuclei considered show strong forward peaking, and the forward peaking becomes more pronounced as the photon energy increases. This forward peaking alone is sufficient to demonstrate that the photon must interact directly with individual nucleons in the nucleus; a compound nuclear process would lead to a much more symmetric distribution.

Another evident feature of the angular distributions is the less rapid variation of cross-section with angle as the excitation energy of the states reached increases. A plausible explanation of this is that an excited state of the residual nucleus is reached because the proton, knocked out of its single-particle orbit by the photon, collides with other nucleons as it travels through and finally leaves the nucleus. The more energy transferred in these collisions, the more the original rapidly varying angular distribution will be smeared out. If this explanation is correct, then only experimental cross-sections to the ground state of the residual nucleus should be compared with predictions which ignore final state inelastic interactions, for example by using an absorptive optical potential to simulate the elastic channel.

The/.....

The differential cross-sections at  $45^\circ$  when plotted on a logarithmic scale as a function of photon energy show an approximately linear energy dependence. Some more  $O^{16} (\gamma, p)$  data has recently become available in the form of preliminary results of measurements of the cross-sections at  $42^\circ$  to the ground state of the residual nucleus  $N^{15}$  up to 200 MeV from MIT<sup>53)</sup>. When these points are added to those from the present experiment, as shown in Fig. 4.18, the trend continues. Interpreted with the plane wave model, this shows that the momentum wavefunction of the bound state decreases monotonically as its argument increases.

Comparing the total cross-sections for the different nuclei at 60 MeV, it can be seen that the ratios between them are approximately  $Li^6 : Li^7 : C^{12} : O^{16} \approx 1 : 1 : 4 : 2$ . Not only are the total cross-sections per nucleon approximately constant, but the shapes of the angular distributions are very similar. There are deviations of  $\sim 30\%$  from this simple relation, but these are probably too small to draw conclusions about the adequacy of the independent particle shell model.

More direct evidence on this point comes from a comparison of the  $(\gamma, p)$  and  $(\gamma, n)$  processes. Recently measurements of  $(\gamma, n)$  cross-sections for  $O^{16}$  and  $C^{12}$  at various photon energies between 63 and 110 MeV have become available<sup>54,55)</sup>. Despite the rather poor resolution of these measurements it is of great interest to compare them with the present  $(\gamma, p)$  results since the shell model predictions for/.....

for the two processes are so different. The shell model predicts the  $(\gamma, n)$  cross-section to be very much less than the  $(\gamma, p)$  cross-section (indeed the  $(\gamma, n)$  process is described by a contribution often presumed negligibly small in comparison with the terms giving the  $(\gamma, p)$  process in the shell model) and to peak in the backward hemisphere unlike the  $(\gamma, p)$  cross-sections which peaks in the forward hemisphere. Combining the results of the two papers just referenced, the total cross-sections for the  $O^{16}(\gamma, n)O^{15}_{g.s.}$  reaction at photon energies of 63 and 79.5 MeV are estimated to be  $32 \pm 4$  and  $16 \pm 2$   $\mu$ barns respectively. Converting the present  $O^{16}(\gamma, p)$  measurements at 60 and 80 MeV to 63 and 79.5 MeV using the cross-section energy-dependence discussed in section 3.5, the  $O^{16}(\gamma, p)N^{15}_{g.s.}$  reaction total cross-sections at these two photon energies are  $54.5 \pm 1.7$  and  $14.40 \pm .76$   $\mu$ barns respectively. This is ample demonstration of the existence and importance of some other reaction mechanism involving more than one nucleon.

## 5.2 Comparison with other ( $\gamma, \beta$ ) experiments

### 5.2.1 Introduction

This experiment is the first to obtain accurate and comprehensive data on the ( $\gamma, \beta$ ) reaction in light nuclei for the energy region between 50 MeV and 100 MeV. This may be attributed to the use of a magnetic spectrometer, the Be-Al photon single difference technique and the accurate beam current monitor. In addition, the cross-sections to the individual states of the residual nucleus have been determined in most cases. The Be-Al photon single difference technique allows best use to be made of the high beam intensity of the accelerator, and both it and the spectrometer make for good resolution. The use of the magnetic spectrometer has the advantage of providing a stable and well established energy calibration together with excellent shielding whilst providing an adequately large solid angle of acceptance and energy coverage.

In order to check the consistency of these results, the next few sections compare where possible, nucleus by nucleus, the results of the present experiment with existing data, the majority of which is listed in the N.B.S. Photonuclear Reaction Data Index<sup>56)</sup>.

### 5.2.2. $\text{Li}^6$

There are only a few existing  $\text{Li}^6$  ( $\gamma, \beta$ ) experiments<sup>57,58)</sup>, and none of these measurements are comparable with the present  $\text{Li}^6$  results/.....

results, since the energy resolution is much poorer and the photon energy range covered does not overlap. Confidence in the present  $\text{Li}^6$  results rests on the agreement of the present  $\text{Li}^7$  results with other  $\text{Li}^7$  data.

### 5.2.3 $\text{Li}^7$

The  $\text{Li}^7$  ( $\gamma, p$ ) experiments are less scarce than the  $\text{Li}^6$ , although a considerable amount of the difference is due to the use of natural lithium targets in the majority of experiments. Of the two experiments <sup>17,19)</sup> most comparable with the present experiment, the better is that of Sanzone et al.<sup>17)</sup> who measured photoproton yield curves from bremsstrahlung for bremsstrahlung endpoint energies in 2.5 MeV steps between 50 and 84 MeV. This enabled them to derive the differential cross-section, at  $(45 \pm 15)^\circ$ , for ejection of p-shell protons as a function of photon energy. A comparison is shown in Fig. 4.15. Their results are consistently higher than those of the present experiment by  $\sim 50\%$ , which exceeds the sum of the systematic errors of  $\sim 10\%$ <sup>16)</sup> and 22% respectively. The present experiment shows some indication, in Fig. 4.3, of the existence of low-lying states in  $\text{He}^6$  above the 1.80 MeV state. This is also seen in the  $\text{Li}^7$  (p,2p)  $\text{He}^6$  data of Roynette et al.<sup>59)</sup> Due to the  $\sim 10$  MeV resolution of the experiment of Sanzone et al., the contribution by any such states would be included in their p-state cross-sections, which would therefore be higher than those of the present experiment which are specifically for the ground state and 1.80 MeV state only.

#### 5.2.4 $C^{12}$

There are more  $C^{12} (\gamma, p)$  experiments than for any of the other nuclei studied. The relevant experiments with which to compare are those of Penner and Leiss<sup>60)</sup>, Taran and Gorbunov<sup>22)</sup>, and Manuzio et al.<sup>16)</sup>.

Penner and Leiss measured five angular distributions of the cross-section leading to the ground state alone of the residual nucleus  $B^{11}$ . The total cross-sections and the differential cross-sections at  $45^\circ$  are shown, together with comparable cross-sections from the present experiment, in Figs. 4.17 and 4.16. Good agreement is obtained, although there is no overlap. Some total cross-sections from the cloud chamber experiment of Taran and Gorbunov are shown in Fig. 4.17. These results are the sums of  $(\gamma, p)$  cross-sections to all particle stable states in the residual nucleus and were analysed with the assumption that the residual nucleus is produced in its ground state, an assumption which will give cross-sections which are a little too low. The total cross-sections to all states below 7 MeV from the present experiment are shown also. The statistical accuracy of the Taran and Gorbunov experiment at high proton energies is not good, but the results seem to be consistently higher than those from the present experiment. This could be due to inclusion of  $(\gamma, pn)$  events with an undetected low energy neutron in the cloud chamber experiment. Manuzio et al. measured the differential cross-section at  $(45 \pm 15)^\circ$  for ejection of a p-shell proton/.....

proton as a function of photon energy between 50 and 75 MeV. Their results are plotted, together with the cross-sections to the ground state and 2.12, 4.44, 5.02 and 6.74 MeV states from the present experiment, in Fig. 4.16. The agreement is good.

Penner and Leiss quote  $(7^{+16})\%$  as the average ratio of the 2.12 MeV state cross-section to the ground state cross-section. This agrees with the present experiment at forward angles. Considering the higher excited states, 4.44, 5.02 and 6.74 MeV, Penner and Leiss estimate the differential cross-section for 60 MeV photons at  $90^\circ$  to these states, assuming all strength to be in the 5.02 MeV state, to be  $(4.8^{+4.8})$   $\mu\text{barns/steradian}$ . The present experiment gives  $(6.5^{+2.4})$   $\mu\text{barns/steradian}$  for this cross-section.

### 5.2.5 $O^{16}$

The  $O^{16}(\gamma, p)$  cross-sections of the present experiment are to the ground state of the residual nucleus  $N^{15}$ . There is only one other set of similar measurements, the preliminary MIT data<sup>53)</sup> already mentioned in section 5.1. These data are differential  $O^{16}(\gamma, p)$  cross-sections to the ground state of  $N^{15}$  at  $42^\circ$  for four photon energies between 124 and 201 MeV. Fig. 4.18 shows these data and the  $45^\circ$  differential cross-sections from the present experiment. The agreement is good, although there is no overlap.

The/.....

The other measurements have not resolved the various states in  $N^{15}$ . Gorbunov and Osipova<sup>21)</sup> have made total cross-section measurements using a cloud chamber to all particle stable states in  $N^{15}$ . Their results, together with the total cross-sections from the present experiment, are shown in Fig. 4.19, and are a factor of  $\sim 2\frac{1}{2}$  to 3 times larger than the present data. Mancini et al.<sup>18)</sup> have made some measurements of cross-sections at  $(43 \pm 20)^\circ$  for ejection of p-shell protons. The differential cross-sections at  $45^\circ$ , extracted from their presented data, together with the differential cross-sections at  $45^\circ$  from the present experiment, are shown in Fig. 4.18, and are consistently higher than the present data by a factor of  $\sim 5$ . Within the large errors of the cloud chamber experiment, these two results are consistent. A factor of  $\sim 3$  is expected on consideration of the relative population of the  $p_{1/2}$  - subshell and the entire p-shell, the present experiment corresponding to ejection of a photoproton from the  $p_{1/2}$  - shell, and the two experiments just mentioned corresponding to the unresolved  $p_{1/2}$  - and  $p_{3/2}$  - shells (see section 5.3.2.5). The factor of  $\sim 5$  is in agreement with some partially analysed and unconfirmed data from MIT<sup>3)</sup> which suggests that the cross-section to the 6.32 MeV state in  $N^{15}$  is about 3 to 4 times greater than the cross-section to the ground state.

### 5.3 Comparison with theory

#### 5.3.1 ( $\gamma, p$ ) calculations

In principle the procedure followed for comparison of experiment with theory is simple. Firstly, the experimental data would be compared with shell model calculations (excluding strong short-range residual interactions). If, as might be expected, these calculations failed to reproduce the magnitudes of the measured cross-sections, then secondly, the effects of the inclusion of various strong residual interactions to raise the cross-sections towards the experimental values would be investigated. From comparison with experiment conclusions about the residual interactions might be possible.

Since several shell model calculations of the ( $\gamma, p$ ) process have been carried out in the past, it might be expected that the first part of the procedure would not present any difficulties. In fact the various shell model calculations give widely varying results (up to a factor of at least 10) and their interpretation is beset by uncertainties. Indeed, the result of comparison with some predictions is that short range residual interactions need not be included.

Some features of ( $\gamma, p$ ) calculations are discussed below. In order to obtain a consistent set of predictions for all the nuclei studied a new programme has been developed; it is discussed in section 5.3.2.1.

Kost/.....

Most calculations have chosen a single particle potential to describe the bound state, for instance the Elton and Swift<sup>61)</sup> single particle potential whose parameters are chosen to fit proton separation energies (from (e,e'p) and (p,2p) experiments) and r.m.s. charge radii (from elastic electron scattering data.) The final state is usually calculated from an optical potential such as the Seth<sup>62)</sup> potential derived from nucleon-nucleus scattering data. Although the initial and final state wavefunctions should presumably be consistent with these experimental data, independently choosing bound and continuum state potentials to satisfy these constraints may lead to corresponding wavefunctions which are not orthogonal. The use of such wavefunctions in  $(\chi, p)$  calculations is incompatible with the first-order time-dependent perturbation theory on which the calculations have been based, because in this theory the orthogonality of the wavefunctions is implicit.

Computations with non-orthogonal wavefunctions will necessarily lead to incorrect results, but the likely magnitude of these errors is in dispute<sup>63,64)</sup>. However, recently a single non-local potential which explains both bound and continuum states has been presented by Gamba et al.<sup>65)</sup> No calculations using this potential have yet been performed, but its use would certainly eliminate the possibility of independently varying bound and continuum state potential parameters which exists at present, and thus force a more consistent description.

A/.....

A further problem with the specification of the bound state arises because the binding energy and radius of the state are insufficient by themselves to determine the Fourier transform of the wavefunction at high momentum. The  $(\gamma, \beta)$  cross-section, which is especially dependent on these high momentum components, is therefore very sensitive to the detailed shape of the bound state potential well. For example, harmonic oscillator wavefunctions, derived from a potential which changes slowly, have lower high momentum components than Woods-Saxon wavefunctions, where the potential changes rather suddenly at the edge of the nucleus.

The use of single particle wavefunctions in shell model calculations means that the  $A$  nucleons in the nucleus are treated as a proton in the field of a core of  $A-1$  nucleons, the core being assumed to be a spectator so that its internal wavefunction does not change during the reaction. This implies that the residual nucleus is a hole state of the target nucleus, an assumption which may well be reasonable for a closed-shell nucleus like  $O^{16}$  but questionable for a nucleus like  $Li^7$ . Some calculations have assumed the core to be immovable; neglect of this centre-of-mass effect can lead to changes of a factor of up to  $\sim 2$  in the predicted cross-sections.

The electromagnetic interaction operator assumed is  $H_1 = \underline{j} \cdot \underline{A}$  where  $\underline{j}$  is the current distribution and  $\underline{A}$  is the vector potential of the electromagnetic field<sup>66)</sup>. When applied to the nuclear photoeffect,  $\underline{j}$  is the total nuclear current, and this must include the meson currents in/.....

in addition to the convection current due to the motion of the (assumed point charge) nucleons. (Exchange of charged mesons is equivalent to moving the charge of a nucleon around without moving the nucleon itself). A calculation which attempts to include the meson exchange currents is discussed later.

For photons in the energy range 50-100 MeV,  $kR \approx 1$ , where  $k$  is the photon wave number and  $R$  is the radius of the nucleus (e.g. for 80 MeV photons on  $C^{12}$   $k \approx .4 \text{ fm}^{-1}$  and  $R \approx 3 \text{ fm}$ .) This is clearly far from the long wavelength limit. Thus the expansion of the electromagnetic interactions operator in multipoles has to be made to quite high order. Truncation at a given order of multipole should not be decided on the basis of convergence of the total cross-section alone. The angular distribution of the cross-section can change dramatically while the total cross-section is almost unaffected as higher multipoles are added.

When the  $A$  nucleons are regarded as a proton and a core of  $A-1$  nucleons, it is probably only realistic for the photon to interact with the proton and not with the core, since the probability that the photon can interact coherently with this massive particle of charge  $Z-1$  and mass  $A-1$  is very small (given by an appropriate form-factor). This shows that the use of effective charges<sup>66,67</sup>, which were developed for much lower photon energies near the giant dipole resonance, to correct for the recoiling charge  $Z-1$  is not appropriate here.

In/.....

In some calculations the extreme assumption has been made of treating the final continuum state as a plane wave. This simplifies the calculation as it is then no longer necessary to expand the photon vector potential  $\underline{A} = \underline{A}_0 e^{i\mathbf{k}_\gamma \cdot \mathbf{r}}$  in multipoles. A further attraction is the structure of the expression for the cross-section as a product of some kinematical factors and the momentum distribution of the nucleus (see Appendix 12,) thus making for a simple interpretation. This means, superficially, that by measuring some angular distributions the bound state momentum wavefunctions may be found, but the obvious problem is the omission of the distortion of the ejected proton as it climbs out of the nuclear well. One method of partially compensating for this omission is to obtain the momentum inside the nucleus  $k_i$  from that observed outside  $k_o$  by adding the depth of the final state potential  $V$  to the observed energy of the proton outside the nucleus i.e.  $k_i^2 = k_o^2 + \frac{2m}{\hbar^2}V$ . Another is the WKB method of treating the final state distortion<sup>10)</sup>, in which the sudden change in wavenumber at the nuclear boundary implied in the last sentence is replaced by a gradual change involving integration of the distorting potential along the classical path of the proton.

The inclusion of residual interactions in  $(\gamma, p)$  calculations will now be discussed. The average nuclear properties such as the mean binding energy are properties which do not depend on the details of the nucleon-nucleon force except to the extent that the strong medium range attractive and even stronger short range repulsive components/.....

components more or less cancel. This cancelling is the justification for the introduction of the single particle shell model and optical potentials. However, in a  $(\gamma, p)$  reaction one of the protons in the nucleus is given a high momentum; this is now no longer an average state, and the details of the nucleon-nucleon force are important. As the photon energy is increased above the giant resonance region, the first effect to become important might be expected to be the medium range attractive component when it has significant Fourier components near the proton momentum. This is largely single  $\pi$ -meson exchange, and Gari and Hebach<sup>68,69)</sup> have included this in a set of  $(\gamma, p)$  cross-section predictions, the effective strength being used as a variable parameter. At higher photon energies the repulsive core with its high momentum Fourier components should become important. Perhaps a Jastrow correlation function<sup>72)</sup> could parametrise this (Fig. 1.3.) In the simplest case of the Jastrow formalism a correlated two-body wavefunction  $\Psi$  is constructed out of two single particle wavefunctions  $\psi_1, \psi_2$  by forming

$$\Psi(\mathbf{r}_1, \mathbf{r}_2) = f(|\mathbf{r}_1 - \mathbf{r}_2|) \psi_1(\mathbf{r}_1) \psi_2(\mathbf{r}_2).$$

The short range behaviour of the correlation function ( $f(r) \ll 1, r \lesssim \frac{1}{2} \text{ fm}$ ) represents the repulsive hard core of the nucleon-nucleon force. The medium range behaviour ( $f(r) > 1, 1 \lesssim r \lesssim 2 \text{ fm}$ ) represents the residual attractive component (mostly single  $\pi$ -meson exchange) which is not included in the single particle self-consistent potential. For distances  $r \gtrsim 2 \text{ fm}$  the correlation function heals; here the correlated/.....

correlated and uncorrelated wavefunctions are identical. In this formalism, used by Weise and others (e.g. refs. 64, 70 and 71), matrix elements are evaluated between correlated initial and final states. The presence of the correlation function enables more than one particle to participate in the transition.

As mentioned above, the nuclear current  $\underline{j}$  includes the current due to exchange of charged mesons between a proton-neutron pair. This is shown in the lower half of Fig. 1.3. Of course the short range correlations represented by a correlation function and charged meson exchange currents are not separate, since all nucleon-nucleon interactions are exchanges of mesons. For example, the meson current component of  $\underline{j}$  could be transformed, through the equation of continuity, into a two-body charge density distribution which could then be absorbed into a Jastrow correlation factor. Gari and Hebach state that this component is included in their  $(\chi, \rho)$  calculations listed in the last paragraph.

Shell model  $(\chi, \rho)$  calculations and calculations including residual interactions are compared with experiment in sections 5.3.2 and 5.3.3 respectively.

### 5.3.2 Comparison with independent particle shell model calculations

#### 5.3.2.1 The $(\gamma, p)$ calculation developed for comparison with present data

For comparison with the data presented in this thesis, new calculations of the  $(\gamma, p)$  cross-section have been made assuming an independent particle shell model bound state and a distorted wave continuum state. The development of the calculational machinery, apart from its obvious and immediate use, has permitted both the investigation of the variation of the predicted cross-section with various parameters and comparison with other published calculations. Details of the calculation are given in Appendices 11 and 13.

The calculation uses a central Woods-Saxon bound state and a continuum state of a central Woods-Saxon complex optical potential with a simplified treatment of the imaginary component of the potential. Centre-of-mass corrections are included, as are electric multipoles up to any order. Spin-orbit coupling has been excluded. Further development is clearly desirable, but it is expected that the important features of the independent particle shell model cross-section are reproduced by the present calculation.

The parameters of the bound state central Woods-Saxon potential

$$V(r) = \frac{-V_0}{1 + e^{\frac{r-R}{a}}}, \quad R = r_0 (A-1)^{\frac{1}{2}}$$

could not just be taken as those of the central component of a standard potential/.....

potential such as that of Elton and Swift<sup>61)</sup> which includes spin-orbit coupling. The features reproduced by the potential had to correspond, as closely as possible, to those reproduced by the standard potentials. Elton and Swift consider that the binding energies and nuclear r.m.s. radii are the important features. Accordingly, the bound state potential was chosen to reproduce the correct binding energy. Since a central potential is characterised by fewer parameters than a potential which includes a spin-orbit component, it is only possible to reproduce either the r.m.s. radius of each shell at the price of a different radius parameter  $r_0$  for each shell or the r.m.s. radius of the nucleus with identical radius parameters but incorrect r.m.s. radii for each shell. This latter case has been used, and the radius parameter is, for every nucleus considered, very close to the value given by Elton and Swift.

The continuum state potential was assumed to be

$$V(r) = \frac{-V_0 - iW_0}{1 + e^{\frac{r-R}{a}}}, \quad R = r_0(A-1)^{\frac{1}{3}}$$

Again, since no spin-orbit coupling was considered, it was necessary to choose parameters from an optical potential which had specifically excluded spin-orbit components throughout its derivation. The potential chosen was taken from McCarthy<sup>73)</sup> and represents a global parameter set for  $r_0 = 1.30$  fm and  $a = .65$  fm. To within the 3 MeV mentioned below, the depth of the real potential agrees with, for example/.....

( $\gamma, p$ ) cross-section calculation parameters

Bound state

Continuum state

$$V(r) = \frac{-V_0}{1 + e^{\frac{r - r_0 (A-1)^{\frac{1}{3}}}{a}}}$$

$$V(r) = \frac{-V_0 - iW_0}{1 + e^{\frac{r - r_0 (A-1)^{\frac{1}{3}}}{a}}}$$

nucleus	$E_\gamma$ (MeV)	$V_0$ (MeV)	$r_0$ (fm)	$a$ (fm)	binding energy (MeV)	$V_0$ (MeV)	$W_0$ (MeV)	$r_0$ (fm)	$a$ (fm)	absorptio facto
$Li^6$	60	51.2	1.46	.65	4.9	32.0	10.5	1.30	.65	.559
$Li^7$	60	61.8	1.41	.65	11.5	33.0	10.0	1.30	.65	.548
	80	61.8	1.41	.65	11.5	30.0	12.0	1.30	.65	.516
$C^{12}$	60	52.1	1.38	.55	15.8	33.0	10.0	1.30	.65	.477
	80	52.1	1.38	.55	15.8	30.0	12.0	1.30	.65	.446
	100	52.1	1.38	.55	15.8	27.5	13.5	1.30	.65	.432
$O^{16}$	60	40.9	1.39	.65	12.3	32.5	10.5	1.30	.65	.432
	80	40.9	1.39	.65	12.3	29.5	12.5	1.30	.65	.402
	100	40.9	1.39	.65	12.3	27.0	14.0	1.30	.65	.389

TABLE 5.1

example, the depths given by Satchler<sup>74)</sup> for the specific cases of  $C^{12}$  and  $Be^9$  at  $\sim 45$  MeV. The approximation used for the imaginary absorptive component of the optical potential is to multiply the wavefunction corresponding to the real component of the optical potential by a factor derived with the assumption that the outgoing wave is a plane wave and that the imaginary potential is constant out to the characteristic radius  $R$  of the Woods-Saxon potential and zero thereafter (see Appendix 14). The multiplicative factor is typically  $\sim \frac{1}{2}$ .

The calculation has been checked by setting the optical potential to zero whereupon cross-sections were produced which were identical with those obtained from a plane wave calculation with its much simpler and different formalism (Appendix 12). Also, it has been verified that the calculation agrees with that of Fink et al.<sup>63)</sup> These authors state that they neglected centre-of-mass corrections, and therefore, before comparison, the present calculation was altered to remove all centre-of-mass effects. With the parameters used by Fink et al. - identical Woods-Saxon wells in the bound and continuum states,  $V_0 = 52$  MeV,  $R = 3.2$  fm,  $a = .65$  fm - the present calculation then produced total cross-sections which agreed with those of Fink et al.

Changing the radius parameter from the value common to each shell reproducing the nuclear r.m.s. radius to the value reproducing the r.m.s. radius of the subshell from which the proton is ejected had the following effects:  $Li^6$ ,  $Li^7$  and  $C^{12}$  cross-sections decreased by  $\sim 10\%$ ,  $O^{16}$  cross-sections increased by a factor of  $\sim 2\frac{1}{2}$ . The calculation also/.....

also reproduced the effect noted by Mougey et al.<sup>75)</sup>, who showed that calculated distorted momentum distributions can change by a factor of  $\sim 2$  if the bound state r.m.s. radius is altered by  $\sim 10\%$ ; it was found that the  $C^{12}(\gamma, p)$  cross-sections were increased by a factor of  $\sim 2$  when the r.m.s. radius of the bound state wavefunction was decreased by 5%. The effect of changing the depth of the real component of the optical potential was investigated. For  $O^{16}$  at  $E_\gamma = 80$  MeV, changing this from 29.5 MeV (the depth specified by McCarthy) by 3 MeV (the maximum variation among p-shell nuclei given by Watson et al.<sup>76)</sup> in either direction changes the cross-section by 40%, increasing the depth of the potential decreasing the cross-section and vice versa. Glassgold and Kellogg<sup>77)</sup> have derived optical potentials of the above form for  $C^{12}$  at 40 MeV (the proton energy appropriate to 60 MeV photons) for two different values of the radius parameter  $r_0$ , 1.31 and 1.20 fm, for which the optimised fit to the proton scattering data is equally good. When used as the continuum state for the  $C^{12}(\gamma, p)$  reaction at  $E_\gamma = 60$  MeV, the  $r_0 = 1.20$  fm potential leads to a cross-section 35% less than the  $r_0 = 1.31$  fm potential. These considerations show the extent to which the present calculation, and presumably other similar calculations, produce reliable quantitative predictions.

#### 5.3.2.2 Li<sup>6</sup>

Fig. 4.6 shows the calculated angular distribution of the  $Li^6(\gamma, p)$  reaction cross-section at a photon energy of 60 MeV. The cross-section/.....

section was calculated using the bound and continuum state parameters shown in Table 5.1. The calculation underestimates the data by a factor of  $\sim 1\frac{1}{2}$ .

The relevant published calculations with which to compare the present data are those of Radhakant<sup>78)</sup> who calculates the 60 MeV angular distribution for this reaction for several different bound and continuum state wavefunctions for purposes of comparison. Considering only his calculations involving Woods-Saxon wavefunctions, use of an optical potential with surface absorption (Ulehla et al.<sup>79)</sup>) produces a reasonable fit to the data whereas a different optical potential with volume absorption (Jain and Jackson<sup>80)</sup>) produces cross-sections  $\sim 2\frac{1}{2}$  times larger. Although Radhakant claims to use Elton and Swift<sup>61)</sup> wavefunctions for his bound state, the parameters quoted in Table 1 of his paper are not those of Elton and Swift. Assuming similar notation, Radhakant's parameters give rise to a binding energy of 10.0 MeV instead of 4.9 MeV, and the r.m.s. radius of his  $1p_{3/2}$  wavefunction is 2.79 fm. whereas the r.m.s. radius of the corresponding Elton and Swift wavefunction is 3.13 fm. This would make Radhakant's cross-sections too high by a factor of  $\sim 2$ . The present calculation agrees with the calculation of Radhakant involving surface absorption to 35%.

These calculations are probably not particularly appropriate.  $Li^6$  has considerable cluster structure  $\alpha-d, t-\tau$  (52,81), and this is not consistent with the shell model. Also the optical potential description/.....

description of the interaction of the outgoing photoproton with a nucleus as light as the residual nucleus  $\text{He}^5$  may well be questioned.  $\text{He}^5$  is unstable against neutron decay with a half-life of  $5 \times 10^{-21}$  sec (admittedly a long time compared with the time for the photoproton to travel through the nucleus,) and Nakamura<sup>52)</sup> shows that the proper description of the final state very probably should include the explicit interaction of the outgoing proton with the odd neutron of  $\text{He}^5$ .

### 5.3.2.3 $\text{Li}^7$

Figs. 4.7 and 4.8 show the calculated angular distribution of the  $\text{Li}^7 (\gamma, p)$  reaction cross-section at photon energies of 60 and 80 MeV. The cross-section was calculated using the bound and continuum state parameters shown in Table 5.1. The calculated values are too high by a factor of  $\sim 1\frac{1}{2}$ . The differential cross-section at  $45^\circ$  as a function of photon energy is shown in Fig. 4.15.

Weise<sup>64,82)</sup> and Radhakant<sup>78)</sup> have recently calculated the p-shell angular distributions of the  $\text{Li}^7 (\gamma, p)$  cross-section, Weise at 60 MeV, Radhakant at 60 and 80 MeV. Radhakant's calculations are similar to his  $\text{Li}^6$  calculations, and again his parameters are not those of Elton and Swift<sup>61)</sup>. Weise calculates for an Elton and Swift bound state and an optical potential of Seth<sup>62)</sup> with surface absorption for the continuum state. At 60 MeV Radhakant's calculation using surface absorption/.....

absorption is very similar to the present calculation. Again his calculation with volume absorption is  $\sim 2\frac{1}{2}$  times higher. Weise's 60 MeV calculation is very much lower. At 80 MeV both Radhakant's predictions overestimate experiment by more than at 60 MeV.

The order-of-magnitude difference between Weise's and Radhakant's predictions is most puzzling. Both authors state they use Elton and Swift bound state wavefunctions. The optical potentials with surface absorption are very similar; Weise uses a Woods-Saxon derivative form-factor for the surface absorption component and Radhakant uses a Gaussian, but the two potentials are very similar. Although Radhakant includes centre-of-mass corrections whereas Weise does not, this cannot explain the difference. Ciolfi degli Atti<sup>83)</sup> and Nakamura and Izutsu<sup>11)</sup> have cast doubt on similar calculations by Radhakant of distorted momentum distributions for the  $(e, e'p)$  reaction. This, together with the discrepancy between Radhakant's bound state and the Elton and Swift specifications means that there must be some doubt about the validity of Radhakant's calculations. However the present calculation does tend to agree with Radhakant.

Like  $\text{Li}^6$ ,  $\text{Li}^7$  has considerable cluster structure, so again the shell model does not provide a particularly good description of the bound state. These calculations, like the  $\text{Li}^6$  calculations, should probably not be taken too seriously.

5.3.2.4 C<sup>12</sup>

Figs. 4.9, 4.10 and 4.11 show the calculated angular distributions of the C<sup>12</sup> ( $\gamma, p$ ) reaction cross-section at photon energies of 60, 80 and 100 MeV. The cross-section was calculated using the bound and continuum state parameters shown in Table 5.1. The calculation predicts cross-sections which are, compared with the experimental cross-sections to the ground state, too low by a factor of  $\sim 1\frac{1}{2}$  at 60 MeV, too low by a factor of  $\sim 2$  at 80 MeV and too low by a factor of  $\sim 3$  at 100 MeV. Which cross-sections should be compared with an independent particle shell model calculation is not clear. The differences in angular dependence of the cross-sections to the different states show that different reaction mechanisms are involved, but the independent particle shell model can but refer to the p-shell of C<sup>12</sup> as a whole. The total cross-section and the differential cross-section at 45° as functions of photon energy are shown in Figs. 4.17 and 4.16.

For C<sup>12</sup> Weise<sup>64,82)</sup> and Radhakant<sup>78)</sup> have performed calculations similar to those for Li<sup>7</sup> with similar results. The present calculation predicts cross-sections in between those predicted by Weise and Radhakant.

5.3.2.5 O<sup>16</sup>

Of the four nuclei for which data has been accumulated in the/.....

the present experiment,  $O^{16}$  is the nucleus for which the shell model ( $\gamma, p$ ) calculations should be the most reasonable. Unlike the other three residual nuclei,  $N^{15}$  has a large gap ( $>5$  MeV) between the ground state and the first excited state, which is of opposite parity to the ground state in any case<sup>41)</sup>. The energy gap between the ground state and the first excited state of normal parity is greater than 6 MeV, and so the ground state of  $N^{15}$  should be a good hole state. Also the use of an optical potential, the optical model being developed primarily for medium to heavy nuclei, will be more valid for the continuum state in this reaction than for the other three reactions involving lighter nuclei.

Figs. 4.12, 4.13 and 4.14 show the calculated angular distributions of the  $O^{16} (\gamma, p)$  reaction cross-section at photon energies of 60, 80 and 100 MeV. The cross-section was calculated using the bound and continuum state parameters shown in Table 5.1. The calculation consistently underestimates experiment by an order of magnitude and gives angular distributions with a dip in the middle which is totally different from the experimental angular distribution. The total cross-section as a function of photon energy is shown in Fig. 4.19.

All the published calculations for  $O^{16}$  have been made with the assumption that the closed p-shell is not split. Presuming that ejection of a proton from the  $p_{1/2}$ - shell of  $O^{16}$  leads to the  $\frac{1}{2}^-$  ground state of  $N^{15}$  and ejection from the  $p_{3/2}$  - shell to the 6.32 MeV  $3/2^-$  excited/.....

excited state, the quantity to compare with these calculations should be the sum of the cross-sections to these states. However, only the ground state cross-sections have been measured in this experiment. The ratio of the populations of the  $p_{3/2}$  - and  $p_{1/2}$  - states is 2 : 1, and so assuming that the cross-section for ejection of a  $p_{3/2}$  proton is the same as that for a  $p_{1/2}$  proton, the predictions of the published calculations have been divided by three before comparison. Even if this factor is wrong by 50%, the conclusions drawn will <sup>be</sup> seen to be unaltered.

Fink et al.<sup>63)</sup> have calculated 60 and 80 MeV angular distributions for an average p-state. The bound state is a central Woods-Saxon state giving a binding energy of 17.2 MeV and an r.m.s. radius within 3% of the Elton and Swift<sup>61)</sup> value of 2.85 fm. for the p-state wavefunctions. The continuum state is the real central component of the Seth<sup>62)</sup> optical potential. There are no centre-of-mass corrections. This calculation underestimates experiment (though by less than the present calculation) and gives angular distributions which are the wrong shape, but the calculation should be expected to give cross-sections which are too high since the choice of optical potential is unreasonable (the real central component of the Seth potential was not derived by optimally fitting it alone to the proton-nucleus scattering data).

Fink et al.<sup>63)</sup> and Weise and Huber<sup>84)</sup> have calculated  $O^{16}$  ( $\alpha, p$ ) total cross-sections. Fink et al. calculate for the bound state/.....

state detailed in the last paragraph and two different continuum states: the continuum state detailed in the last paragraph and a continuum state belonging to the bound state potential (and therefore orthogonal to it). Weise and Huber calculate for orthogonal bound and continuum states derived from a real central potential almost identical with the bound state potential used by Fink et al. Some 10% differences between the cross-sections for the two sets of orthogonal states are expected due to the slight difference between the potentials used, but the actual discrepancy is much larger than this, although they both seriously underestimate experiment. The non-agreement of Weise and Huber with Fink et al. is not understood. As mentioned in section 5.3.2.1, the present calculation supports Fink et al.

#### 5.3.2.6 Conclusions

The various different shell model ( $\chi, \rho$ ) calculations give very different predictions. Weise and Huber<sup>84)</sup>, Fink et al.<sup>63)</sup> and the present calculation more or less agree for  $O^{16}$ . However the other Weise calculations<sup>64,82)</sup> for  $Li^7$  and  $C^{12}$  are more sophisticated and so it does not follow that because his  $O^{16}$  calculation is more or less valid then his  $Li^7$  and  $C^{12}$  calculations are also valid. Radhakant<sup>78)</sup> appears to use inconsistent parameters. Clearly further calculations with spin-orbit coupling and rigorous treatment of the imaginary component of the optical potential are desirable. This should show whether the differences in the various shell model predictions are genuine or erroneous.

The/.....

The worth of the present calculation is the consistent set of predictions for all the nuclei studied. The extent to which the results are credible have been discussed in section 5.3.2.1. When these uncertainties are considered, reasonable conclusions are: firstly, the predicted cross-sections more or less agree with the experimental lithium cross-sections, underestimate the carbon cross-sections somewhat, and seriously underestimate the oxygen cross-sections, and secondly, the predicted angular distribution shapes do not agree with the shapes of the experimental cross-section angular distributions.

Experimentally the cross-sections per proton are approximately the same for the four nuclei studied. To investigate the systematic change in  $(\gamma, p)$  shell model predictions with the atomic weight  $A$ , the  $(\gamma, p)$  total cross-section was calculated for ejection of protons from the  $1p$ -shell of a whole range of fictional nuclei of different  $A$ . The bound state was described by a potential

$$V(r) = \frac{-V_0}{1 + e^{\frac{r - r_0(A-1)^{\frac{1}{2}}}{a}}}$$

with  $r_0 = 1.41$  fm,  $a = .65$  fm and  $V_0$  chosen to give a binding energy of 10 MeV. The continuum state was described by a similar potential with  $V_0 = 33$  MeV,  $r_0 = 1.30$  fm and  $a = .65$  fm. Fig. 5.1 shows the variation of the total cross-section with  $A$  for 60 and 120 MeV photons. There is a wiggle superimposed on a cross-section which decreases as  $A$  increases, and/.....

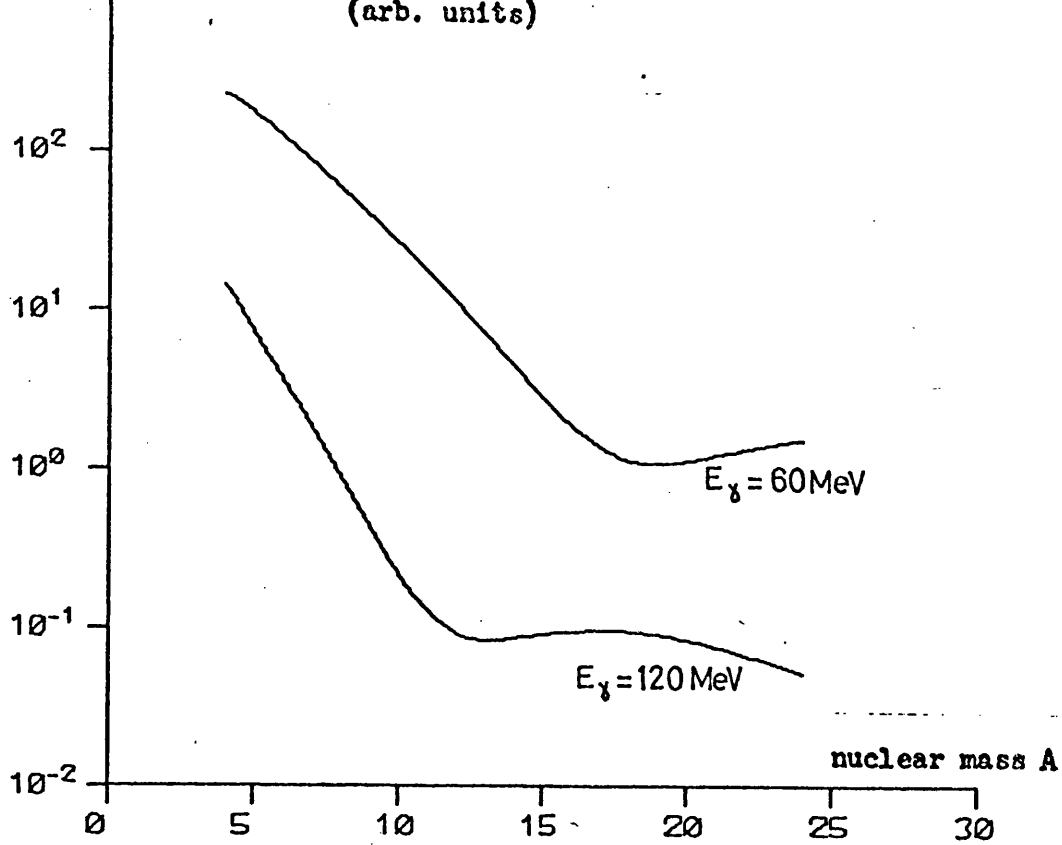
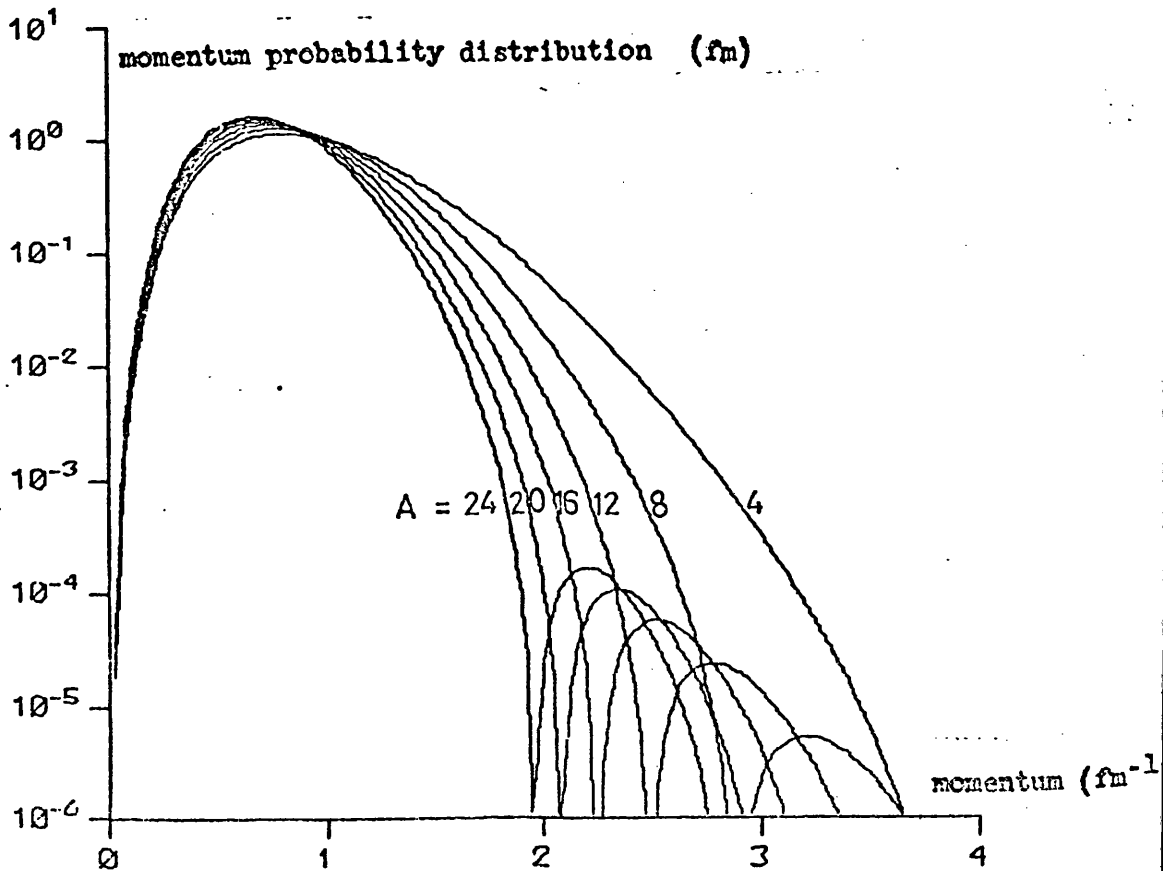


FIG. 5.1 Single-particle shell model  $(\gamma, p)$  cross-section as a function of nuclear mass  $A$

FIG. 5.2 Single-particle shell model momentum distribution as a function of nuclear mass  $A$



and this wiggle moves to lower  $A$  as the photon energy increases. The behaviour does not agree with experiment.

This can be understood in terms of the behaviour of the momentum distribution of the initial bound state. In the simplest model of the  $(\gamma, p)$  process, where the proton is ejected with a cross-section proportional to the probability that in the bound state the proton has a momentum equal to the (vector) difference of the momenta of the outgoing proton and the incoming photon, the angular distribution of the cross-section is directly related to the momentum distribution (see the plane-wave treatment of the  $(\gamma, p)$  process, Appendix 12). The dip in, for example, the  $O^{16}$  predicted angular distribution suggests a deficiency of some particular value of momentum in the bound state (the dip moves to smaller angles as the photon energy increases). When the momentum distribution of the  $O^{16}$  bound state (Table 5.1) is evaluated there is a dip at  $\sim 400$  MeV/c as shown in Fig. 5.4. The  $O^{16}$  experimental momentum distribution (see section 5.4) is also shown. There is no evidence of a dip. The systematic variation of the momentum distribution with  $A$  (using the bound states detailed in the last paragraph) is shown in Fig. 5.2. The dip in the momentum distribution moves to lower momenta as  $A$  increases. This explains the behaviour of the total cross-section described in the last paragraph.

The dips in the cross-section angular distributions are perhaps the best evidence for the inadequacy of the shell model explanation of the  $(\gamma, p)$  process. This evidence does not include any assumptions about details of the bound state (binding energy, r.m.s. radius, etc.) or the continuum state (validity of optical potential, etc/.....

etc.,) assumptions which must be made if proof of shell model inadequacy is to be based on underestimation of experimental cross-sections due to a deficiency of high momentum components in shell model wavefunctions (the traditional approach). Clearly residual interactions are required to "fill in" the dips in the momentum distribution.

### 5.3.3 Comparison with calculations involving residual interactions

#### 5.3.3.1 Introduction

Calculations for various diverse processes involving high momenta in the framework of the shell model but with the addition of residual interactions between nucleons have been reasonably successful in explaining discrepancies between experiment and shell model theory<sup>4)</sup>. These calculations have often used Jastrow correlation factors. ~~A convenient form for the correlation factors.~~ A convenient form for the correlation function is  $f(r_{12}) = 1 - j_0(q_c r_{12})$  because this form is computationally simple. The Fourier transform of  $j_0(q_c r)$  is a delta-function  $\delta(q - q_c)$  and physically this corresponds to the exchange between nucleons of a unique momentum  $q_c$ . Clearly this is not very realistic. Weise<sup>64,82)</sup> has used an extension<sup>4)</sup> of this idea to simulate the exchange between nucleons of a Gaussian momentum package characterised by a mean momentum  $\bar{q}_c$  and width  $\Delta q_c$ . This is a little more realistic. Some examples of high momentum processes whose description is improved by the introduction of short range correlations are/.....

are the  $C^{12} (e, e'p)$ ,  $C^{12} (p, \pi^+)$  and  $C^{12} (\pi^-, NN)$  reactions investigated by Köbberling et al.<sup>12)</sup>, Dillig et al.<sup>85)</sup> and Morris and Weber<sup>70)</sup> respectively. They all find that using a Jastrow correlation factor of the form  $1 - j_0(q_c r)$  with  $q_c \simeq 300$  MeV/c gives a better description of experiment. However, the fits to the data are not particularly good, and so the value  $q_c = 300$  MeV/c is by no means definitive.

There are no existing calculations involving residual interactions with which the present  $Li^6$  experimental results can be compared.

### 5.3.3.2 $Li^7$

Weise<sup>64,82)</sup> has made calculations for  $Li^7$  involving short range correlations. Predictions are made of the  $Li^7 (\gamma, p)$  cross-section angular distribution for 60 MeV photons and the energy dependence of the differential cross-section at  $45^\circ$  for p-shell ejection using a Jastrow correlation factor simulating the exchange between nucleons of a Gaussian momentum package peaked at  $\bar{q}_c = 300$  MeV/c with a standard deviation of  $\frac{\Delta q_c}{\sqrt{2}}$  where  $\Delta q_c = 100$  MeV/c. The angular distribution, shown in Fig. 4.7, fits the data quite well, but the energy dependence of the differential cross-section at  $45^\circ$ , shown in Fig. 4.15, indicates that this agreement is fortuitous.

Weise's shell model prediction (section 5.3.2.3) is certainly shifted nearer experiment by the introduction of correlations although the predictions of the present (shell model) calculation fit the /.....

the data equally well. However the result of introducing correlations, is to add further terms<sup>4,64)</sup> to the single particle shell model  $(\chi, \rho)$  matrix element, and so Weise's predictions using correlated wavefunctions may be more or less independent of his shell model predictions.

### 5.3.3.3 C<sup>12</sup>

Weise<sup>64,82)</sup> has made calculations for C<sup>12</sup> which are similar to his calculations for Li<sup>7</sup>. These are shown in Figs. 4.9, 4.10 and 4.11. Agreement is good for  $\bar{q}_c = 300$  MeV/c at 60 MeV but bad at 100 MeV, as can be seen from the total cross-sections in Fig. 4.17. Fig. 4.16 shows the energy dependence of the differential cross-section at  $45^\circ$ .  $\bar{q}_c = 350$  MeV/c gives better results for the 80 and 100 MeV angular distributions, but it is clear that the data cannot be consistently explained although the introduction of the correlations certainly removes the dips in the angular distributions discussed in section 5.3.2.6.

Shklyarevskii<sup>86)</sup> has calculated C<sup>12</sup>  $(\chi, \rho)$  total cross-sections for an harmonic oscillator bound state (not particularly realistic) and a crude optical potential for the final state using a correlation function  $e^{-\beta r^2}$ . Agreement with the 60 MeV total cross-section from the present experiment and with the total cross-sections between 25 and 60 MeV of Penner and Leiss<sup>60)</sup> is good for  $\beta = .55 \text{ fm}^{-2}$  (which corresponds<sup>70)</sup> very roughly to  $q_c \approx 350$  MeV/c).

#### 5.3.3.4 $O^{16}$

Again the calculations for  $O^{16}$  have been made with the assumption that the p-shell is not split, and so, as in section 5.3.2.5, the predictions have been divided by three before comparison with the data.

Fink et al.<sup>63)</sup> have calculated a correlation factor from many-body theory by solving the Bethe-Goldstone equation for a somewhat unrealistic nucleon-nucleon potential with a hard core and an exponential tail. Using this correlation function it is found that short range correlations are unimportant below 100 MeV, at which energy they only contribute 10% to the cross-section.

Gari and Hebach<sup>68)</sup> have evaluated a contribution to the  $(\gamma, p)$  process which they attribute to meson exchange currents. This is effected by including a single  $\pi$ -meson exchange potential of adjustable depth in the interaction Hamiltonian; there is no hard core. When applied to the case of the  $O^{16}(\gamma, p)$  reaction<sup>69)</sup>, the total cross-section produced, as a function of photon energy, agrees very well with the data as can be seen in Fig. 4.19. The agreement, however, between the 60 MeV angular distributions is not so good as can be seen in Fig. 4.12.

Weise and Huber<sup>84)</sup> have investigated the result of introducing a Jastrow correlation factor  $1-j_0(q_c r)$  into their  $O^{16}(\gamma, p)$  shell model total cross-section calculation discussed in section/.....

section 5.3.2.5. For  $q_c = 300$  MeV/c the result is shown in Fig. 4.19; very clearly it is inconsistent with the data. The total cross-sections for 60 and 100 MeV photons are also given as functions of the correlation parameter  $q_c$ . Agreement with experiment would require  $q_c$  to be 270 MeV/c at 60 MeV and 410 MeV/c at 100 MeV.

### 5.3.3.5 Conclusions

The various ( $\chi, \rho$ ) calculations which include residual interactions do so in different ways. The longest range residual interaction left out of the shell model is single  $\pi$  - meson exchange with a characteristic range of 1.44 fm; this is included by Hebach and his calculation produces results probably less inconsistent with experiment than any others. The characteristic range of the Gaussian correlation function used by Shklyarevskii is also  $\frac{1}{\sqrt{.55}} \approx 1.4$  fm. This contrasts sharply with the healing distance  $\approx 2$  fm of the correlation function used by Weise with correlation parameters corresponding to the exchange between nucleons of a momentum of 300 MeV/c. This distance (about the same as the radius of the  $C^{12}$  nucleus) is unreasonably large; equivalently, the momentum exchange parameter of 300 MeV/c is too low. The wound volume, the volume of the hole punched out of the wavefunction by the correlation function, for a correlation parameter of 300 MeV/c is seven times<sup>5)</sup> greater than that from a solution of the Bethe-Goldstone equation, and wound volumes of this magnitude are shown by Mougey et al.<sup>75)</sup> to appreciably change the/.....

the r.m.s. radii of the wavefunctions from their accepted values<sup>61</sup> thus producing spurious effects. Such correlations are really too long range to be described as short range correlations.

The much used correlation factor  $1 - j_0(q_c r)$ , corresponding to a distribution of transferred momentum which is  $\delta$ -function, is clearly physically unreasonable but is attractive because of computational convenience. However, a correlation factor composed of a sum of these single momentum correlation factors with appropriate partial amplitudes to produce an approximation to a more reasonable transferred momentum distribution may well lead to better results.

The introduction of residual interactions certainly raises the shell model  $(\gamma, \beta)$  cross-sections and removes the dips in their angular distributions. No treatments explain experiment satisfactorily, but it is probably reasonable to conclude that these various calculations indicate the manner in which more realistic treatments of the  $(\gamma, \beta)$  process can proceed.

#### 5.4 Momentum distributions

The  $(\gamma, p)$  reaction is a single nucleon knock-out reaction like the  $(e, e'p)$  and  $(p, 2p)$  reactions. The purpose of  $(e, e'p)$  and  $(p, 2p)$  quasi-free scattering<sup>10)</sup> experiments has been, up to now, to measure binding energies and bound state momentum distributions, the latter being of interest because they are related through Fourier transformations to the bound state configuration space wavefunctions. However, determination of a momentum distribution by experiment is hampered by the distortion of the proton wavefunction, and in practice for quasi-free scattering a "distorted momentum distribution" is obtained by analysing the experimental data as if there were no distortion.

A momentum distribution extracted from a  $(\gamma, p)$  experiment will be more model-dependent than that from a quasi-free scattering experiment. However, it is of interest to see whether self-consistent  $(\gamma, p)$  momentum distributions can indeed be obtained and whether they match the momentum distributions obtained from corresponding quasi-free scattering experiments. Only the  $(e, e'p)$  reaction will be considered since the final state distortion (one strongly interacting particle) should be similar to that involved in the  $(\gamma, p)$  reaction, whereas the  $(p, 2p)$  reaction involves the severe distortion produced by the strongly interacting projectile and ejected proton. It is only recently that  $(e, e'p)$  experiments have determined momentum distributions/.....

distributions for momenta greater than about 200 MeV/c and so a comparison between the momentum distributions produced by (e,e'p) and ( $\gamma, p$ ) reactions has not previously been possible. However such experiments have been performed at Saclay<sup>87)</sup> and DESY<sup>12,88)</sup>.

The ( $\gamma, p$ ) momentum distributions presented in this section have been obtained using plane wave formalism (see Appendix 12).

From the experimental cross-sections, the quantity

$$\frac{1}{2l+1} \sum_m |\phi(q)|^2$$

is calculated. The effect of distortion has been approximated by adding the depth of the final state potential to the observed energy of the outgoing proton, and the absorption has been approximated by using a multiplicative correction factor (see Appendix 14). Again it should be emphasised that the ( $\gamma, p$ ) momentum distributions are model-dependent; they should be viewed with circumspection.

Fig. 5.3 shows the momentum distributions extracted from the  $C^{12}(\gamma, p) B_{g.s.}^{11}$  cross-sections of the present experiment for final potential depths of 0 and 37 MeV. (These depths represent no correction for distortion and an average correction based on the distorted wave  $C^{12}$  80 MeV angular distributions). For compatibility with (e,e'p) experiments no corrections have been made here for absorption. The inclusion of distortion clearly leads to greater self-consistency. Also shown are the results of Bernheim et al.<sup>87)</sup> (Saclay) for the p-shell momentum distribution. Distortion is not expected/.....

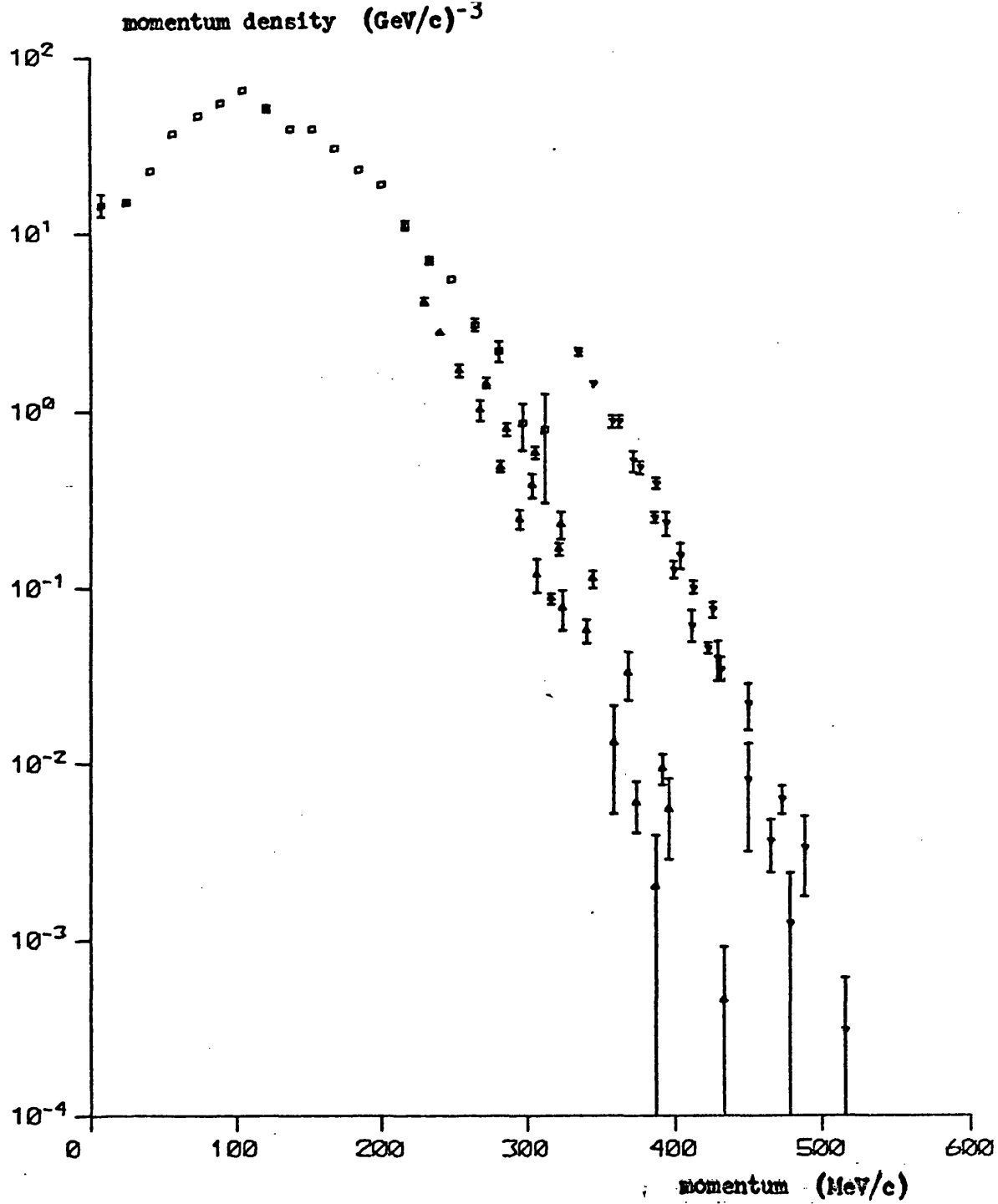


FIG. 5.3  $\text{C}^{12}$  p-shell momentum distribution

- Saclay:  $(e, e'p)$
- △ present experiment:  $V_{\text{final state}}^{\text{real}} = 0 \text{ MeV}$
- ▽ present experiment:  $V_{\text{final state}}^{\text{real}} = 37 \text{ MeV}$

expected to be important in this (e,e'p) experiment<sup>11)</sup>. The results of the DESY experiment are not included because s- and p-shell protons were not distinguished. The ( $\chi, p$ ) and (e,e'p) momentum distributions are not inconsistent. However, further investigation is required, both into the model dependence of the ( $\chi, p$ ) results and the dependence of the (e,e'p) results on the kinematics of the experiment.

Fig. 5.4 shows the  $O^{16}$  momentum distribution deduced from the present experimental results and the four extra points recently available from MIT<sup>53)</sup>. This momentum distribution covers a greater range of momenta and is quite self-consistent. (Incidentally, the MIT results do not extend to a higher momentum than those of the present experiment. Although the highest energy MIT point (200 MeV) is at twice the photon energy of the highest point of the present experiment (100 MeV), the difference in angles ( $42^\circ$  and up to  $120^\circ$  respectively) is sufficient to compensate for the difference in energies, as illustrated in Fig. 1.1.) A final state potential of 37 MeV (based on the distorted wave  $O^{16}$  80 MeV angular distribution) and a factor of .4 (Table 5.1) have been used as average corrections for distortion and absorption. Also shown is the  $O^{16}$  shell model momentum distribution (see section 5.3.2.6); the discrepancy is obvious. There are no comparable  $O^{16}$  (e,e'p) results,

The/.....

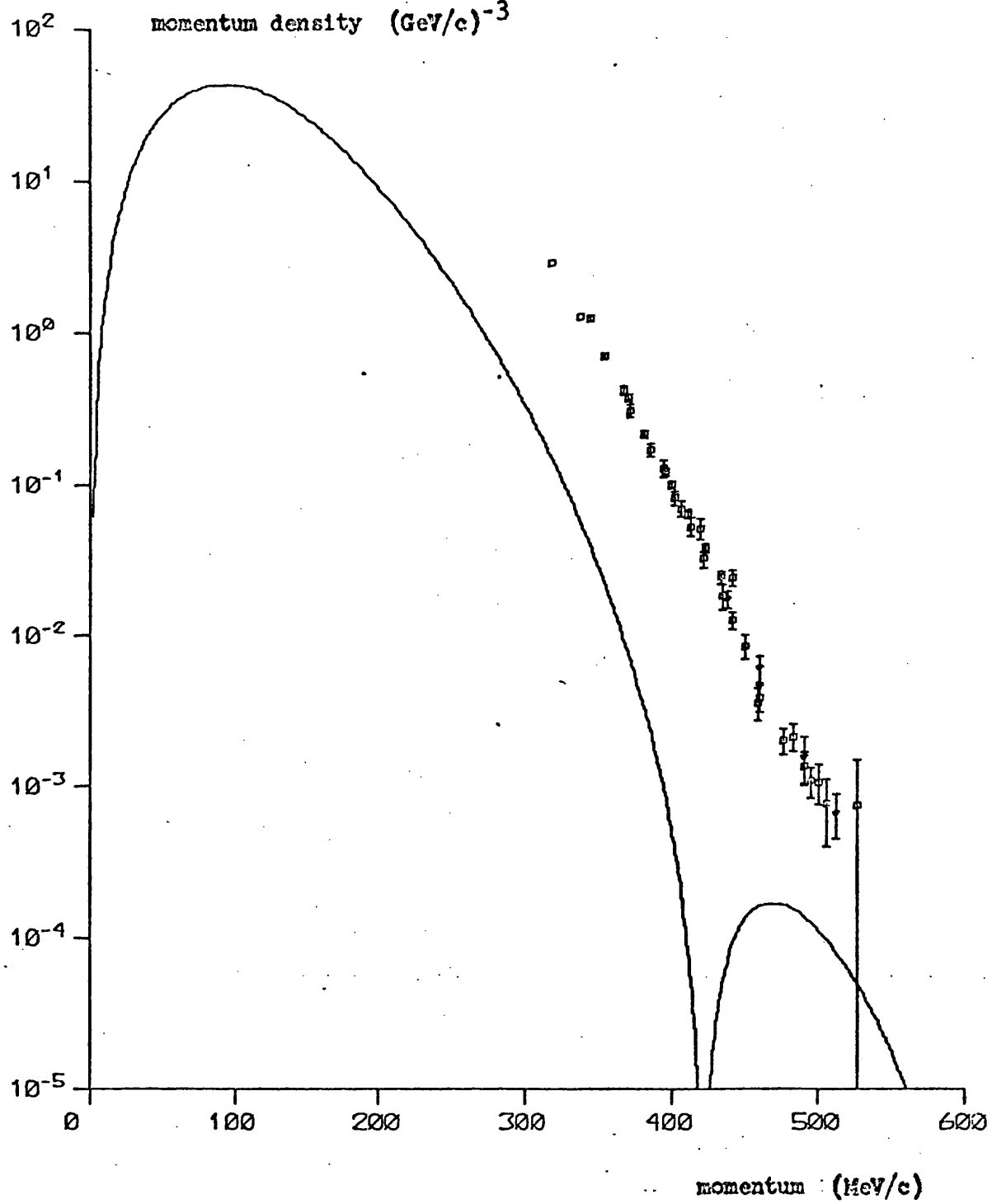


FIG. 5.4  $^{16}\text{O}$   $p_{1/2}$ -shell momentum distribution

- single-particle shell model
- present experiment
- ◇ HIT

The most important fact about these momentum distributions is that a single self-consistent distribution can be obtained from several angular distributions at various different photon energies. This demonstrates that it is quite reasonable to regard the  $(\gamma, p)$  process as depending only on the momentum which must be provided by the initial bound state to make up the difference between the momenta of the incoming photon and outgoing proton regardless of the energy of the photon and the angle and energy of the emergent proton.

## 5.5 Conclusions

It is clear that at present the theoretical treatment of the medium to high energy nuclear photoeffect is in a less satisfactory state than the experimental studies. Perhaps this situation has arisen because of the scarcity of accurate, specific and comprehensive data; it is therefore to be hoped that the present experiment will be of some use in stimulating further theoretical studies.

The shell model, when applied to cases where it is expected to be most reasonable, definitely seems to produce predictions inconsistent with experiment. This can apparently be simply related to the details of the momentum wavefunction of the bound state.

The existence of a self-consistent experimental momentum distribution derived from  $(\gamma, p)$  reaction cross-section measurements shows that the simplest interpretation of the  $(\gamma, p)$  process is reasonable.

Single  $\pi$ -meson exchange between nucleons is the residual interaction with the longest range. When this interaction is included,  $(\gamma, p)$  cross-section predictions come nearest to experiment.

The Jastrow correlation factor  $1-j_0(q_0 r)$  with  $q_0 \approx 300$  MeV/c has been much used to explain various diverse high momentum processes. However/.....

However the  $(\gamma, p)$  reaction cannot be so explained and this therefore reduces the validity of the explanations of the other processes. It has also been shown that for no single value of  $q_0$  is a consistent explanation of the  $(\gamma, p)$  process possible.

### 5.6 Future developments

The extension of the present measurements to higher energy would be valuable. The higher the energy the smaller are effects due to distortion in the final state and the more important become short range effects. Some very preliminary  $(\gamma, p)$  measurements up to 300 MeV have already been made on  $O^{16}$  at MIT<sup>3)</sup>. The cross-section appears to continue to fall from the present values up to  $\sim 260$  MeV after which it starts to rise. It has been suggested that this rise is due to nuclear isobar formation although isobar formation had not previously been found to be important in medium to heavy nuclei.

Investigation of heavier nuclei would be of interest. For  $(\gamma, p)$  reactions to states near the ground state the shell model contribution to the cross-section is proportional to the number of nucleons in the outermost shell, but the contribution due to correlations should presumably depend more on the total number of nucleons and therefore should be more important for heavier nuclei.

For/.....

For example, the  $\text{Ca}^{40} (\gamma, p) \text{K}^{39}$  reaction might be an appropriate choice. Like  $\text{O}^{16}$ ,  $\text{Ca}^{40}$  is a doubly magic nucleus and the overlap of the ground states of  $\text{Ca}^{40}$  and  $\text{K}^{39}$  should be well described by a single-particle wavefunction. The first excited state of  $\text{K}^{39}$  is  $\sim 2\frac{1}{2}$  MeV above the ground state, and so cross-sections to the ground state of  $\text{K}^{39}$  could be readily obtained. Good  $(\gamma, p)$  data at a medium to high energy does not exist for  $\text{Ca}^{40}$ . A further attraction is that the  $\text{Ca}^{40} (e, e'p)$  reaction has been studied experimentally, and so  $(\gamma, p)$  and  $(e, e'p)$  momentum distributions could be compared.

A good nucleus for the investigation of meson exchange current and nucleon isobar contributions is the deuteron, in which these contributions can be evaluated most easily. The effects of such contributions have recently been evaluated<sup>89,90</sup>). However, existing data is not accurate enough for comparison. With a new counter ladder, much more accurate data could be acquired at Glasgow. At present a substantial contribution to the overall possible systematic error in the Glasgow  $(\gamma, p)$  measurements is the error in the absolute efficiency of the counters, and because pulse-height spectra from the counters must be accumulated and the background subtracted the evaluation of the area of a small proton peak is uncertain. This limits the present experimental system at high energies and backward angles where the count rate is low. A coincidence counter system consisting of thin overlapping pieces of scintillator would remove most of these objections. Development of such a system is currently in progress.

Finally/.....

Finally, it would be of interest to extend the present shell model calculation to include spin-orbit coupling and a non-local potential. Also further investigation of the Jastrow correlation factors used in  $(\chi, \rho)$  calculations would be worthwhile. The Jastrow formalism is intuitively pleasing and corresponds to definite physical pictures. Properties of the correlation function such as the shape, wound volume, etc. could be systematically varied to determine their effects on cross-section predictions and momentum distributions.

The  $\alpha$ -calibration is the procedure which is the primary calibration of the magnetic spectrometer and subsequently of the entire experimental system and which determines the dispersion across the focal plane of the spectrometer thereby giving the momenta at each counter in the counter ladder in the focal plane relative to the momentum on the central orbit.

A  $\text{Pu}^{238}$   $\alpha$ -source is mounted in the target ladder at the centre of the scattering chamber which is vacuum coupled to the spectrometer.  $\alpha$ -particles from the source, acting as the object for the spectrometer, are focused on to the counters, which are covered in thin aluminium foil, as described in section 2.8, with slits cut to define the centres of the counters. The data are the spectrometer fields, measured by the gaussmeter, at which the 5.499 MeV line of the  $\alpha$ -source appears in each counter. Thus for the ten counters  $J = 0$  to 9, ten different fields  $R(p_\alpha, J)$  are obtained at which charged particles of magnetic rigidity  $p_\alpha = 101.27 \text{ MeV}/c$  are focused on to counter  $J$ .

For a given spectrometer field  $R$  it is assumed that the magnetic rigidity  $p_J$  of charged particles seen by counter  $J$  is related to the momentum  $\bar{p}$  on the central orbit (corresponding to counter  $J = \frac{1}{2}$ ) by the relation

$$p_J = F(J) \bar{p}(R) \quad . \quad \text{A1.1}$$

$F(J)$  is assumed to be independent of field, which is equivalent to the assumption of a field distribution in the spectrometer independent of the absolute value of the magnetic field. This assumption will be reasonable until the magnetic field is such that the iron approaches saturation. Only two of the field  $R$ , momentum  $p$  and counter  $J$  are independent, i.e. there is some function  $f$  such that

$$f(p, R, J) = 0 \quad .$$

The reciprocity theorem may therefore be used:

$$\left(\frac{\partial p}{\partial R}\right)_J \left(\frac{\partial R}{\partial J}\right)_p \left(\frac{\partial J}{\partial p}\right)_R = -1 \quad \text{Al.2}$$

The  $\alpha$ -calibration data gives  $\left(\frac{\partial R(p_\alpha, J)}{\partial J}\right)_p$ . Using eq. Al.1 in eq. Al.2, eq. Al.2 may be written

$$\frac{dF}{dJ} = \frac{-1}{p_\alpha} \left(\frac{\partial p}{\partial R}\right)_J \left(\frac{\partial R}{\partial J}\right)_p \quad \text{Al.3}$$

Assuming that the gaussmeter readings are linearly related to the spectrometer field and that the field distribution is constant

$$\left(\frac{\partial p}{\partial R}\right)_J = \text{constant} = \frac{p_\alpha}{R(p_\alpha, J)}$$

Then eq. Al.3 becomes

$$\frac{d}{dJ} (F(J)) = \frac{-1}{R(p_\alpha, J)} \left(\frac{\partial R(p_\alpha, J)}{\partial J}\right)_p \quad \text{Al.4}$$

where both factors are given by the data.  $F(J)$  is then obtained from

$$F(J) = \int \frac{dF}{dJ} dJ + \text{constant} \quad \text{Al.5}$$

the constant being chosen such that  $F(4\frac{1}{2}) \equiv 1$ .

The function  $F(J)$  is shown in Fig. Al.1.

RELATIVE MOMENTA (F(J)) FOR EACH  
COUNTER (J) IN COUNTER LADDER

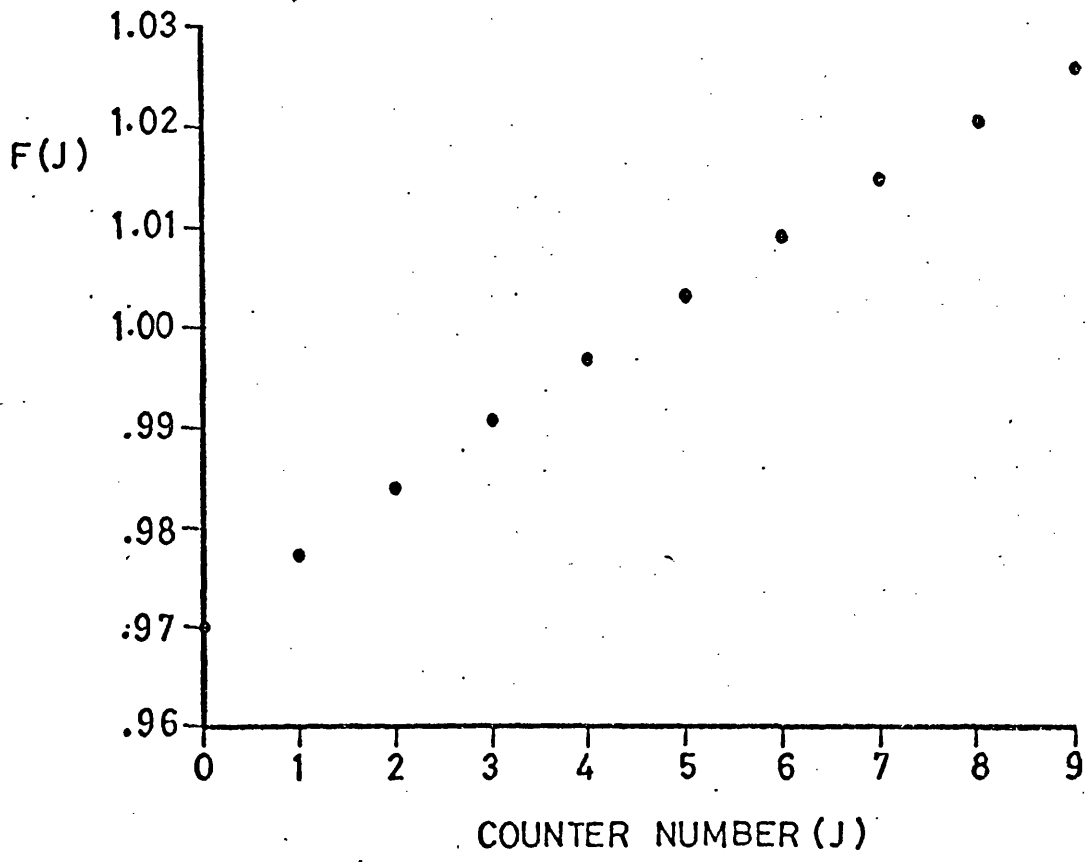


FIG. A1.1       $F = F(J)$

J	F(J)
0	.9696
1	.9772
2	.9839
3	.9905
4	.9968
5	1.0032
6	1.0092
7	1.0148
8	1.0205
9	1.0258

The resonant frequency of the IER oscillator measuring the magnetic field in the first bending magnet is used to measure the momentum of the electrons in the electron beam produced by the energy analysis system. It is assumed that the field is uniform and linearly related to the IER frequency because the magnet is operated well away from saturation (the maximum magnetic field is  $\sim 5500$  gauss) and because the gap is narrow compared with the dimensions of the poles. The calibration consists of finding the electron momentum corresponding to a given IER frequency and forming their quotient to give the IER calibration constant. Electrons of energy  $\sim 100$  MeV are used because their magnetic rigidity is almost that of the  $5.499$  MeV  $\alpha$ -particles used in the  $\alpha$ -calibration.

The energy analysis system is set to produce electrons of energy  $\sim 100$  MeV analysed to  $.1\%$ . These electrons were scattered from a thin aluminium foil in the scattering chamber and detected by the spectrometer at a field  $R_{100}$  in one of the two central counters in the focal plane nearest the central orbit. Let the IER frequency corresponding to these electrons be  $f^{\text{IER}}(R_{100})$ . The field  $R_{100}$  is very near to the field  $R_{\alpha}$  at which the  $\alpha$ -particles of magnetic rigidity  $p_{\alpha}$  from the  $\alpha$ -calibration source are detected in the same counter. If the details of the function  $f^{\text{IER}}(R)$  giving the IER frequency  $f^{\text{IER}}$  as a function of spectrometer field  $R$  are known for  $R \approx R_{\alpha}$ , then this provides the IER frequency  $f^{\text{IER}}(R_{\alpha})$  corresponding to an electron of momentum  $p_{\alpha}$  in the spectrometer or  $p'_{\alpha}$  in the bending magnet, where  $p'_{\alpha}$  is obtained from  $p_{\alpha}$  by considering the electron energy losses in the scattering chamber window, the spectrometer window and the air gap between them and the nuclear recoil correction.

The details of  $f^{\text{IER}}(R)$  are obtained by also measuring the fields  $R_{60}$  and  $R_{80}$  at which similarly scattered electrons of energies  $\sim 60$  and  $\sim 80$  MeV are detected by the spectrometer and fitting a quadratic through the three

points  $f^{IRR}(R_{60})$ ,  $R_{60}$ ,  $f^{IRR}(R_{80})$ ,  $R_{80}$  and  $f^{IRR}(R_{100})$ ,  $R_{100}$ .

The value of the calibration constant was found to be

$$233.39 \pm .04 \text{ kc/s / MeV/e .}$$

This calibration gives the magnetic rigidity on the central orbit  $\bar{p}$  as a function of the magnetic field  $R$  as measured by the gaussmeter.

The spectrometer energy calibration presumes the energy analysis system to have been previously been calibrated (Appendix 2.) The spectrometer calibration is determined by observing the endpoints of proton yield spectra produced from a thin photonuclear target by a reaction of known  $Q$ -value using bremsstrahlung from a thin radiator with primary electrons of known energy and small energy spread. A thin carbon (graphite) target (.006") was used, the radiator was  $\sim .015$  radiation lengths of gold, and the primary electrons from the accelerator were energy analysed to .5%. Experimentally observed proton yield spectra at various different endpoint energies spanning the required energy range are compared with proton yield spectra calculated assuming a linear spectrometer calibration based on the  $\alpha$ -calibration point (Appendix 1.) Matching the calculated spectra (involving the spectrometer field  $R$ ) with the experimentally observed spectra (involving the proton energy and hence momentum  $\bar{p}$ ) gives points on the calibration curve  $\bar{p} = \bar{p}(R)$  which may then be fitted by a polynomial in  $R$ . Also included were four lower momentum points, the  $\alpha$ -calibration point and the three elastic electron scattering points (Appendix 2.)

A thin photonuclear target, thin bremsstrahlung radiator and small energy spread are necessary to make the proton spectrum near the endpoint as sharp as possible. The proton spectrum was calculated with the assumption that the protons from the  $C^{12}(\gamma, p)B^{11}$  reaction left  $B^{11}$  in its ground state. Since the first excited state of  $B^{11}$  is 2.12 MeV above the ground state, it is the last 2 MeV or so of the spectra which should be matched. In fact it was not possible to distinguish the contributions from the excited states in the experimental spectra, and so the matching was performed near the endpoint. Small errors in matching ( $\leq \frac{1}{4}$  MeV) are

not important because provision is made for possible small errors in the spectrometer calibration when analysing data as discussed in section 3.6.

The polynomial fitted and thereafter used as the calibration curve was a quartic with a zero constant term

$$\bar{p} = a_1 R + a_2 R^2 + a_3 R^3 + a_4 R^4$$

where  $a_1 = 5.3096 \times 10^{-2}$   
 $a_2 = -3.6601 \times 10^{-7}$   
 $a_3 = -1.7053 \times 10^{-13}$   
 $a_4 = 1.3319 \times 10^{-14}$

and where  $R = \frac{\text{spectrometer field in gauss}}{2}$

The momentum  $p_J$  at each counter  $J$  for a given field  $R$  is assumed to be given by eq. A1.1

$$p_J = F(J) \bar{p}(R)$$

where  $F(J)$  gives the dispersion across the focal plane and is obtained from the  $\alpha$ -calibration.

The nonlinearity at high fields,  $\sim 4\%$  at 375 MeV/c, shows that some of the iron is definitely beginning to saturate; this is certainly true near the the gaussmeter probe at the outer edges of the poles. Therefore the dispersion at these high fields may no longer be that given by the  $\alpha$ -calibration ( $\sim 100$  MeV/c.)

Let the number spectrum as a function of momentum  $p$  differential in momentum  $p$  and solid angle  $\Omega$  of protons about to enter the spectrometer be  $\frac{d^2N}{dp d\Omega}$ . For counters 4 and 5, the two counters nearest the central orbit in the focal plane of the spectrometer, the solid angle of acceptance is the geometrical solid angle  $\Delta\Omega$  subtended at the object (the photonuclear target) by the collimator at the entrance window of the spectrometer (see section 2.7.) The momentum bite of either of the two central counters (counter numbers  $J = 4, 5$ ) is

$$\Delta p_J = \frac{dp_J}{dJ} \Delta J = \bar{p} \frac{dF}{dJ}(J) \Delta J \quad A4.1$$

using eq. A4.1 where  $\bar{p}$  is the momentum on the central orbit,  $\Delta J$  is the width of the counter in counter number space and  $\frac{dF}{dJ}(J)$  is given by the  $\alpha$ -calibration (eq. A1.4.) The absolute efficiency of a counter is  $\eta$ ; this is treated in Appendix 6. Then the number of counts  $C_J(\bar{p})$  seen by counter  $J = 4, 5$  for a spectrometer field corresponding to a momentum  $\bar{p}$  on the central orbit is

$$C_J(\bar{p}) = \frac{d^2N}{dp d\Omega} \bar{p} \frac{dF}{dJ}(J) \Delta J \Delta\Omega \eta(p_J) \quad A4.2$$

It is more convenient to write this in terms of energy than momentum. Using

$$\frac{d^2N}{dp d\Omega} = \frac{d^2N}{dE d\Omega} \frac{dE}{dp}, \quad p^2 = E^2 + 2mE, \quad \frac{dE}{dp} = \frac{p}{E+m} \quad \text{and} \quad p = F(J)\bar{p},$$

$$C_J = \frac{d^2N}{dE d\Omega} 2\bar{E} \frac{1 + \frac{\bar{E}}{2m}}{1 + \frac{\bar{E}}{m}} F(J) \frac{dF}{dJ}(J) \Delta J \Delta\Omega \eta(E), \quad J = 4, 5 \quad A4.3$$

For non-central counters these factors have different values;  $\Delta\Omega$  varies across the focal plane because the magnification varies and because the field deviates from the theoretical shape near the edges,  $\Delta p$  varies because the dispersion across the focal plane is not constant, and  $\eta$  varies because the proton momentum or energy changes continuously across the focal plane. Instead of trying to calculate these effects, they are all collected into

a single factor  $r_J$ , the relative efficiency of counter J, and this is directly measured (see Appendix 5.) The relative efficiencies  $r_J$ ,  $J = 0$  to 9, are defined such that the relative efficiency of a counter on the central orbit, counter  $J = 4\frac{1}{2}$ , is unity, i.e.  $r_{4\frac{1}{2}} \equiv 1$ . The relative efficiencies are energy-dependent, i.e.  $r_J = r_J(\bar{E})$ . So for any counter J

$$c_J = \frac{d^3N}{dE d\Omega} \bar{E} \frac{1 + \frac{\bar{E}}{\partial m}}{1 + \frac{\bar{E}}{m}} \left( 2 \Delta\Omega \frac{dF}{dJ}(J) F(J) \Delta J \right)_{J=4\frac{1}{2}} \eta(\bar{E}) r_J(\bar{E}) \quad A4.4$$

Writing  $\bar{E} = \left( 2 \Delta\Omega \frac{dF}{dJ}(J) F(J) \Delta J \right)_{J=4\frac{1}{2}}$

$$c_J = \frac{d^3N}{dE d\Omega} \bar{E} \frac{1 + \frac{\bar{E}}{\partial m}}{1 + \frac{\bar{E}}{m}} \bar{E} \eta(\bar{E}) r_J(\bar{E}) \quad A4.5$$

$\Delta\Omega = 9.94$  milliradians (section 2.7),  $\left( \frac{dF}{dJ} \right)_{J=4\frac{1}{2}} = .00648$  (Appendix 1),

$(F(J))_{J=4\frac{1}{2}} \equiv 1$ , and  $\Delta J = \frac{3}{4}$  (section 2.8.)

In terms of the cross-section  $\frac{d\sigma}{d\Omega}(\theta_p, E_\gamma)$  for the  $(\gamma, p)$  reaction to a particular state in the residual nucleus and the spectrum  $\frac{dN_\gamma}{dE_\gamma}(E_\gamma)$  of photons incident on the photonuclear target, the proton yield spectrum from the target is

$$\frac{d^3N_p}{dE_p d\Omega} = \frac{N_A}{A} n_e \times \frac{dN_\gamma}{dE_\gamma} \frac{dE_\gamma}{dE_p} \frac{d\sigma}{d\Omega} \quad A4.6$$

where  $N_A$  is Avogadro's number, A is the atomic weight of the photonuclear target,  $n_e$  is the number of electrons incident on the radiator and x is the target thickness. Let

$$s(E_\gamma, E_\gamma) \frac{d\sigma}{d\Omega}(E_{\gamma_0}) = \frac{d\sigma}{d\Omega}(E_\gamma)$$

where  $\frac{d\sigma}{d\Omega}(E_{\gamma_0})$  is the cross-section at a photon energy  $E_{\gamma_0}$  and  $s(E_\gamma, E_{\gamma_0})$  is the energy dependence of the cross-section. Then

$$\frac{d^3N_p}{dE_p d\Omega} = \left( \frac{N_A}{A} n_e \times \frac{d\sigma}{d\Omega}(E_{\gamma_0}) \right) \left( s \frac{dN_\gamma}{dE_\gamma} \frac{dE_\gamma}{dE_p} \right) \quad A4.7$$

Equations A4.5 and A4.7 together relate the number of counts in each counter  $C_J$  to the cross-section  $\frac{d\sigma}{d\Omega}(E_{\gamma_0})$  through the proton spectrum  $\frac{d^2N}{dE_d\Omega}$ . The relationship is quantified by fitting the experimental proton spectrum with its calculated shape. Let

$$\frac{dG}{dE_p}(\theta_p, E_p) = \frac{C_J(\theta_p, E_p)}{\bar{E} \frac{1 + \frac{\bar{E}}{2m}}{1 + E/m} \nu_J(\bar{E}) \eta(\bar{E})} \quad \text{A4.8}$$

This is a quantity proportional to the experimental proton spectrum in eq. A4.5. Let

$$\frac{dH}{dE_p}(\theta_p, E_p) = s \frac{dN_{\gamma}}{dE_{\gamma}} \frac{dE_{\gamma}}{dE_p} \quad \text{A4.9}$$

This is the quantity defining the shape of the proton spectrum in terms of the incident photon spectrum and the energy dependence of the cross-section (see eq. A4.7.) Fitting the experimental proton spectrum with the calculated spectrum shape establishes the quantity

$$a = \frac{\frac{dG}{dE_p}}{\frac{dH}{dE_p}}$$

$a$  is a number proportional to the cross-section to the particular state being considered (see sections 3.5, 3.6.) The absolute cross-section at  $E_{\gamma_0}$  is then given by

$$\frac{d\sigma}{d\Omega} = \frac{A}{\bar{E} N_A n_e x} a \quad \text{A4.10}$$

The relative efficiencies  $r_J$  of the counters  $J = 0$  to  $9$  are effectively obtained by examining the same proton spectrum with each counter in turn and requiring the detected spectra to be identical.

A smooth proton yield spectrum (ideally energy independent) from a suitable photonuclear target is examined at  $K$  different spectrometer field settings each separated by an amount small compared with the span of the counter ladder (Fig. A5.1a.) Since there are ten counters in the ladder, ten points of the spectrum for each field setting are obtained. All the 10N points should lie on the same smooth curve, but in fact they do not because of the different relative efficiencies of the counters. The situation is as shown in Fig. A5.1b, where the  $J^{\text{th}}$  counter's measurement of the proton yield spectrum is shifted vertically from the  $K^{\text{th}}$  counter's measurement by  $\ln(r_J) - \ln(r_K)$ .

Starting from eq. A4.5, the equation giving the number of counts in counter  $J$  in terms of the proton spectrum, and taking logarithms

$$\ln \left( \frac{c_J}{\bar{E} \frac{1 + \frac{\bar{E}}{2m}}{1 + \frac{\bar{E}}{m}} \eta(\bar{E})} \right) = \ln \left( \frac{d^2N}{dE d\Omega} \right) + \ln(r_J) + \text{constant}$$

At a given spectrometer field setting, i.e. at a given  $\bar{E}$ , the energy on the central orbit, only  $r_J$  varies as  $J$  varies on the right hand side of this equation. The relative efficiencies  $r_J$  are found by requiring all 10N points

$$y_{j+10J} = \ln \left( \frac{c_{jJ}}{\bar{E}_j \frac{1 + \frac{\bar{E}_j}{2m}}{1 + \frac{\bar{E}_j}{m}} \eta(\bar{E}_j)} \right)$$

$J = 0, 9$  (counter index)  
 $j = 1, N$  (spectrometer field setting index)  
 $E_{jJ}$  = energy of proton seen by counter  $J$  at field setting  $j$

to lie on the same smooth curve parametrised by a polynomial of degree  $L$ ,

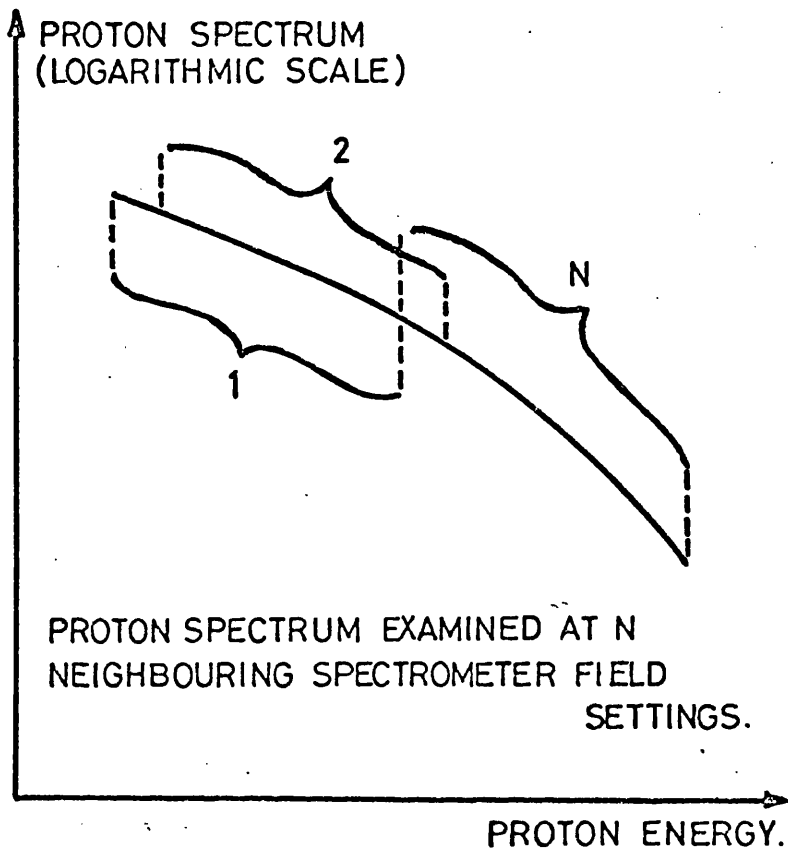


FIG. A5.1a

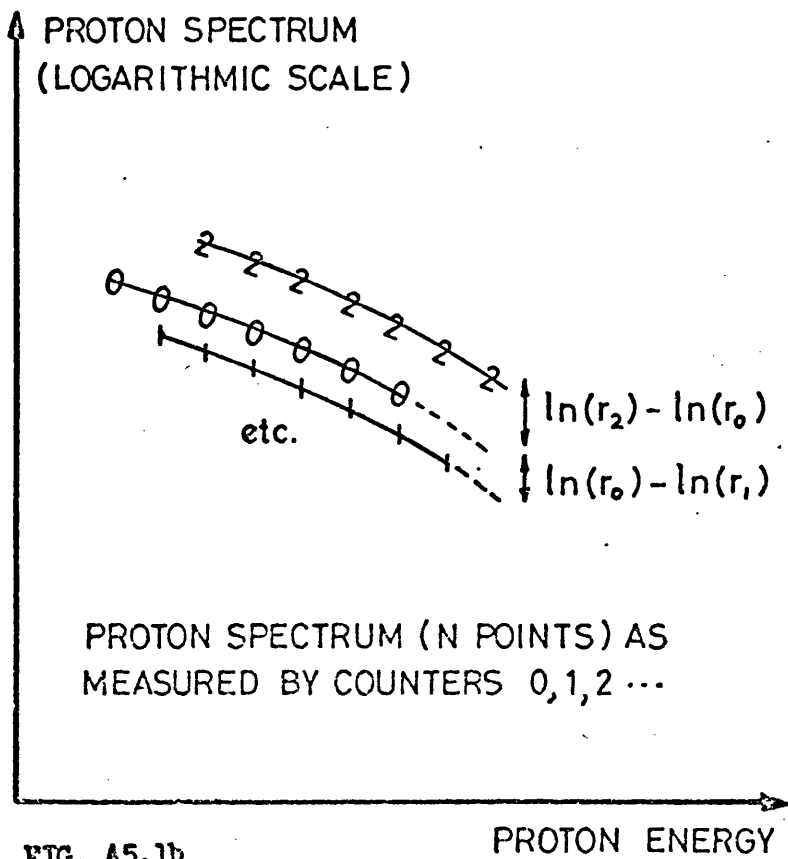


FIG. A5.1b

a demand met by minimising the quantity

$$\sum_{i=1}^{10N} \left( \frac{\sum_{k=0}^{q+L} a_k \phi_k(\epsilon_i) - y_i}{\sigma_i} \right)^2$$

$\sigma_i = \text{error in } y_i$   
 $\phi_k(E_j + 10J) = \begin{cases} \delta_{jk} & k = 0, 9 \\ E_{jJ}^{k-9} & k = 10, 9+L \end{cases}$

This procedure is just fitting the polynomial

$$c_0 + c_1 E + c_2 E^2 + \dots + c_L E^L$$

to all the points with a different constant  $c_0$  for each counter which gives its relative efficiency. The coefficients  $a_k$  produced by the minimisation are

$$a_J = \ln(r_J) + \text{constant} \quad J = 0, 9$$

$$a_{9+k} = \text{coefficient of } E^k \text{ in the polynomial}$$

The relative efficiency of counter  $J$  with respect to a counter on the central orbit (counter  $4\frac{1}{2}$ ) is given by

$$r_J = \frac{e^{a_J}}{\frac{1}{2} (e^{a_4} + e^{a_5})}$$

The errors in  $r_J$  are obtained from the correlated errors in the  $a_J$ .

The relative efficiencies of the counters were measured at six different proton energies or spectrometer fields. A graph is presented as Fig. A5.2. The general slope downwards with increasing  $J$  for counters near the centre of the ladder reflects the varying energy bite across the focal plane. The droops at the ends of the counter ladder reflects the reduction of the effective solid angle as particles hit the vacuum box of the spectrometer or encounter incorrect field distributions. The smaller variations are due to combinations of the effects of both these factors and the variation in dispersion. It is evident that the field distribution is worst at the highest fields.

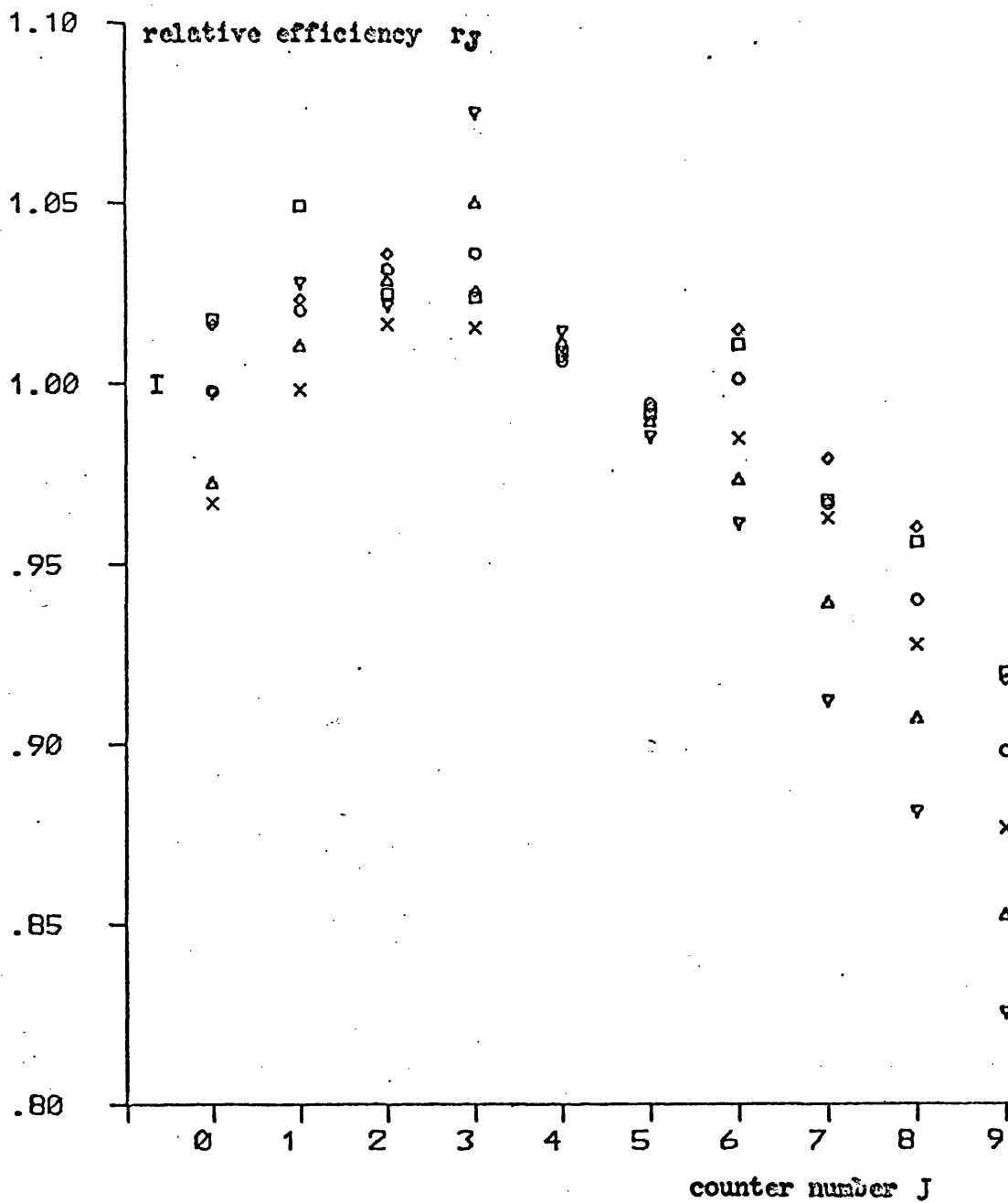


FIG. A5.2 RELATIVE EFFICIENCIES

- proton energy - 16 MeV
- ◇ 22 MeV
- 32 MeV
- x 45 MeV
- △ 59 MeV
- ▽ 71 MeV

The absolute efficiency of a counter relates the total number of protons incident on the counter to the area of the proton peak in the counter pulse height spectrum.

When monoenergetic protons are incident on a scintillation counter, the pulse height spectra with and without background are as shown in Fig. A6.1. The low energy tail is due to protons which have either scattered out of the side of the counter before depositing their full energy or suffered inelastic nuclear interactions. The relative proportions of these depend on the counter geometry. In the presence of background, the observed lower limit of the peak is defined by the energy resolution of the counter and is characterised by the quantity  $\epsilon$  as shown,  $\epsilon$  being expressed as a fraction of the full peak energy. (In the data analysis, the lower of the two channel numbers defining the "added" region which spans the peak is  $\epsilon$  (section 3.2.))

The multiple scattering loss was evaluated by calculating the mean square displacement  $\sqrt{\langle t^2 \rangle}$  <sup>36,42)</sup> of a proton from its plane of incidence after having passed through a thickness of scintillation material corresponding to production of a fraction  $\epsilon$  of the light <sup>43)</sup> produced from the full thickness. A proton incident on the counter within  $\sqrt{\langle t^2 \rangle}$  of the edge is considered to be lost. The multiple scattering loss is energy dependent and is most significant for protons which just stop in the counter. A useful approximation when calculating the mean square multiple scattering angle through a thick foil in which energy losses are significant is to use the thin foil formula with an energy equal to the geometric mean of the entry and exit energies. This assumes the stopping power  $\frac{dE}{dx}$  to be constant between entry and exit.

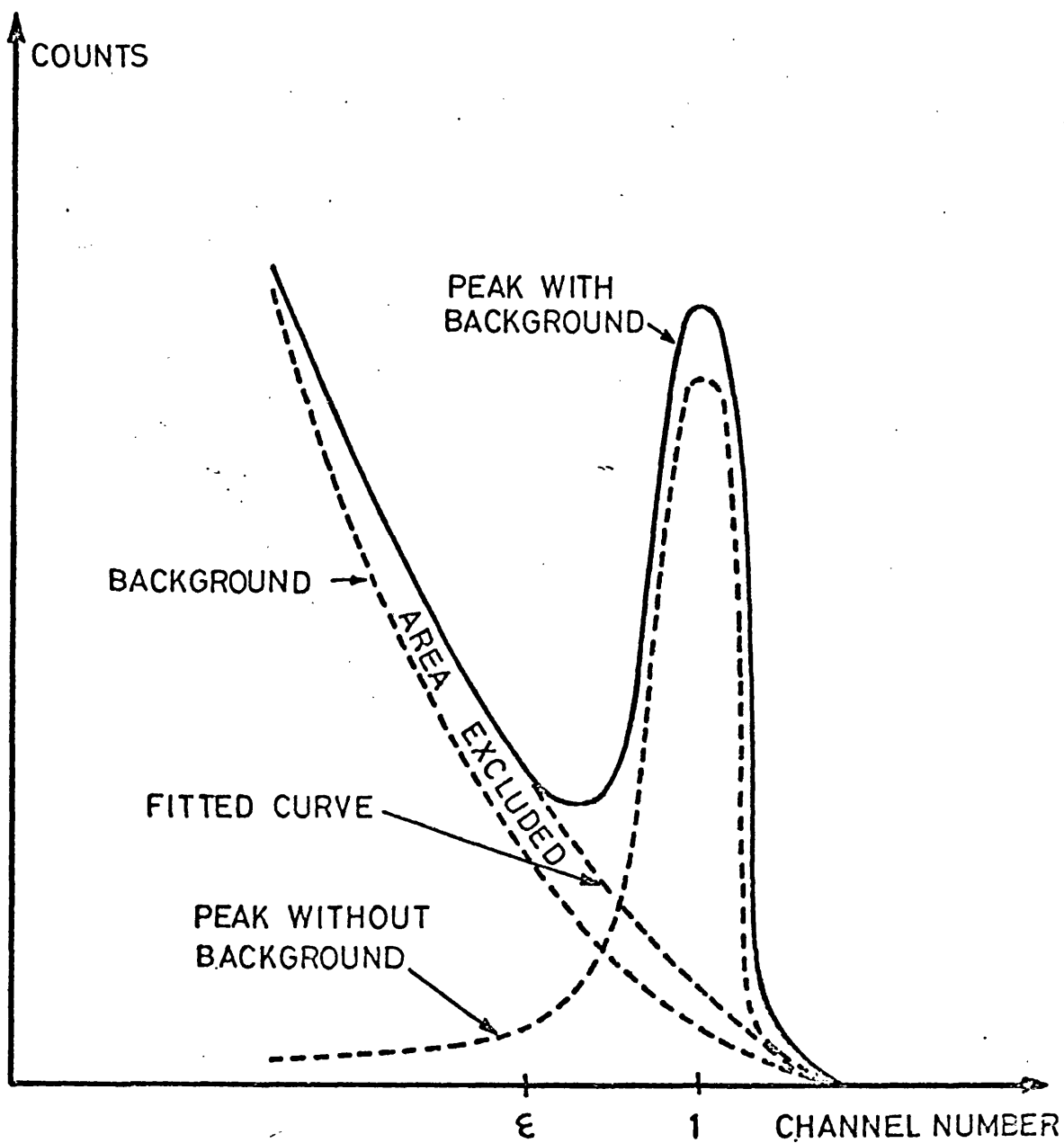


FIG. A6.1

Proton peak with background in  
pulse height spectrum

The inelastic nuclear interaction loss was calculated using the pulse height spectrum shapes as measured by Baker et al.<sup>44)</sup> and the theoretical predictions of Heasday and Richard-Serre<sup>45)</sup>. The experimental measurements used were obtained using a monoenergetic proton beam incident upon a large counter at its centre so there would be no multiple scattering losses as described above. If the lower limit of the peak is  $\epsilon$  then the protons excluded from the computed area are shown in Fig. A6.1. From the spectrum shape this area may be calculated. This loss is also energy dependent, the loss becoming more significant as the energy increases.

These two losses obviously depend on  $\epsilon$ , and  $\epsilon \approx .8$  for the counter pulse height spectra analysed. The two losses together make up the absolute efficiency  $\eta(E)$ . An error of 50%, including the error due to variation of  $\epsilon$ , was assigned to this correction. The absolute efficiency as a function of energy is shown in Fig. A6.2.

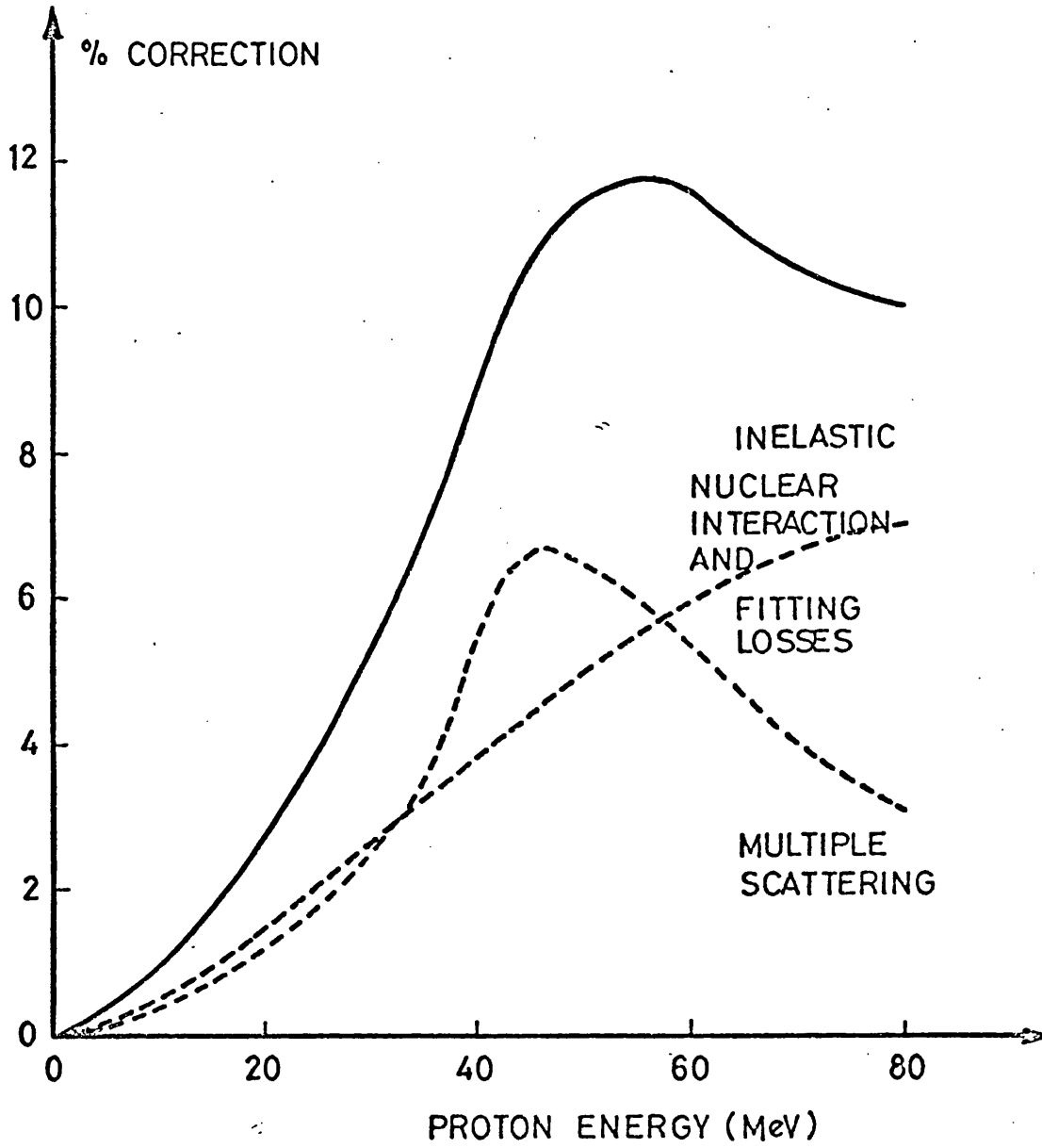


FIG. A5.2

Absolute efficiency of counter

The essence of the photon single difference technique<sup>20)</sup> is shown in Fig. A7.1. The difference of two appropriately chosen bremsstrahlung spectra has a peak and a low energy tail as shown. If the proton yield spectra from the photonuclear target for the two bremsstrahlung spectra are subtracted, then the resulting proton yield spectrum is due to the photon difference spectrum. An important feature of the photon single difference technique is the small (ideally zero) contribution by the virtual photons. This makes the use of a magnet to dump the electrons leaving only the photons unnecessary and allows the photonuclear target to be placed near the radiator thus intercepting the entire cone of photons emitted from the radiator.

A simplified illustration is shown in Fig. A7.2. A gross approximation to the basic bremsstrahlung spectrum from an infinitely thin radiator for monoenergetic primary electrons is shown in Fig. A7.2a. When energy losses in an actual radiator are considered, the resulting spectrum looks like that in Fig. A7.2b. The two radiator thicknesses and primary electron energies are then chosen such that the situation in Fig. A7.2c is reproduced. The difference spectrum is then as shown in Fig. A7.2d. From this it can be seen that radiators of the same material cannot be chosen for both bremsstrahlung spectra. It is obvious that the photon difference spectrum depends critically on the shape of the bremsstrahlung spectrum near the endpoint and on the details of the electron energy losses.

If there were no energy loss straggling in the radiators and if the analysed electron beam from the accelerator were of zero energy width, then the requirement of zero contribution by the virtual photons would be met by arranging the energies of electrons emerging from the two radiators to be equal (the situation shown, in fact, in Fig. A7.2.) This would give two identical virtual photon spectra which would cancel exactly. However,

INTENSITY : ( NO. OF PHOTONS / INCIDENT ELECTRON / MEV ) x PHOTON ENERGY

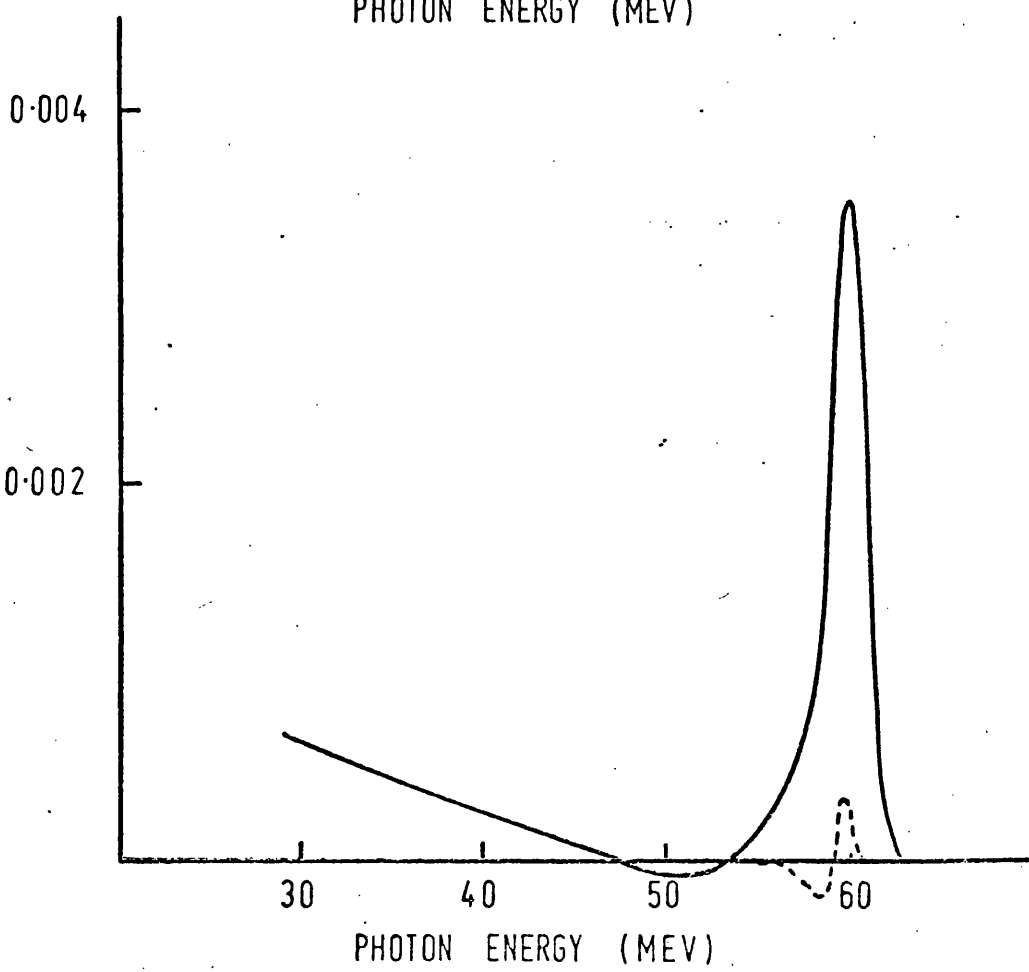
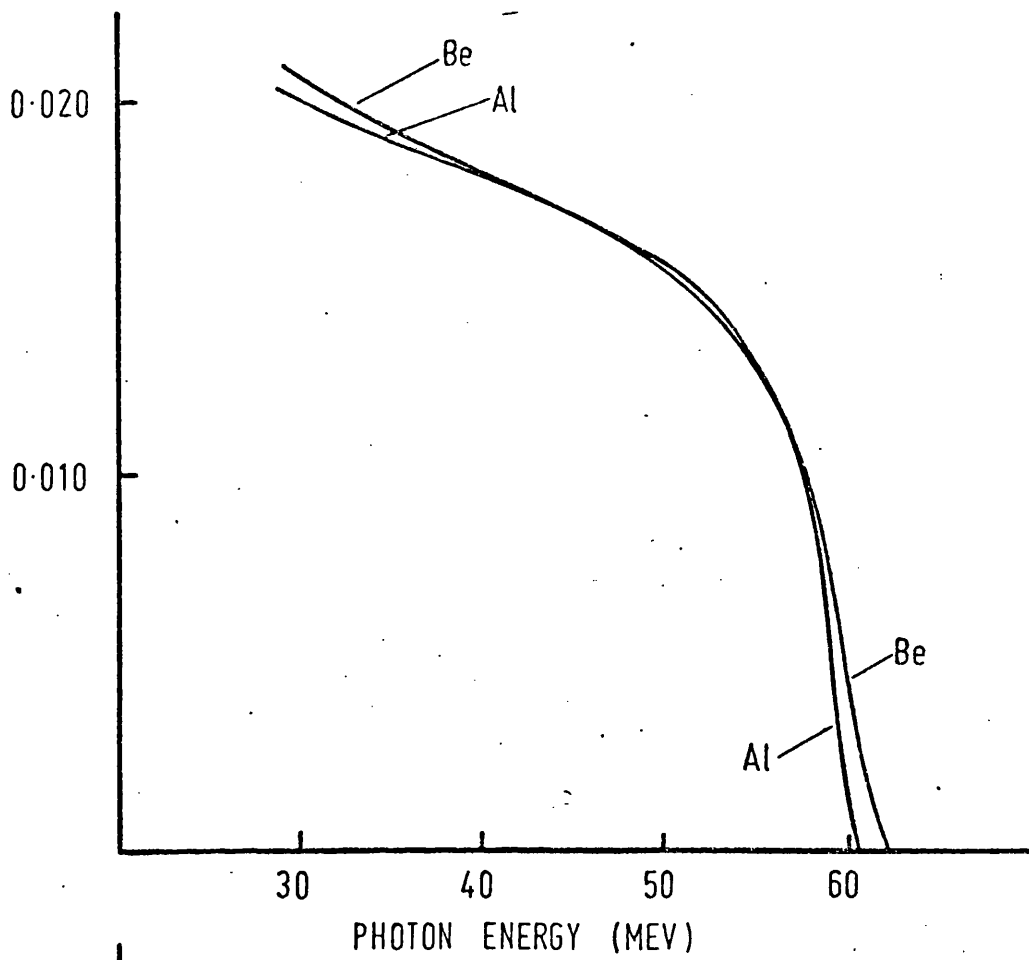


FIG. A7.1 PHOTON DIFFERENCE SPECTRUM  
( - - - - - VIRTUAL PHOTON SPECTRUM )

since there is energy loss straggling and since the electron beam is  $\sim \frac{1}{2}$  MeV wide, the two virtual photon spectra never cancel exactly. Conditions should thus be chosen such that the area of the virtual photon difference spectrum is small or zero.

The radiator materials, radiator thicknesses and primary electron energies are chosen by a long iterative procedure involving many compromises about the area and width of the photon peak, the magnitude of the low energy tail and the cancellation of the virtual photon spectrum. Low Z elements are desirable for the radiator material since for them the Coulomb correction<sup>30)</sup>, which is somewhat uncertain, is smallest; high Z materials have the largest bremsstrahlung cross-sections; the low energy tail should be fairly small; the peak should be narrow and have a large area; the virtual photon contribution should be small.

The materials chosen for the radiators are Be (the minuend) and Al (the subtrahend) of thicknesses 1.678 gm/cm<sup>2</sup> (.020 radiation lengths) and .578 gm/cm<sup>2</sup> (.022 radiation lengths) respectively. These are low Z metals of reasonable thermal conductivity and low chemical reactivity in air. The electron energy losses were taken from Sternheimer<sup>36,37)</sup>. The typical difference spectrum shown in Fig. A7.1 uses primary electron energies of 61.93 and 60.32 MeV analysed to .75%.

The calculated photon difference spectrum has been partially checked experimentally by the  $\text{Li}^7(\gamma, t)\text{He}^4$  reaction. The nucleus  $\text{He}^4$  has no excited state of excitation energy less than  $\sim 20$  MeV, and so over a large energy region down from the endpoint the reaction is two-body with the triton spectrum mirroring the photon spectrum. Since a triton has a third of the energy of a proton of the same magnetic rigidity, high energy tritons near the endpoint of the difference spectrum have not been detected because sufficiently high spectrometer fields cannot be obtained. However, tritons

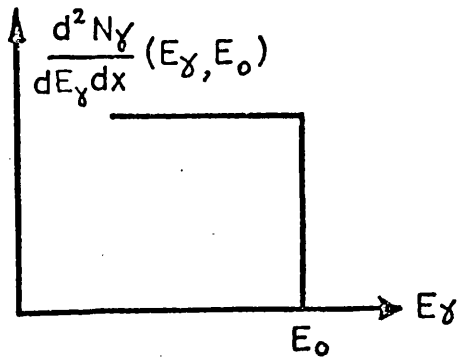


FIG. A7.2a

Bremsstrahlung spectrum from infinitely thin radiator (primary electron energy  $E_0$ )

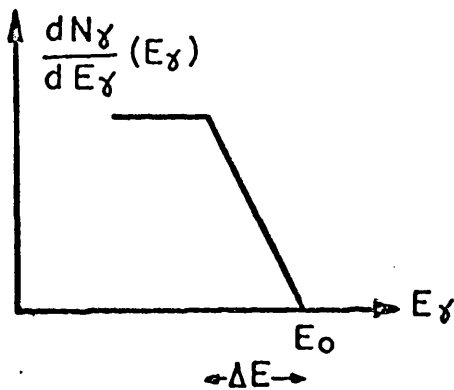


FIG. A7.2b

Bremsstrahlung spectrum from radiator of finite thickness ( $\Delta E$  = electron energy loss in radiator)

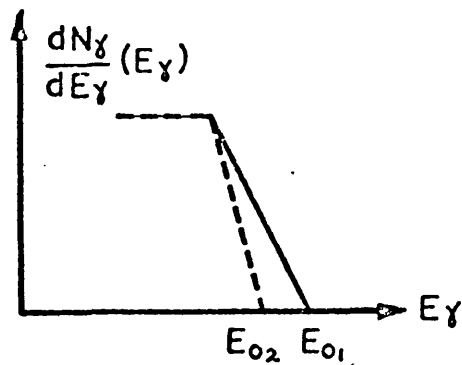


FIG. A7.2c

Two bremsstrahlung spectra from two different radiators

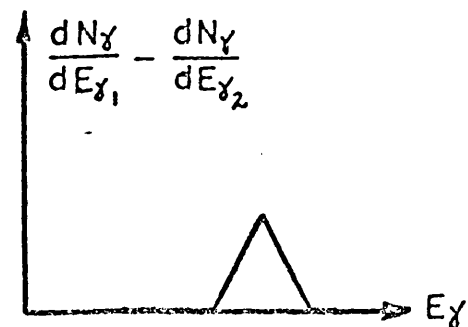


FIG. A7.2d

Difference spectrum

corresponding to photons below the peak in the difference spectrum have been seen, and these confirm the cancellation below the peak. Another check is the consistency of the  $C^{12}(\gamma, p)$  cross-sections measured both using the photon difference method and ordinary bremsstrahlung as discussed in section 4.1. A good way to check, but one which has not been done so far, would be to measure the proton yield spectrum from the two-body  $O^{16}(\gamma, p)N^{15}$  reaction by the photon difference method. Such a spectrum can be obtained for more than 5 MeV down from the endpoint, and should therefore cover all of the photon difference peak.

Let  $\frac{d^2N(E, E_0)}{dE dx}$  be the bremsstrahlung photon spectrum per unit radiator thickness and per primary electron as a function of photon energy  $E$  from an infinitely thin radiator for a primary electron energy  $E_0$ . Let  $s(E, t, E')$  be the energy loss distribution for electrons of energy  $E$  incident on an absorber of thickness  $t$  (the bremsstrahlung radiator,) and  $w(E_0, E)$  the distribution of incident electrons of nominal energy  $E_0$  (the energy-analysed beam from the accelerator.) Then, (after a procedure similar to that in Appendix 9,) the spectrum of photons from the bremsstrahlung radiator is

$$\frac{dN''(E'')}{dE''} = \int w(E_0, E) dE \int \frac{d^2N(E'', E')}{dE'' dx} \int s(E, x, E') dx$$

$w(E_0, E)$  is assumed to be a rectangle whose full-width is the width of the energy-defining slits in the analysis system.  $s(E, x, E')$ , the electron energy loss distribution, is the result of folding together the radiative and collision energy loss distributions in the radiator, and is given by

$$s(E, x, E') = \int s_1(E, x, E'') s_r(E'', x, E') dE''$$

where  $s_1(E, x, E')$  is the ionisation (collision) energy loss distribution and  $s_r(E, x, E')$  is the radiative energy loss distribution. This integration must be performed numerically.

While  $S(E, E') = \int s(E, x, E') dx$ , the integrated energy loss distribution, should be evaluated as a function of both  $E$  and  $E'$ , in fact when calculating it is evaluated once, for  $E = E_0$ , and then moved along the  $E$ -axis (with slight stretching or compressing) for other values of  $E$ . This avoids excessively lengthy calculations without introducing serious errors.

The proper evaluation of the above expressions is essential to obtain the correct shape of the bremsstrahlung spectrum near the endpoint. This is important for the photon single difference technique.

Suppose the spectrum of protons differential in energy and target thickness produced from an infinitely thin photonuclear target by a spectrum of photons is  $\frac{d^2N(E)}{dE dx}$  (number of protons per MeV per unit target thickness.) In the actual target, since it is of finite thickness, energy losses and straggling occur. The photonuclear target is therefore divided into elementary slices of thickness  $dx$ . Then  $\frac{d^2N(E)}{dE dx} dx$  is the number of protons at  $x + dx$  with energies between  $E$  and  $E + dE$  that originate in the slice of thickness  $dx$ . These protons must pass through the rest of the target. Let  $s(E_0, t, E)$  be the energy loss distribution for monoenergetic protons with energy  $E_0$  incident upon an absorber of thickness  $t$ , i.e.  $s(E_0, t, E)dE$  is the probability that a proton emerges from the absorber with an energy between  $E$  and  $E + dE$  if its initial energy is  $E_0$  (see Fig. A10.1.) (If there were no straggling,  $s$  would be a  $\delta$ -function.)

Then

$$\frac{d^2N(E)}{dE dx} dx s(E, T-x, E') dE' \quad , \quad T = \text{target thickness} \quad ,$$

is the number of protons emerging from the target with energies between  $E'$  and  $E' + dE'$  that are derived from the slice of thickness  $dx$  at position  $x$ . Integrating over  $E$  and  $x$ , the number of protons with energies between  $E'$  and  $E' + dE'$  coming from the entire target is

$$dN' = \int dE \int dx \frac{d^2N(E)}{dE dx} s(E, T-x, E') dE' \quad ,$$

and so the spectrum of protons emerging from the entire target is

$$\frac{dN'(E')}{dE'} = \int \frac{d^2N(E)}{dE dx} \int_0^T s(E, T-x, E') dx dE \quad .$$

Since the energy losses in the photonuclear target are very small compared with the energies of the protons involved (typically  $\sim \frac{1}{2}$  MeV for a 50 MeV proton passing through  $50 \text{ ng/cm}^2$ ) the energy loss distribution

$s(E, t, E')$  may be assumed to be a function only of the difference of  $E$  and  $E'$  (see Appendix 10.) This means that the integral over  $x$

$$\int_0^T s(E, T-x, E') dx$$

may be evaluated separately. Problems can arise if it is attempted to perform the integration numerically, because as  $T-x$  becomes very small the function  $s$  looks like a  $\delta$ -function. However,  $s$  may be approximated by a suitable function which can be integrated analytically. One such approximation (to the Landau straggling distribution) is the triangular distribution shown in Fig. A9.1.  $a$  is the most probable energy loss per unit thickness, and  $b$  and  $c$  are determined by requiring the upper and lower mean square half-widths to be those of the Landau distribution. The result of performing the integration

$$\int_0^T s(E, t, E') dt$$

for the triangular

distribution is given in Table A9.1.

for the triangular

$S(E,t,E')$

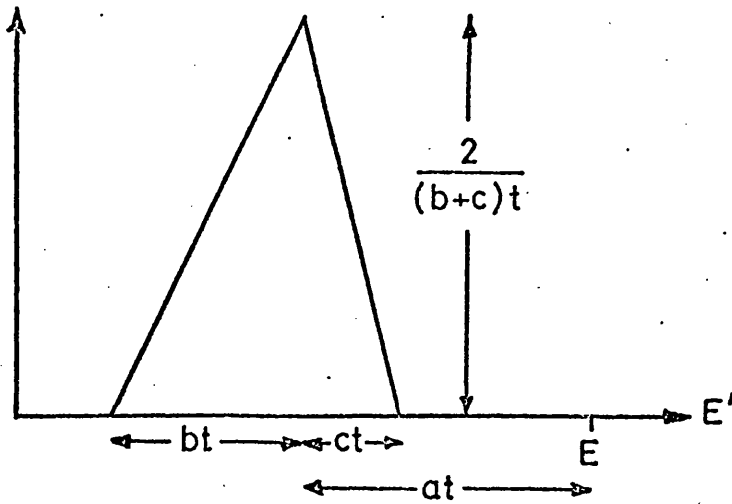


FIG. A9.1

$$I = \int_0^T s(E,t,E') dE'$$

1)  $E' < E - (a+c)T$

$I = 0$

2)  $E - (a+c)T < E' < E - aT$

$$I = \frac{2}{c} \frac{a+c}{b+c} \left( \frac{E-E'}{T} - 1 + \ln \frac{T}{E-E'} \frac{a+c}{a} \right)$$

3)  $E - aT < E' < E - (a-b)T$

$$I = \frac{2}{b} \frac{a-b}{b+c} \left( \frac{a}{a-b} - \frac{E-E'}{T} - \ln \frac{T}{E-E'} \frac{a}{a} \right) + \frac{2}{c} \frac{a+c}{b+c} \left( \frac{a}{a+c} - 1 + \ln \frac{a+c}{a} \right)$$

4)  $E' > E - (a-b)T$

$$I = \frac{2}{b} \frac{a-b}{b+c} \left( \frac{a}{a-b} - 1 + \ln \frac{a-b}{a} \right) + \frac{2}{c} \frac{a+c}{b+c} \left( \frac{a}{a+c} - 1 + \ln \frac{a+c}{a} \right)$$

Let there be a spectrum of particles  $\frac{dN}{dE}(E)$  differential in energy as a function of energy incident upon an absorber of thickness  $t$ , and let  $s(E, t, E')$  be the energy loss distribution in the absorber. Then (after a procedure similar to that in Appendix 9) the spectrum of particles  $\frac{dN'}{dE'}(E')$  after having passed through the absorber is

$$\frac{dN'}{dE'}(E') = \int \frac{dN}{dE}(E) s(E, t, E') dE .$$

$s$  is a function of the three independent variables  $E$ ,  $t$ , and  $E'$ , and, for given  $E$  and  $t$ , may resemble either of the two illustrations in Fig. A10.1.

If the shape of the straggling distribution is assumed to be constant,

$$s(E, t, E') = c(E - E'')$$

$$\text{where } E'' = E - \overline{\Delta E}$$

and  $\overline{\Delta E} = \overline{\Delta E}(E, t)$  is the mean energy loss in the absorber.

(This is assuming that as  $E$  changes the straggling function retains a fixed shape but slides along the  $E'$  axis to give the correct mean energy loss  $\overline{\Delta E}(E)$ .)

Then

$$\frac{dN'}{dE'}(E') = \int \frac{dN}{dE}(E) c(E' - E'') dE, \quad E'' = E - \overline{\Delta E} .$$

Change integration variable to  $E''$  :  $dE'' = dE - d(\overline{\Delta E}(E))$

$$\text{i.e. } dE'' = \left(1 - \frac{d\overline{\Delta E}}{dE}\right) dE .$$

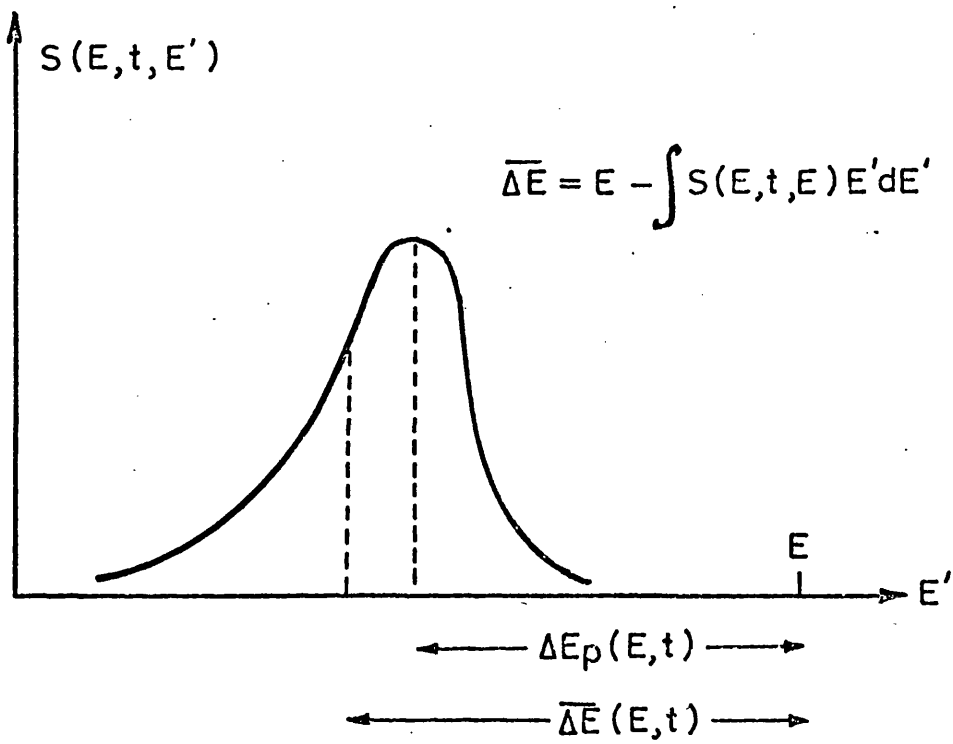
$\overline{\Delta E}$  is related to the stopping power  $\frac{dE}{dx}$  by the integral equation

$$t = \int_{E - \overline{\Delta E}}^E \frac{1}{\frac{dE}{dx}(E')} dE'$$

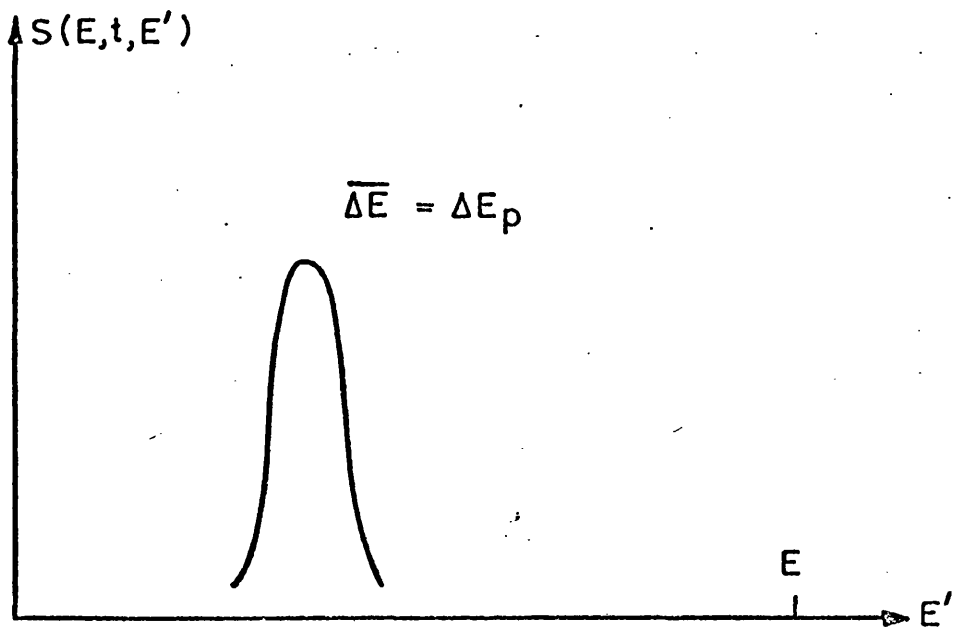
$$\text{i.e. } t = \int \frac{1}{\frac{dE}{dx}(E')} dE' - \int_{E - \overline{\Delta E}(E)} \frac{1}{\frac{dE}{dx}(E')} dE' .$$

Differentiate both sides with respect to  $E$  :

$$\frac{dt}{dE} = 0 = \frac{d}{dE} \int \frac{1}{\frac{dE}{dx}(E')} dE' - \frac{d(E - \overline{\Delta E})}{dE} \frac{d}{d(E - \overline{\Delta E})} \int_{E - \overline{\Delta E}} \frac{1}{\frac{dE}{dx}(E')} dE'$$



LANDAU STRAGGLING



GAUSSIAN STRAGGLING

Fig. A10.1

$$= \frac{1}{\frac{dE}{dx}(E)} - \left(1 - \frac{d\bar{\Delta E}}{dE}\right) \frac{1}{\frac{dE}{dx}(E - \bar{\Delta E})}$$

$$\text{i.e. } 1 - \frac{d\bar{\Delta E}}{dE} = \frac{\frac{dE}{dx}(E - \bar{\Delta E})}{\frac{dE}{dx}(E)}$$

$$\therefore dE'' = \frac{\frac{dE}{dx}(E - \bar{\Delta E})}{\frac{dE}{dx}(E)} \quad \text{or} \quad dE = \frac{\frac{dE}{dx}(E'' + \bar{\Delta E})}{\frac{dE}{dx}(E'')} dE''$$

$$\text{Therefore } \frac{dN'}{dE'}(E') = \int \frac{dN}{dE}(E'' + \bar{\Delta E}) \sigma(E - E'') \frac{\frac{dE}{dx}(E'' + \bar{\Delta E})}{\frac{dE}{dx}(E'')} dE''$$

If  $\sigma(E' - E'')$  is only significant for  $E'' \approx E'$ , then the equation may be rewritten

$$\frac{dN'}{dE'}(E') = \frac{\frac{dE}{dx}(E' + \bar{\Delta E})}{\frac{dE}{dx}(E')} \int \frac{dN}{dE}(E'' + \bar{\Delta E}) \sigma(E' - E'') dE''$$

The approximations made in this derivation are reasonable for Gaussian straggling (low energy, thick absorber) when the resultant spectrum is not required over a large energy range.

Neglecting straggling, the factor

$$\frac{\left[\frac{dE}{dx}\right]_{E = E_{\text{incident}}}}{\left[\frac{dE}{dx}\right]_{E = E_{\text{final}}}}$$

may be

simply derived using the reciprocity theorem. Suppose  $\Delta N$  particles, with energies between  $E$  and  $E + dE$ , are incident on an absorber, and after passing through the absorber they have energies between  $E'$  and  $E' + dE'$ . Then writing  $\frac{dN}{dE}$  for the incident spectrum of particles and  $\frac{dN'}{dE'}$  for the final spectrum

$$\Delta N = \frac{dN}{dE} dE = \frac{dN'}{dE'} dE' \quad \text{or} \quad \frac{dN'}{dE'} = \frac{dE}{dE'} \frac{dN}{dE}$$

Since there is no straggling, there is a unique relation between the incident energy  $E$ , the absorber thickness  $x$  and the final energy  $E'$ . The reciprocity theorem may therefore be used:

$$\left(\frac{\partial E}{\partial x}\right)_{E'} \left(\frac{\partial x}{\partial E'}\right)_E \left(\frac{\partial E'}{\partial E}\right)_x = -1$$

$$\therefore \frac{dE}{dE'} = \left(\frac{\partial E}{\partial E'}\right)_x = - \frac{\left(\frac{\partial E}{\partial x}\right)_{E'}}{\left(\frac{\partial E'}{\partial x}\right)_E} = \frac{\left[\frac{dE}{dx}\right]_{E = E_{\text{incident}}}}{\left[\frac{dE}{dx}\right]_{E = E_{\text{final}}}}$$

It should be noted that if the energy loss distribution function  $s(L, t, E')$  is assumed to be a function of  $E - E'$  and not of  $E$  and  $E'$  separately, then this is equivalent to

$$\frac{\left[\frac{dE}{dx}\right]_{E = E_{\text{incident}}}}{\left[\frac{dE}{dx}\right]_{E = E_{\text{final}}}} \equiv 1$$

The reaction is the photodisintegration of the A nucleon target nucleus to a proton and an A-1 nucleon residual nucleus. The A nucleons are considered as a proton and a core of A-1 nucleons. It is assumed that the photon only interacts with the proton, and that the internal wavefunction of the core does not change during the transition. The system is therefore treated as two particles, the proton and the core. The initial state (the target nucleus) is a bound state of the proton and the core, and the final state is a continuum state of the proton and the core (the residual nucleus.)

The process will be described in a coordinate system in which

$\vec{r}_p$  is the coordinate of the proton

$\vec{r}_c$  is the coordinate of the core

$\vec{K}_i$  is the momentum of the target nucleus (the centre-of-mass of the proton and the core in the initial state)

$\vec{K}_f$  is the momentum of the centre-of-mass of the proton and the residual nucleus (the proton and the core in the final state)

$\vec{k}_\gamma$  is the momentum of the photon.

Also let  $\vec{r}$  be the coordinate of the proton relative to the core

$\vec{R}$  be the coordinate of the centre-of-mass of the proton and the core

$\vec{k}$  be the momentum of the proton or the residual nucleus (the core in the final state) in their combined centre-of-mass frame

$m$  be the proton mass

$\hat{\epsilon}$  be the photon polarisation vector.

First-order time-dependent perturbation theory gives<sup>46)</sup> the transition rate between an initial state  $|i\rangle$  and a two-particle final state  $|f\rangle$  described by the parameters  $\nu_1, \nu_2$  with a density of final states  $\frac{d^2 N}{d\nu_1 d\nu_2}$  due to a perturbing Hamiltonian  $H_1$  as

$$\frac{dw}{dt} = \frac{2\pi}{\hbar} \iint |\langle f | H_1 | i \rangle|^2 \frac{d^2 N}{d\nu_1 d\nu_2} \delta(E_f - E_i) d\nu_1 d\nu_2$$

The initial state is  $\Psi_i = e^{i\mathbf{K}_i \cdot \mathbf{R}} \psi_i(\mathbf{r})$ ,

the final state is  $\Psi_f = e^{i\mathbf{K}_f \cdot \mathbf{R}} \psi_f(\mathbf{r}, \mathbf{r}_p)$ ,

the perturbing Hamiltonian  $H_1$  is the photon interaction operator<sup>34)</sup>

$$i \frac{e\hbar}{mc} \sqrt{\frac{2\pi\hbar c}{k_y}} \sum_{\mathbf{r}_p} e^{i\mathbf{k}_y \cdot \mathbf{r}_p} \cdot \nabla_{\mathbf{r}_p}$$

the parameters used to describe the final state will be taken to be  $\mathbf{K}_f, k$ ,

and  $\frac{d^3 N}{d\nu_1 d\nu_2} d\nu_1 d\nu_2 = \frac{1}{(2\pi)^6} d^3 \mathbf{K}_f k^2 dk d\Omega_k$ .

The cross-section is the transition rate per unit incident flux of photons:

$$\sigma = \frac{\partial n}{k c} \left( \frac{e\hbar}{mc} \right)^2 \frac{2\pi\hbar c}{k_y} \frac{1}{(2\pi)^6} \iint \left\{ \sum_{f_i} \left| \iint e^{i\mathbf{K}_f \cdot \mathbf{R}} \psi_f(\mathbf{r}, \mathbf{r}_p) \right|^2 \sum_{i_i} e^{i\mathbf{K}_i \cdot \mathbf{R}} \psi_i(\mathbf{r}) d^3 \mathbf{r}_p d^3 \mathbf{r}_c \right\} \delta(E_f - E_i) d^3 \mathbf{K}_f k^2 dk d\Omega_k$$

where  $\sum_{f_i}$  denotes the sum over the final and the average over the initial substates.

It is convenient to change from  $\mathbf{r}_p, \mathbf{r}_c$  to  $\mathbf{r}, \mathbf{R}$ :

$$\begin{aligned} \mathbf{r}_p &= \mathbf{r}_b - \mathbf{r}_c & \mathbf{r}_b &= \mathbf{R} + \frac{A-1}{A} \mathbf{r} \\ \mathbf{r}_c &= \frac{1}{A} \mathbf{r}_b + \frac{A-1}{A} \mathbf{r}_c & \mathbf{r}_c &= \mathbf{R} - \frac{1}{A} \mathbf{r} \\ d^3 \mathbf{r}_p d^3 \mathbf{r}_c &\longrightarrow \frac{\partial(\mathbf{r}_b, \mathbf{r}_c)}{\partial(\mathbf{r}, \mathbf{R})} d^3 \mathbf{r} d^3 \mathbf{R} = -d^3 \mathbf{r} d^3 \mathbf{R} \\ \nabla_{\mathbf{r}_p} &\longrightarrow \nabla_{\mathbf{r}} + \frac{1}{A} \nabla_{\mathbf{R}} \end{aligned}$$

Then  $\frac{d\sigma}{d\Omega_k} = F \iint \left\{ \sum \left| - \int e^{i\mathbf{K} \cdot \mathbf{R}} d^3 \mathbf{R} \left[ I_1 - \frac{i}{A} \frac{1}{\mathbf{r}} \cdot \mathbf{K}_i I_0 \right] \right|^2 \right\} \delta(E_f - E_i) d^3 \mathbf{K}_f k^2 dk$

where  $F = \frac{2\pi}{\hbar c} \left( \frac{e\hbar}{mc} \right)^2 \frac{2\pi\hbar c}{k_y} \frac{1}{(2\pi)^6}$ ,  $\kappa = k_x + k_i - k_f$ ,

$$I_1 = \int \psi_f^*(\underline{k}, \underline{z}) \underline{\hat{e}} e^{i \frac{A-1}{A} k_x \cdot \underline{z}} \cdot \nabla \psi_i(\underline{z}) d^3 z,$$

and  $I_2 = \int \psi_f^*(\underline{k}, \underline{z}) e^{i \frac{A-1}{A} k_x \cdot \underline{z}} \psi_i(\underline{z}) d^3 z,$

$$\begin{aligned} \text{i.e. } \frac{d\sigma}{d\Omega} &= F \iint e^{i\kappa \cdot \underline{R}'} d^3 R' \int e^{i\kappa \cdot \underline{R}''} d^3 R'' d^3 \underline{k}_f \left\{ \sum \left| I_1 - \frac{i}{A} \underline{\hat{e}} \cdot \underline{k}_i I_2 \right|^2 \right\} \\ &\quad \delta(E_f - E_i) k^2 dk \\ &= F \iiint e^{i\kappa \cdot (\underline{R}' + \underline{R}'')} d^3 \underline{k}_f d^3 R' d^3 R'' \left\{ \sum \left| I_1 - \frac{i}{A} \underline{\hat{e}} \cdot \underline{k}_i I_2 \right|^2 \right\} \\ &\quad \delta(E_f - E_i) k^2 \frac{dk}{dE_f} dE_f \\ &= F \iint (2\pi)^3 \delta(\underline{R}' + \underline{R}'') d^3 R' d^3 R'' \left\{ \sum \left| I_1 - \frac{i}{A} \underline{\hat{e}} \cdot \underline{k}_i I_2 \right|^2 \right\} \\ &\quad \delta(E_f - E_i) k^2 \frac{dk}{dE_f} dE_f \\ &= F (2\pi)^3 \int d^3 R'' \left\{ \sum \left| I_1 - \frac{i}{A} \underline{\hat{e}} \cdot \underline{k}_i I_2 \right|^2 \right\} \delta(E_f - E_i) k^2 \frac{dk}{dE_f} dE_f \\ &= F (2\pi)^3 \int \left\{ \sum \left| I_1 - \frac{i}{A} \underline{\hat{e}} \cdot \underline{k}_i I_2 \right|^2 \right\} \delta(E_f - E_i) k^2 \frac{dk}{dE_f} dE_f. \end{aligned}$$

The most useful coordinate system is the one in which the centre-of-mass of the final state is at rest ( $\underline{k}_f = 0$ .) This means  $\underline{k}_1 = -\underline{k}_2$ , and, since the polarisation vector of a real photon is perpendicular to its direction of propagation,  $\underline{\hat{e}} \cdot \underline{k}_1 = 0$ . In this system,  $E_f = \frac{\hbar^2 k^2}{2 \frac{A-1}{A} m}$ .

$$\begin{aligned} \frac{d\sigma}{d\Omega} &= F (2\pi)^3 \int \left\{ \sum \left| I_1 \right|^2 \right\} \delta(E_f - E_i) k^2 \frac{A-1}{\hbar^2 k} m dE_f \\ &= F (2\pi)^3 \left[ \left\{ \sum \left| I_1 \right|^2 \right\} k^2 \frac{A-1}{\hbar^2 k} \right]_{E_f = E_i} \end{aligned}$$

$$\therefore \frac{d\sigma}{d\Omega} = \frac{1}{2\pi} \frac{A-1}{A} \frac{e^2}{\hbar c} \frac{\hbar c k}{mc^2} \frac{1}{k_y} \sum \left| \int \psi_f^*(\underline{k}, \underline{z}) \underline{\hat{e}} e^{i \frac{A-1}{A} k_x \cdot \underline{z}} \cdot \nabla \psi_i(\underline{z}) d^3 z \right|^2,$$

$$\hbar k = \sqrt{\frac{A-1}{A} \left( 2m (\hbar c k_y - Q) + \frac{\hbar^2 c^2 b_y^2}{A} \right)}$$

electric term only - no spin

Let the initial state be  $\psi_i(\underline{r}) = R_{nl}(r) Y_{lm}(\hat{r})$  and the final state be  $\psi_f(\underline{r}) = e^{i\mathbf{k} \cdot \underline{r}}$  (a plane wave.) The matrix element to be evaluated is

$$\begin{aligned} H &= \int \left( e^{i\mathbf{k} \cdot \underline{r}} \right)^* \hat{\underline{e}} \cdot \underline{\nabla} e^{i \frac{A-1}{A} \mathbf{k} \cdot \underline{r}} \cdot \underline{\nabla} \psi(\underline{r}) d^3 \underline{r} \\ &= \hat{\underline{e}} \cdot \int e^{-i \left( \mathbf{k} - \frac{A-1}{A} \mathbf{k} \right) \cdot \underline{r}} \underline{\nabla} \psi(\underline{r}) d^3 \underline{r} \end{aligned}$$

where  $\psi(\underline{r})$  is the bound state wavefunction. Since  $d^3 \underline{r} = r^2 \sin \theta dr d\theta d\phi \rightarrow 0$  as  $r \rightarrow 0$  and  $\psi(\underline{r}) \rightarrow 0$  faster than  $\frac{1}{r^2}$  as  $r \rightarrow \infty$ ,  $\underline{\nabla}$  is hermitian.

$H$  may therefore be rewritten

$$\begin{aligned} H &= \hat{\underline{e}} \cdot \int \underline{\nabla} e^{-i \left( \mathbf{k} - \frac{A-1}{A} \mathbf{k} \right) \cdot \underline{r}} \psi(\underline{r}) d^3 \underline{r} \\ &= -i \hat{\underline{e}} \cdot \left( \mathbf{k} - \frac{A-1}{A} \mathbf{k} \right) \int e^{-i \left( \mathbf{k} - \frac{A-1}{A} \mathbf{k} \right) \cdot \underline{r}} \psi(\underline{r}) d^3 \underline{r} \end{aligned}$$

Since the polarisation of a photon is perpendicular to the direction of its propagation  $\hat{\underline{e}} \cdot \mathbf{k} = 0$

$$\begin{aligned} \therefore H &= -i \hat{\underline{e}} \cdot \frac{\mathbf{k}}{k} k (2\pi)^{3/2} \left( \frac{1}{(2\pi)^{3/2}} \int e^{-i \left( \mathbf{k} - \frac{A-1}{A} \mathbf{k} \right) \cdot \underline{r}} \psi(\underline{r}) d^3 \underline{r} \right) \\ &= -i \hat{\underline{e}} \cdot \frac{\mathbf{k}}{k} k (2\pi)^{3/2} \phi \left( \mathbf{k} - \frac{A-1}{A} \mathbf{k} \right) \end{aligned}$$

$\phi(\underline{q}) =$  Fourier transform of  $\psi(\underline{r})$  (Appendix 15.)

To form  $\sum_{f,i} |H|^2$  with the above wavefunctions, it is necessary to average over photon polarisations and initial state angular momentum projections

$$|H|^2 = (2\pi)^3 \left| \hat{\underline{e}} \cdot \frac{\mathbf{k}}{k} \right|^2 k^2 \left| \phi \left( \mathbf{k} - \frac{A-1}{A} \mathbf{k} \right) \right|^2$$

Let  $\hat{k} = (\sin\theta \cos\phi, \sin\theta \sin\phi, \cos\theta)$ , the direction of the outgoing proton,  
 and  $\hat{\epsilon} = (\cos\phi', \sin\phi', 0)$ , the direction of the photon polarisation vector,  
 where the z-axis is defined by  $\hat{z} = \hat{k}$

$$\hat{\epsilon} \cdot \hat{k} = \sin\theta (\cos\phi \cos\phi' + \sin\phi \sin\phi') = \sin\theta \cos(\phi - \phi')$$

$$\therefore |\hat{\epsilon} \cdot \hat{k}|^2 = \sin^2\theta \cos^2(\phi - \phi')$$

Averaging  $|\hat{\epsilon} \cdot \hat{k}|^2$  over photon polarisations is just averaging  $\cos^2(\phi - \phi')$  over  $\phi$

$$\overline{\cos^2(\phi - \phi')} = \frac{1}{2}$$

Averaging over initial angular momentum projections  $m$  is forming  $\frac{1}{2l+1} \sum_m$

$$\begin{aligned} \therefore \sum_{f_i} |H|^2 &= (2\pi)^3 \sin^2\theta \frac{1}{2} k^2 \frac{1}{2l+1} \sum_m \left| \phi \left( \frac{k}{2} - \frac{A-1}{A} \frac{k}{2} \gamma \right) \right|^2 \\ &= (2\pi)^3 \sin^2\theta \frac{1}{2} k^2 \frac{1}{4\pi} \left| Q_{nl} \left( \left| \frac{k}{2} - \frac{A-1}{A} \frac{k}{2} \gamma \right| \right) \right|^2 \quad (\text{Appendix 15}) \end{aligned}$$

$$\text{i.e. } \sum_{f_i} |H|^2 = \pi^2 \sin^2\theta k^2 \left| Q_{nl} \left( \left| \frac{k}{2} - \frac{A-1}{A} \frac{k}{2} \gamma \right| \right) \right|^2$$

$$\text{where } Q_{nl}(q) = \sqrt{\frac{2}{\pi}} \int j_l(qr) R_{nl}(r) r^2 dr$$

electric term only - no spin

The initial bound state is  $\psi_i(\underline{r}) = R_{nl}(r) Y_{lm}(\hat{r})$ .

The final continuum state is  $\psi_f(\underline{k}, \underline{r}) = 4\pi \sum_{l'} \sum_{m'} i^{l'} e^{-i\delta_{l'}} g_{l'}(kr) Y_{l'm'}^*(\hat{k}) Y_{l'm'}(\hat{r})$

$$g_{l'}(kr) Y_{l'm'}^*(\hat{k}) Y_{l'm'}(\hat{r}) \quad (\text{distorted wave.})$$

The operator  $\hat{\underline{e}} \cdot \hat{\underline{\nabla}} e^{i \frac{A-1}{A} \underline{k} \cdot \underline{r}} \cdot \hat{\underline{\nabla}}$  is expanded in multipoles:

$$\hat{\underline{e}} \cdot \hat{\underline{\nabla}} e^{i \frac{A-1}{A} \underline{k} \cdot \underline{r}} \cdot \hat{\underline{\nabla}} = \sqrt{4\pi} \sum_{\lambda} i^{\lambda} \sqrt{2\lambda+1} j_{\lambda}\left(\frac{A-1}{A} kr\right) Y_{\lambda 0}(\hat{k}) \hat{\underline{e}} \cdot \hat{\underline{\nabla}} \quad (\hat{k}_y = \hat{k}_z)$$

The matrix element  $\int \psi_f^*(\underline{k}, \underline{r}) \hat{\underline{e}} \cdot \hat{\underline{\nabla}} e^{i \frac{A-1}{A} \underline{k} \cdot \underline{r}} \cdot \hat{\underline{\nabla}} \psi_i(\underline{r}) d^3 \underline{r}$  is therefore

$$H = \int (4\pi \sum_{l'} \sum_{m'} i^{l'} e^{-i\delta_{l'}} g_{l'}(kr) Y_{l'm'}^*(\hat{k}) Y_{l'm'}(\hat{r}))^* \sqrt{4\pi} \sum_{\lambda} i^{\lambda} \sqrt{2\lambda+1} j_{\lambda}\left(\frac{A-1}{A} kr\right) Y_{\lambda 0}(\hat{k}) \hat{\underline{e}} \cdot \hat{\underline{\nabla}} (R_{nl}(r) Y_{lm}(\hat{r})) d^3 \underline{r}$$

Considering circularly polarised photons,  $\hat{\underline{e}} \cdot \hat{\underline{\nabla}} = \nabla_h$  where  $h = \pm 1$ .

Using the gradient formula (for this and other relations used herein, see refs. 47 and 48)

$$H = \int (4\pi)^{\frac{3}{2}} \sum_{l'} \sum_{m'} (i^{l'})^* (e^{-i\delta_{l'}})^* g_{l'}(kr) Y_{l'm'}^*(\hat{k}) Y_{l'm'}(\hat{r}) \sum_{\lambda} i^{\lambda} \sqrt{2\lambda+1} j_{\lambda}\left(\frac{A-1}{A} kr\right) Y_{\lambda 0}(\hat{k}) \left( \sqrt{l+1} (-1)^{l+m+h} \begin{pmatrix} l+1 & l & 1 \\ m+h & -m & -h \end{pmatrix} Y_{l+1, m+h}(\hat{r}) \left( \frac{d}{dr} - \frac{l}{r} \right) R_{nl}(r) - \sqrt{l} (-1)^{l+m+h} \begin{pmatrix} l-1 & l & 1 \\ m+h & -m & -h \end{pmatrix} Y_{l-1, m+h}(\hat{r}) \left( \frac{d}{dr} + \frac{l+1}{r} \right) R_{nl}(r) \right) d^3 \underline{r}$$

Separating into radial and angular integrals, with  $d^3r = r^2 dr d\Omega$ ,

$$H = (4\pi)^{\frac{3}{2}} (-1)^{l+m+h} \sum_{l'} \sum_{m'} (i^{l'})^* (e^{-i\delta_{l'}})^* \sum_{\lambda} i^{\lambda} \sqrt{2\lambda+1} \gamma_{l'm'} \left( \frac{\hat{r}}{r} \right) \\ \sum_a \begin{pmatrix} a & l & 1 \\ m+h & -m & -h \end{pmatrix} R(n, l, l', \lambda, a) \int \gamma_{l'm'}^* \left( \frac{\hat{r}}{r} \right) \gamma_{\lambda 0} \left( \frac{\hat{z}}{r} \right) \gamma_{a, m+h} \left( \frac{\hat{z}}{r} \right) d\Omega,$$

where  $R(n, l, l', \lambda, l+1) = \sqrt{l+1} \int g_{l'}(kr) j_{\lambda} \left( \frac{A-1}{A} kr \right) \left( \frac{d}{dr} - \frac{l}{r} \right) R_{nl}(r) r^2 dr,$

$$R(n, l, l', \lambda, l-1) = -\sqrt{l} \int g_{l'}(kr) j_{\lambda} \left( \frac{A-1}{A} kr \right) \left( \frac{d}{dr} + \frac{l+1}{r} \right) R_{nl}(r) r^2 dr,$$

and  $a$  runs over the two values  $l-1, l+1$ .

Using the addition theorem for the product of three spherical harmonics of the same argument

$$H = 4\pi (-1)^{l+m+h} \sum_{\lambda} i^{\lambda} (2\lambda+1) \sum_a \sqrt{2a+1} \begin{pmatrix} a & l & 1 \\ m+h & -m & -h \end{pmatrix} \sum_{l'} \sqrt{2l'+1} (i^{l'})^* (e^{-i\delta_{l'}})^* \\ \begin{pmatrix} l' & \lambda & a \\ 0 & 0 & 0 \end{pmatrix} R(n, l, l', \lambda, a) \sum_{m'} (-1)^{m'} \begin{pmatrix} l' & \lambda & a \\ -m' & 0 & m+h \end{pmatrix} \gamma_{l'm'} \left( \frac{\hat{r}}{r} \right).$$

$|H|^2 = HH^*$  is required :

$$HH^* = 16\pi^2 \sum_{\lambda} \sum_{\Lambda} i^{\lambda} (i^{\Lambda})^* (2\lambda+1)(2\Lambda+1) \sum_a \sum_b \sqrt{2a+1} \sqrt{2b+1} \\ \begin{pmatrix} a & l & 1 \\ m+h & -m & -h \end{pmatrix} \begin{pmatrix} b & l & 1 \\ m+h & -m & -h \end{pmatrix} \sum_{l'} \sum_{L'} \sqrt{2l'+1} \sqrt{2L'+1} (i^{l'})^* i^{L'} \\ (e^{-i\delta_{l'}})^* e^{-i\delta_{L'}} \begin{pmatrix} l' & \lambda & a \\ 0 & 0 & 0 \end{pmatrix} \begin{pmatrix} L' & \lambda & b \\ 0 & 0 & 0 \end{pmatrix} \\ R(n, l, l', \lambda, a) R(n, l, L', \lambda, b) \sum_{m'} \sum_{M'} (-1)^{m'} (-1)^{M'} \\ \begin{pmatrix} l' & \lambda & a \\ -m' & 0 & m+h \end{pmatrix} \begin{pmatrix} -L' & \lambda & b \\ -M' & 0 & m+h \end{pmatrix} \gamma_{l'm'} \left( \frac{\hat{r}}{r} \right) \gamma_{L'M'}^* \left( \frac{\hat{r}}{r} \right).$$

Using the addition theorem for the product of two spherical harmonics of the

same argument and  $\begin{pmatrix} j_1 & j_2 & j_3 \\ m_1 & m_2 & m_3 \end{pmatrix} = 0$  if  $m_1 + m_2 + m_3 \neq 0$

on the terms involving  $m'$  and  $M'$ ,

$$\begin{aligned}
 HH^* &= 4\pi \sum_{\lambda} \sum_{\Lambda} i^{\lambda} (i^{\Lambda})^* (2\lambda+1)(2\Lambda+1) \sum_a \sum_b \sqrt{2a+1} \sqrt{2b+1} \\
 &\quad \begin{pmatrix} a & \ell & 1 \\ m+h & -m & -h \end{pmatrix} \begin{pmatrix} b & \ell & 1 \\ m+h & -m & -h \end{pmatrix} \sum_{\ell'} \sum_{L'} \sqrt{2\ell'+1} \sqrt{2L'+1} (i^{\ell'})^* i^{L'} \\
 &\quad (e^{-i\delta_{\ell'}})^* e^{-i\delta_{L'}} \begin{pmatrix} \ell' & \lambda & a \\ 0 & 0 & 0 \end{pmatrix} \begin{pmatrix} L' & \Lambda & b \\ 0 & 0 & 0 \end{pmatrix} \\
 &\quad R(n, \ell, \ell', \lambda, a) R(n, \ell, L', \Lambda, b) \begin{pmatrix} \ell' & \lambda & a \\ -m-h & 0 & m+h \end{pmatrix} \begin{pmatrix} L' & \Lambda & b \\ -m-h & 0 & m+h \end{pmatrix} \\
 &\quad \sum_c (-1)^{-m-h} (2c+1) \sqrt{2\ell'+1} \sqrt{2L'+1} \begin{pmatrix} \ell' & L' & c \\ -m-h & m+h & 0 \end{pmatrix} \begin{pmatrix} \ell' & L' & c \\ 0 & 0 & 0 \end{pmatrix} P_c(\cos\theta)
 \end{aligned}$$

$$\text{where } \cos\theta = \hat{k} \cdot \hat{z}.$$

At this point it is useful to note that, since

$$\begin{pmatrix} j_1 & j_2 & j_3 \\ 0 & 0 & 0 \end{pmatrix} = 0 \text{ if } j_1 + j_2 + j_3 = \text{odd}$$

and  $a, b = \ell \pm 1$ , the sums of the angular momentum quantum numbers in all the 3j-symbols are even. This also implies  $\lambda - \Lambda - \ell' + L' = \text{even}$ .

To form  $\sum_{f \bar{i}} |H|^2$  with the above wavefunctions,  $HH^*$  must be averaged over photon polarisations and initial state angular momentum projections i.e.

$$\sum_{f \bar{i}} |H|^2 = \frac{1}{2\ell+1} \sum_m \frac{1}{2} \sum_h HH^*.$$

$$\sum |H|^2 = \frac{4\pi}{2(2\ell+1)} \sum_{\lambda} \sum_{\Lambda} i^{\lambda} (i^{\Lambda})^* (2\lambda+1)(2\Lambda+1) \sum_a \sum_b \sqrt{2a+1} \sqrt{2b+1}$$

$$\sum_{\ell'} \sum_{L'} (2\ell'+1)(2L'+1) (i^{\ell'})^* i^{L'} (e^{-i\delta_{\ell'}})^* e^{-i\delta_{L'}}$$

$$\begin{pmatrix} \ell' & \lambda & a \\ 0 & 0 & 0 \end{pmatrix} \begin{pmatrix} L' & \Lambda & b \\ 0 & 0 & 0 \end{pmatrix} R(u, \ell, \ell', \lambda, a) R(u, \ell, L', \Lambda, b)$$

$$\sum_c (2c+1) \begin{pmatrix} \ell' & L' & c \\ 0 & 0 & 0 \end{pmatrix} P_c(\cos\theta) \sum_m \sum_h (-1)^{-m-h} \begin{pmatrix} a & \ell & 1 \\ m+h & -m & -h \end{pmatrix}$$

$$\begin{pmatrix} b & \ell & 1 \\ m+h & -m & -h \end{pmatrix} \begin{pmatrix} \ell' & \lambda & a \\ -m-h & 0 & m+h \end{pmatrix} \begin{pmatrix} L' & \Lambda & b \\ -m-h & 0 & m+h \end{pmatrix} \begin{pmatrix} \ell' & L' & c \\ -m-h & m+h & 0 \end{pmatrix}$$

Writing out  $\sum_h$  explicitly, the sum involving  $m$  and  $h$  becomes

$$\sum_m (-1)^{-m-1} \begin{pmatrix} a & \ell & 1 \\ m+1 & -m & -1 \end{pmatrix} \begin{pmatrix} b & \ell & 1 \\ m+1 & -m & -1 \end{pmatrix} \begin{pmatrix} \ell' & \lambda & a \\ -m-1 & 0 & m+1 \end{pmatrix} \begin{pmatrix} L' & \Lambda & b \\ -m-1 & 0 & m+1 \end{pmatrix}$$

$$\begin{pmatrix} \ell' & L' & c \\ -m-1 & m+1 & 0 \end{pmatrix} + (-1)^{-m+1} \begin{pmatrix} a & \ell & 1 \\ m-1 & -m & 1 \end{pmatrix} \begin{pmatrix} b & \ell & 1 \\ m-1 & -m & 1 \end{pmatrix}$$

$$\begin{pmatrix} \ell' & \lambda & a \\ -m+1 & 0 & m-1 \end{pmatrix} \begin{pmatrix} L' & \Lambda & b \\ -m+1 & 0 & m-1 \end{pmatrix} \begin{pmatrix} \ell' & L' & c \\ -m+1 & m-1 & 0 \end{pmatrix}$$

Since  $\begin{pmatrix} j_1 & j_2 & j_3 \\ m_1 & m_2 & m_3 \end{pmatrix} = (-1)^{j_1+j_2+j_3} \begin{pmatrix} j_1 & j_2 & j_3 \\ -m_1 & -m_2 & -m_3 \end{pmatrix}$

and, for all the  $3j$ -symbols,  $j_1 + j_2 + j_3 = \text{even}$ , the signs of the angular momentum projection quantum numbers in the second set of five  $3j$ -symbols

may be reversed. The above expression then becomes

$$\sum_m (-1)^{-m-1} \begin{pmatrix} a & \ell & 1 \\ m+1 & -m & -1 \end{pmatrix} \begin{pmatrix} b & \ell & 1 \\ m+1 & -m & -1 \end{pmatrix} \begin{pmatrix} \ell' & \lambda & a \\ -m-1 & 0 & m+1 \end{pmatrix} \begin{pmatrix} L' & \Lambda & b \\ -m-1 & 0 & m+1 \end{pmatrix} \begin{pmatrix} \ell' & L' & c \\ -m-1 & m+1 & 0 \end{pmatrix}$$

$$+ \sum_m (-1)^{-m+1} \begin{pmatrix} a & \ell & 1 \\ -m+1 & m & -1 \end{pmatrix} \begin{pmatrix} b & \ell & 1 \\ -m+1 & m & -1 \end{pmatrix} \begin{pmatrix} \ell' & \lambda & a \\ m-1 & 0 & -m+1 \end{pmatrix} \begin{pmatrix} L' & \Lambda & b \\ -m-1 & 0 & m+1 \end{pmatrix} \begin{pmatrix} \ell' & L' & c \\ -m-1 & m+1 & 0 \end{pmatrix}$$

$$= \left( \sum_m + \sum_{-m} \right) (-1)^{m+1} \begin{pmatrix} a & \ell & 1 \\ m+1 & -m & -1 \end{pmatrix} \begin{pmatrix} b & \ell & 1 \\ m+1 & -m & -1 \end{pmatrix}$$

$$\begin{pmatrix} \ell' & \lambda & a \\ -m-1 & 0 & m+1 \end{pmatrix} \begin{pmatrix} L' & \Lambda & b \\ -m-1 & 0 & m+1 \end{pmatrix} \begin{pmatrix} \ell' & L' & c \\ -m-1 & m+1 & 0 \end{pmatrix}$$

Consider  $i^\lambda (i^\lambda)^* (i^{l'})^* i^{l'} (e^{-i\delta_{l'}})^* e^{-i\delta_{l'}}$  ; this is equal to

$$\cos\left(\frac{\pi}{2}(\lambda - \lambda - l' + l')\right) \cos(\delta_{l'} - \delta_{l'}) - \sin\left(\frac{\pi}{2}(\lambda - \lambda - l' + l')\right) \sin(\delta_{l'} - \delta_{l'})$$

$$+ i \sin\left(\frac{\pi}{2}(\lambda - \lambda - l' + l')\right) \cos(\delta_{l'} - \delta_{l'}) + i \cos\left(\frac{\pi}{2}(\lambda - \lambda - l' + l')\right) \sin(\delta_{l'} - \delta_{l'}) .$$

$$\lambda - \lambda - l' + l' = \text{even} \quad \therefore \sin\left(\frac{\pi}{2}(\lambda - \lambda - l' + l')\right) = 0 .$$

$\sin(\delta_{l'} - \delta_{l'})$  is antisymmetric under exchange of  $l', l'$ . The rest of  $\sum |H|^2$  is symmetric under such an exchange since  $l' + l' + c = \text{even}$ . Therefore when forming  $\sum_{l'} \sum_{l'}$  the  $\sin(\delta_{l'} - \delta_{l'})$  terms vanish. This leaves

$$\cos\left(\frac{\pi}{2}(\lambda - \lambda - l' + l')\right) \cos(\delta_{l'} - \delta_{l'}) = (-1)^{\frac{1}{2}(\lambda - \lambda - l' + l')} \cos(\delta_{l'} - \delta_{l'}) \text{ only.}$$

Using  $\sum_m + \sum_{-m} = 2 \sum_m$ , the equation for  $\sum |H|^2$  becomes

$$\sum_{l'} |H|^2 = \frac{4\pi}{2l+1} \sum_{\lambda} \sum_{\lambda} (2\lambda+1)(2\lambda+1) \sum_a \sum_b \sqrt{2a+1} \sqrt{2b+1} \sum_{l'} \sum_{l'} (2l'+1)(2l'+1)$$

$$(-1)^{\frac{1}{2}(\lambda - \lambda - l' + l')} \cos(\delta_{l'} - \delta_{l'}) \begin{pmatrix} l' & \lambda & a \\ 0 & 0 & 0 \end{pmatrix} \begin{pmatrix} l' & \lambda & b \\ 0 & 0 & 0 \end{pmatrix}$$

$$R(u, l, l', \lambda, a) R(u, l, l', \lambda, b) \sum_c (2c+1) \begin{pmatrix} l' & l' & c \\ 0 & 0 & 0 \end{pmatrix} P_c(\cos\theta)$$

$$\sum_m (-1)^{m+1} \begin{pmatrix} a & l & 1 \\ m+1 & -m & -1 \end{pmatrix} \begin{pmatrix} b & l & 1 \\ m+1 & -m & -1 \end{pmatrix} \begin{pmatrix} l' & \lambda & a \\ -m-1 & 0 & m+1 \end{pmatrix} \begin{pmatrix} l' & \lambda & b \\ -m-1 & 0 & m+1 \end{pmatrix}$$

$$\begin{pmatrix} l' & l' & c \\ -m-1 & m+1 & 0 \end{pmatrix} .$$

The continuum state of a  $(\gamma, p)$  reaction is presumed to be a scattering state of the optical potential appropriate to the residual nucleus. The effects of the real and imaginary components of the optical potential may be separated. The real component may be considered to relate the momentum inside the nucleus just after the interaction to the momentum observed externally (the momentum of the photoproton at infinity,) whereas the imaginary component may be considered as merely providing an overall reduction 11).

The simplest way of treating the real part of the optical potential is to evaluate the matrix element for a proton energy inside the nucleus which is different from that outside by an amount equal to the depth of the real part of the optical potential

$$E_{\text{internal}} = E_{\text{external}} + V_{\text{optical}}^{\text{real}}$$

$$\text{or } k_{\text{internal}}^2 = k_{\text{external}}^2 + \frac{2m}{\hbar^2} V_{\text{optical}}^{\text{real}} .$$

This relation is used (incorrectly) in refs. 16 and 49.

The imaginary component of the optical potential may be treated with the assumption that the outgoing proton is a plane wave and that the imaginary component  $V_{\text{optical}}^{\text{imaginary}}$  is constant out to a radius  $D$  (e.g. the nuclear matter radius) and zero thereafter. The plane wave

$$e^{i\mathbf{k} \cdot \mathbf{r}} = e^{i\mathbf{k}_{\text{real}} \cdot \mathbf{r}} e^{-\mathbf{k}_{\text{imaginary}} \cdot \mathbf{r}}$$

$$k_{\text{imaginary}} \approx -\frac{1}{2} \sqrt{\frac{2m}{\hbar^2} \frac{V_{\text{optical}}^{\text{imaginary}}}{E - V_{\text{optical}}^{\text{real}}}} \quad (\text{ref. 50})$$

is attenuated as it advances up to  $r = D$  but for  $r > D$  there is no attenuation. After leaving the nucleus the attenuation is  $e^{-k_{\text{imaginary}} D}$ . The cross-section is thus reduced by  $e^{-2k_{\text{imaginary}} D}$ .

Appendix 15     Fourier transforms

The Fourier transform of a function  $\psi(\underline{r})$  is

$$\phi(\underline{q}) = \frac{1}{(2\pi)^{3/2}} \int e^{-i\underline{q} \cdot \underline{r}} \psi(\underline{r}) d^3r$$

Suppose  $\psi(\underline{r})$  may be written  $\psi(\underline{r}) = R_{nl}(r) Y_{lm}(\hat{\underline{r}})$ , where  $\int |R_{nl}(r)|^2 r^2 dr = 1$ .

The complex exponential is expanded in partial waves (47, 48)

$$e^{i\underline{q} \cdot \underline{r}} = 4\pi \sum_{l'} \sum_{m'} i^{l'} j_{l'}(qr) Y_{l'm'}^*(\hat{\underline{q}}) Y_{l'm'}(\hat{\underline{r}})$$

Then using the orthogonality relation for the spherical harmonics

$$\int Y_{l'm'}^* Y_{lm} d\Omega = \delta_{ll'} \delta_{mm'}$$

$$\phi(\underline{q}) = (-i)^l Q_{nl}(q) Y_{lm}(\hat{\underline{q}}) \quad \text{where} \quad Q_{nl}(q) = \sqrt{\frac{2}{\pi}} \int j_l(qr) R_{nl}(r) r^2 dr$$

$$\text{and} \quad \int |Q_{nl}(q)|^2 q^2 dq = 1$$

Often the average  $\frac{1}{2l+1} \sum_m$  over the angular momentum substates  $m$ ,

$-1 \leq m \leq 1$  is required. Using (48)  $\sum_m |Y_{lm}|^2 = \frac{2l+1}{4\pi}$ ,

$$\frac{1}{2l+1} \sum_m |\phi(\underline{q})|^2 = \frac{1}{4\pi} |Q_{nl}(q)|^2$$

## References

- 1) S. K. Gardiner  
Ph.D. thesis, University of Glasgow, 1971
- 2) S. H. Gardiner, J. L. Matthews and R. O. Owens  
Phys. Lett. 46B (1973) 186
- 3) J. L. Matthews  
private communication
- 4) M. G. Huber  
Ann. Phys. (Paris) 5 (1970) 239 (and references cited therein)
- 5) C. Ciofi degli Atti  
"The Nuclear Many-Body Problem", ed. F. Calogero and  
C. Ciofi degli Atti, Editrice Compositori, Bologna, 1973
- 6) C. Ciofi degli Atti and H. M. Eabachnik  
Phys. Rev. C 1 (1970) 809
- 7) V. E. Herscovits  
Nucl. Phys. A161 (1971) 321
- 8) S. Pittel and N. Austern  
Nucl. Phys. A218 (1974) 221
- 9) A. B. Clegg  
"High Energy Nuclear Reactions", Clarendon Press, Oxford, 1965
- 10) G. Jacob and Th. A. J. Maris  
Rev. Mod. Phys. 38 (1966) 121 and Rev. Mod. Phys. 45 (1973) 6
- 11) K. Nakamura and E. Izutsu  
Report UPRN-51, University of Tokyo, 1975
- 12) H. Kobberling, J. Moritz, K. H. Schmidt, D. Wegener, D. Zeller,  
J. K. Bienlein, J. Bleckwenn, H. Dinter and F. H. Heimlich  
Nucl. Phys. A231 (1974) 504
- 13) C. Schuhl  
Conference (Asilomar, March 1973) "Photonuclear Reactions and  
Applications" Proceedings, ed. B. L. Berman
- 14) A. B. Penfold and J. E. Leiss  
Phys. Rev. 114 (1959) 1332
- 15) E. Bramanis, T. K. Deague, R. S. Hicks, R. J. Hughes, E. G. Muirhead,  
R. H. Sambell and R. J. J. Stewart  
Nucl. Instr. Meth. 100 (1972) 59
- 16) G. Manuzio, G. Ricco, M. Sanzone and L. Ferrero  
Nucl. Phys. A133 (1969) 225
- 17) M. Sanzone, G. Ricco, S. Costa and L. Ferrero  
Nucl. Phys. A153 (1970) 401
- 18) E. Mancini, G. Ricco, M. Sanzone, S. Costa and L. Ferrero  
Nuovo Cim. 15A (1973) 705

- 19) C. Whitehead, W. R. McMurray, H. J. Aitken, H. Middlemas and C. H. Collie  
Phys. Rev. 110 (1955) 941
- 20) J. L. Matthews and R. O. Owens  
Nucl. Instr. Meth. 91 (1971) 37 and Nucl. Instr. Meth. 111 (1973) 157
- 21) A. N. Gorbunov and V. A. Osipova  
Sov. Phys. JETP 16 (1963) 27
- 22) G. G. Taras and A. N. Gorbunov  
Sov. J. Nucl. Phys. 6 (1968) 816
- 23) G. G. Taras  
Sov. J. Nucl. Phys. 7 (1968) 301
- 24) G. R. Hogg, A. G. Slight, T. E. Drake, A. Johnston and G. R. Bishop  
Nucl. Instr. Meth. 101 (1972) 203
- 25) S. Penner  
Rev. Sci. Instr. 32 (1961) 150
- 26) S. Penner  
N. B. S. Internal Report
- 27) S. H. Gardiner, J. L. Matthews and R. O. Owens  
Nucl. Instr. Meth. 87 (1970) 285
- 28) A. G. Slight  
Ph.D. thesis, University of Glasgow, 1971
- 29) Nuclear Enterprises Ltd., Edinburgh, Scotland
- 30) H. W. Koch and J. W. Metz  
Rev. Mod. Phys. 31 (1959) 920
- 31) R. T. Deck, C. J. Mullin and C. L. Hammer  
Nuovo Cim. 32 (1964) 180
- 32) W. C. Barber and T. Wiedling  
Nucl. Phys. 18 (1960) 575
- 33) R. H. Dalitz and D. R. Yennie  
Phys. Rev. 105 (1957) 1598
- 34) L. R. B. Elton  
"Introductory Nuclear Theory", Pitman and Sons Ltd., London, 1965
- 35) G. Ticcioni, S. H. Gardiner, J. L. Matthews and R. O. Owens  
Phys. Lett. 46B (1973) 369
- 36) R. M. Sternheimer  
"Methods of Experimental Physics", Vol. 5 (Nuclear Physics), part A,  
ed. L. C. L. Yuan and C-S Wu (and references cited therein)

- 37) J. T. O'Brien, H. Crannell, F. J. Klein and S. Penner  
Phys. Rev. C 9 (1974) 1418 (and references cited therein)
- 38) P. Cziffra and H. J. Horavcsik  
Report UCRL-8523 Rev., University of California, 1959
- 39) T. Lauritsen and F. Ajzenberg-Selove  
Nucl. Phys. 78 (1966) 1
- 40) F. Ajzenberg-Selove and T. Lauritsen  
Nucl. Phys. A114 (1968) 1
- 41) F. Ajzenberg-Selove  
Nucl. Phys. A152 (1970) 1
- 42) B. Rossi and K. Greisen  
Rev. Mod. Phys. 13 (1941) 240
- 43) G. D. Badhwar, C. L. Deney, B. R. Dennis and M. F. Kaplan  
Nucl. Instr. Meth. 57 (1967) 116
- 44) C. A. Baker, B. E. Bonner, I. H. Blair, F. P. Brady, J. A. Edgington  
and V. J. Howard  
Nucl. Instr. Meth. 71 (1969) 117
- 45) D. F. Measday and C. Richard-Serre  
CERN Report 69-17 (1969)
- 46) F. Mandl  
"Quantum Mechanics", Butterworths Scientific Publications, London, 1954
- 47) A. R. Edmonds  
"Angular Momentum in Quantum Mechanics", Princeton University Press,  
Princeton, 1960
- 48) D. M. Brink and G. R. Satchler  
"Angular Momentum", Clarendon Press, Oxford, 1962
- 49) G. M. Shklyarevskii  
Sov. Phys. JETP 36(9) (1959) 1057
- 50) A. E. S. Green, T. Sawada and D. S. Saxon  
"The Nuclear Independent Particle Model - The Shell and Optical Models",  
Academic Press, 1968
- 51) H. Danos and E. G. Fuller  
"Photonuclear Reactions", Annual Review of Nuclear Science, vol. 15,  
1965
- 52) K. Nakamura  
Report UTPH-36, University of Tokyo, 1974
- 53) J. L. Matthews, W. Bertozzi, M. J. Leitch, C. P. Sargent,  
W. Turchinets and R. O. Owens  
Bull. Amer. Phys. Soc. II 20 (1975) 629 and Symposium on Interaction  
Studies in Nuclei, Mainz, February, 1975

- 54) H. Schier and B. Schoch  
Nucl. Phys. A229 (1974) 93
- 55) H. Schier and B. Schoch  
Report "Cross-sections for the direct ( $\gamma, n$ ) reaction in  $O^{16}$ ,  $C^{12}$   
and  $Be^9$  at 60 MeV photon energy", University of Mainz
- 56) E. G. Fuller, H. M. Gerstenberg, H. Vander Molen and T. C. Dunn  
"Photonuclear Reaction Data, 1973", N. B. S. Special Publication 380
- 57) E. B. Bazhanov and L. A. Kul'chitskii  
Sov. Phys. JETP 11 (1960) 1215
- 58) J. L. Matthews, W. Bertozzi, S. Kowalski, C. P. Sargent  
and W. Turchinets  
Nucl. Phys. A112 (1968) 654
- 59) J. C. Roynette, M. Arditi, J. C. Jacmart, F. Mazloum, H. Riou  
and C. Ruhla  
Nucl. Phys. A95 (1967) 545
- 60) S. Penner and J. E. Leiss  
Phys. Rev. 114 (1959) 1101
- 61) L. R. B. Elton and A. Swift  
Nucl. Phys. A94 (1967) 52
- 62) K. Seth  
Nucl. Phys. A133 (1969) 61
- 63) M. Fink, H. Hebach and K. Kummel  
Nucl. Phys. A186 (1972) 353
- 64) W. Weise  
Report "A Study of ( $\gamma, p$ ) Reactions at Intermediate Photon Energies"  
University of Erlangen-Nurnberg
- 65) S. Gamba, G. Ricco and G. Rottigni  
Nucl. Phys. A213 (1973) 383
- 66) A. deShalit and H. Feshbach  
"Theoretical Nuclear Physics", Vol. 1, John Wiley and Sons, 1974
- 67) J. M. Eisenberg and W. Greiner  
"Nuclear Theory", Vol. 2, North-Holland Publishing Co., 1970
- 68) M. Gari and H. Hebach  
Phys. Rev. C 10 (1974) 1629
- 69) H. Hebach  
Report "Photonuclear Reactions at Intermediate Energies",  
Ruhr-Universitat Bochum
- 70) J. W. Morris, Jr. and H. J. Weber  
Ann. Phys. (New York) 79 (1973) 34

- 71) C. Ciofi degli Atti  
Preprint "The Jastrow Method and its Applications: A Review"  
Istituto Superiore di Sanita, Rome, Italy
- 72) M. Danos  
Lecture Notes, Les Houches Summer School, 1968
- 73) I. E. McCarthy  
"Introduction to Nuclear Theory", John Wiley and Sons, 1968
- 74) G. R. Satchler  
Nucl. Phys. A100 (1967) 497
- 75) J. Mougey, D. Royer, M. Priou, M. Bernheim, A. Bussiere and G. J. Wagner  
Preprint "On the influence of Short Range Correlations on (e,c'p)  
Cross-sections", C. E. N. Saclay
- 76) B. A. Watson, P. P. Singh and R. E. Segel  
Phys. Rev. 182 (1969) 977
- 77) A. E. Glassgold and P. J. Kellogg  
Phys. Rev. 109 (1958) 1291
- 78) S. Radhakant  
Preprint "The Angular Distribution of Photo-protons ejected from  
Light Nuclei", McGill University
- 79) Ulehla, Gomocak and Pluhar  
"Optical Model of the Atomic Nucleus", Academic Press, 1964,  
p. 97 and 104
- 80) B. K. Jain and D. F. Jackson  
Nucl. Phys. A99 (1967) 113
- 81) Yu. A. Kudryarov, V. G. Neudachin, S. G. Serebryakov and Yu. F. Smirnov  
Sov. J. Nucl. Phys. 6 (1968) 876
- 82) W. Weise  
private communication
- 83) C. Ciofi degli Atti  
Report ISS P 74/5, Istituto Superiore di Sanita
- 84) W. Weise and M. G. Huber  
Nucl. Phys. A162 (1971) 330
- 85) M. Dillig, H. M. Hofmann and M. G. Huber  
Phys. Lett. 44B (1973) 454
- 86) G. M. Shklyarevskii  
Sov. Phys. JETP 14 (1962) 170 and Sov. Phys. JETP 14 (1962) 324
- 87) M. Bernheim, A. Bussiere, A. Gillebert, J. Mougey, Phan Xuan Ho,  
M. Priou, D. Royer, I. Sick and G. J. Wagner  
Phys. Rev. Lett. 32 (1974) 898

- 88) F. H. Heimlich, E. Rosale, M. Kobberling, J. Moritz, K. H. Schmidt,  
D. Wegener, D. Zeller, J. K. Biehnlein, J. Eieckwein and H. Dinter  
Nucl. Phys. A228 (1974) 478
- 89) H. Arenhovel and W. Fabian  
Phys. Lett. 52B (1974) 303
- 90) H. Arenhovel  
Phys. Lett. 53B (1974) 224

